# Time resolved electrostatic force microscopy measurements of ionic transport

Aaron Mascaro

Department of Physics
McGill University, Montreal

*Supervisor:*
Dr. Peter Grütter

A Thesis submitted to McGill University in partial fulfillment of the requirements for the degree of Doctor of Philosophy

December 2018

# Acknowledgements

I would like to begin by acknowledging my supervisor, Prof. Peter Grütter, who has guided and mentored me along the way, and whose continued support and encouragement has proved invaluable, and Prof. Yoichi Miyahara, whose technical knowledge, abilities, and insightful conversations have allowed me to succeed.

I would also like to thank Dr. Karim Zaghib and his team at Hydro-Québec for their funding and support in our collaboration as well as the samples and discussions they provided.

Thanks to Prof. Kirk Bevan and Zi Wang for the helpful discussions and insight.

I would like to thank the rest of our group members for their help around the lab, fruitful discussions, and, of course, their friendship.

To all of my friends, far and wide: thank you for all of the wonderful memories and for helping and motivating me in times of need.

To LeeAnna, my wonderful partner, thank you for all you've done for me and for your never-ending patience.

Finally, I would like to thank my family, especially my parents Matt and Brenda, for inspiring my curiosities about the world from a young age. I truly could not have achieved a fraction of the things I have thus far without them.

# Abstract

The present thesis is a collection of scientific articles published or submitted by the author during the period from 2015-2018 as part of Ph.D. research conducted at McGill University. Each of these articles explores an aspect of performing quantitative measurements using atomic force microscopy. The first chapter introduces the motivation for the work, explains the basic workings of a lithium ion battery and the challenges faced in developing better batteries, and concludes by exploring a variety of atomic force microscopy-based techniques and how they have been and will be used to study battery materials. The remaining chapters are presented in a coherent order instead of chronologically for cohesiveness.

The second chapter demonstrates the use of time-domain electrostatic force microscopy to probe ionic transport on lithium iron phosphate, a material currently used in some commercial batteries. Ionic transport in solids is known to follow a stretched exponential response in the time domain, which is observed in the direct time-domain measurements performed on lithium iron phosphate. Previous theoretical descriptions of ionic transport in solids have concluded that the stretching factor in this stretched exponential response contains information regarding the collective motion of the ions (e.g. ion-ion interactions). By performing these measurements on a small region of a sample that was directly characterized using a variety of other techniques, the measurements were related to theoretical calculations obtained using density functional theory. These measurements demonstrate that large phase-boundary hopping barriers are the limiting factor for ionic transport, while the hopping barriers for ions in the bulk are significantly lower. These insights were made possible by the improved time resolution of the time-domain technique by implementation of a real-time averaging system. This represents a key finding in the understanding of ionic transport and a demonstration of the power of localized

dynamic measurements enabled by the atomic force microscope.

In the third chapter, the time resolution limits for time-domain electrostatic force microscopy are explored. A new technique is proposed and its much improved time resolution is demonstrated via a validation measurement on a metallic sample. Its limitations and application of this technique to ionic transport are then discussed in detail. Three other recently developed techniques that use voltage pulses to measure time-resolved sample responses are then explored in detail, along with their challenges and applicability to ionic transport measurements.

The fourth chapter then discusses the challenges in calibrating the spring constant of atomic force microscopy cantilevers. Accurate measurements of the cantilever spring constant are required to perform quantitative force measurements using atomic force microscopy. Cantilever spring constants are typically done by measuring the small oscillations of the cantilever due to thermal energy and analyzing them in the frequency domain. We show that this can be greatly affected by ambient acoustic noise. A protocol to calibrate the spring constants while precluding the effect of acoustic noise is then demonstrated by actively driving the cantilever; specifically by performing frequency sweeps and ringdown measurements.

# Résumé

La présente thèse est un recueil d'articles scientifiques publiées ou soumises par l'auteur au cours de la période 2015-2018 dans le cadre des recherches du troisième cycle menées à l'Université McGill. Chacun de ces articles étudie un aspect de la réalisation de mesures quantitatives à l'aide de la microscopie à force atomique. Le début du premier chapitre présente la motivation du travail. La suite explique le fonctionnement de base d'un accumulateur aux ions lithium et les défis rencontrés pour développer de meilleures batteries. On le chapitre conclut en explorant diverses techniques basées sur la microscopie à force atomique et leur utilisation pour étudier les matériaux de l'accumulateur. Les chapitres restants sont présentés dans un ordre cohérent mais pas nécessairement chronologique pour des raisons de cohésion.

Le deuxième chapitre montre l'utilisation de la microscopie à force électrostatique dans le domaine temporel pour étudier le transport ionique du lithium fer phosphate, un matériel utilisé actuellement dans certaines batteries commerciales. On sait que le transport ionique dans les solides suit une réponse exponentielle étendue dans le domaine temporel, qui est observée par les mesures directes dans le domaine temporel effectuées sur du lithium fer phosphate. Les descriptions théoriques du transport ionique dans les solides des récentes publications ont conclu que le facteur d'étirement dans la réponse exponentielle étendue contient des informations sur le mouvement collectif des ions (par ex. les interactions ion-ion). En effectuant ces mesures sur une petite région d'un échantillon qui a été directement caractérisé à l'aide d'une variété d'autres techniques, les mesures ont été associées à des calculs théoriques obtenus à l'aide de la théorie de la densité fonctionnelle. Ces mesures démontrent que les grandes barrières de saut en limite de phase constituent le facteur limitant pour le transport ionique, alors que les barrières de saut pour les ions en volume sont nettement plus faibles. Ces connaissances ont été

rendues possibles par l'amélioration de la résolution temporelle de la technique du domaine temporel par la mise en oeuvre d'un système de calcul de la moyenne en temps réel. Ceci représente une découverte clé dans la compréhension du transport ionique et une démonstration de la puissance des mesures dynamiques localisées rendues possibles par le microscope à force atomique.

Dans le troisième chapitre, on explore les limites de résolution temporelle pour la microscopie à force électrostatique dans le domaine temporel. On propose une nouvelle technique tout en démontrant sa résolution temporelle nettement améliorée via une mesure de validation sur un échantillon métallique. Ensuite, les limites et l'application de cette technique au transport ionique sont discutées en détail. De plus, trois autres techniques récemment développées qui utilisent des impulsions de tension pour mesurer les réponses des échantillons résolus dans le temps sont explorées en détail, ainsi que leurs difficultés et leur applicabilité aux mesures de transport ionique.

Le quatrième chapitre aborde les problèmes posés par la calibration de la constante de ressort des apex nanométriques situés sur la pointe du levier présent dans les microscopes à force atomique. Ces mesures précises de la constante de ressort des apex sont nécessaires pour effectuer des mesures de force quantitatives à l'aide de la microscopie à force atomique. Ces constantes de ressort sont généralement réalisées en mesurant les petites oscillations de l'apex dues à l'énergie thermique et en les analysant dans le domaine fréquentiel. On démontre que cela peut être grandement affecté par le bruit acoustique ambiant. Ensuite, un protocole permettant de calibrer les constantes de ressort tout en éliminant l'effet du bruit acoustique est démontré en actionnant activement l'apex du levier; en particulier en effectuant des balayages de fréquence et des mesures optiques.

# Preface

## Contributions of Authors

- Chapter 2: P.G., K.H.B., and K.Z. proposed and supervised the project. A.M. and Y.M. customized the commercial AFM and designed/built the data acquisiton system. A.M. performed the AFM experiments and analyzed the spectroscopy data. Z.W. performed the hopping barrier DFT calculations. P.H. and V.G. performed the SEM, TOF-SIMS, and EBSD measurements. A.P. synthesized the sample. Z.F. performed the work function DFT calculations. T.E. and C.A. prepared preliminary samples and conducted preliminary structural and compositional analysis of the sample (not shown). A.M. and Z.W. wrote the manuscript. All authors discussed the results and cultivated the final interpretation.

- Chapter 3: P.G. supervised the project. A.M. and Y.M. set up and performed the experiments. T.E. and O.D. contributed significantly in discussions regarding the data analysis and experimental parameters. A.M. wrote the manuscript. All authors revised and reviewed the manuscript.

- Chapter 4: P.G. and A.M. proposed the experiments. A.M., Y.M., and O.D. set up and performed the experiments. A.M. wrote the manuscript; all authors discussed the results and revised the manuscript.

# Statement of Originality

- The original contributions of this thesis are included in Chapters 2, 3, and 4.
- The original contributions of Chapter 2 are
  - The development of a real-time averaging system to perform time-domain electrostatic force measurements.
  - Local measurements of activation energy on lithium iron phosphate.
  - Extraction of single-ion vs. collective activation energies using the stretching factor from the stretched exponential response due to movement of ions.
- The original contributions of Chapter 3 are
  - The development of a new time-resolved electrostatic force microscopy technique that can measure dynamic processes much faster than the time period of the cantilever oscillation at resonance.
  - Simulations of the fast free time-resolved electrostatic force microscopy technique with a stretched exponential response.
- The original contributions of Chapter 4 are
  - Demonstration of the effect of acoustic noise on calibration measurements of the spring constant of an atomic force microscope cantilever.
  - Demonstration of a new protocol of driven techniques to calibrate the spring constant of an atomic force microscope cantilever that are unaffected by acoustic noise.

# Contents

# 1

# Introduction and Background

## 1.1 Motivation

With the rising threat of anthropogenic climate change, the world is turning away from fossil fuels with an ever increasing percentage of energy generation from renewable sources [1]. The demand for renewable energy production methods has led to tremendous technological advancements resulting in constantly decreasing prices of renewable energy technologies such as solar and wind [2]. Even with these environmentally friendly energy generation methods, we will only be able to eliminate our carbon output by also choosing more sustainable methods of locomotion, in particular, electric vehicles [3].

As of 2016, the cumulative sales of electric vehicles totalled over 2 million for the first time, making up 0.2% of the total automobile market [4]. To conform to the International Energy Agency (IEA)'s scenario to limit average global temperature increase to 1.75°C, it is estimated that an increase of electric vehicles to 86% of the market share is required by 2060 [5]. Consumer adoption of electric vehicles is expected to be limited mainly by three related factors: range, cost, and limitations in high-utilization applications [3].

As nearly all current-generation electric vehicles are powered by lithium-ion batteries, all three of these factors are limited both by battery performance and infrastructure; the former being truly a technological and scientific limitation, while the latter is an economic factor related to consumer adoption and demand [3]. The limitations imposed by lithium-ion battery technology are fundamentally due to three specific challenges: achieving fast charging times, improving total energy storage, and increasing cycle life (the number of times a battery can be charged and discharged while still retaining high energy capacity)[3, 6–10]. These challenges all require a broad, interdisciplinary approach in order to understand the mechanisms that limit battery performance and develop new materials and technologies that will eventually lead to mass adoption of affordable electric vehicles.

In this chapter I begin by exploring the basics of lithium ion batteries with a brief overview of their composition and functionality. I will then introduce atomic force microscopy and its applications, and conclude by discussing the role of atomic force microscopy in the study of battery materials.

## 1.2 Lithium Ion Batteries

### 1.2.1 Overview

Early discoveries of electrochemical storage of energy, such as the so-called “Volta pile" invented in 1800 by Alessandro Volta, typically exploited irreversible chemical reactions arising from inherent chemical potential differences between materials [11]. These non-rechargeable battery systems (otherwise known as *primary* batteries) would pave the way for an extraordinary era of innovation in electrochemistry, and thus, battery technology, eventually giving rise to the (still widely-used) lead-acid (Gaston Planté, 1859), nickel-cadmium (Waldmar Jungner, 1901), and, more recently developed, lithium-ion

rechargeable batteries [11]. One of the key breakthroughs that enabled lithium-ion batteries to reliably cycle (and that also sets them apart from previous rechargeable battery chemistries) was lithium intercalation compounds [12]. These compounds – LiNiMnCo (NMC), $LiFePO_4$ (LFP), and LiCoO2 (LCO), to name a few – allow for lithium ions to physically be moved into and out of the material in response to an applied electric field (or practically, an applied voltage). In a lithium-ion battery, the positive electrode (or cathode) materials provide a source of $Li^+$ ions, which can be deintercalated into an electrolytic solution or solid electrolyte as the battery is charged, illustrated in Figure 1.1. The ions then intercalate into the negative electrode (or anode) as a result of the applied voltage. Disconnecting the voltage source halts the motion of ions and results in a persistent potential difference between the negative and positive electrode. On connection of a load between the current collectors, the voltage then deintercalates the lithium ions from the negative electrode into the electrolyte and causes ions in the electrolyte to intercalate back into the positive electrode, thus discharging the battery. The electrons travel from the negative electrode to the positive electrode through the load, providing the electrical current to power the device. Although this process is fundamentally very straightforward, a large number of factors can affect the overall lithium ion transport, including: transport across the solid electrolyte interface and the solid-electrolyte-interphase (SEI) [13–17], transport through the electrolyte itself [18–22], and bulk transport through the active materials [17, 23–26].

Each of these factors may limit the performance of a battery depending on the physical structure/composition of the active materials, the specific chemistries used, and the intended application. Electric vehicles are an example of high-current applications; they require batteries that can provide large currents over short time periods and be recharged quickly (high power density). This presents a unique challenge as high discharge and

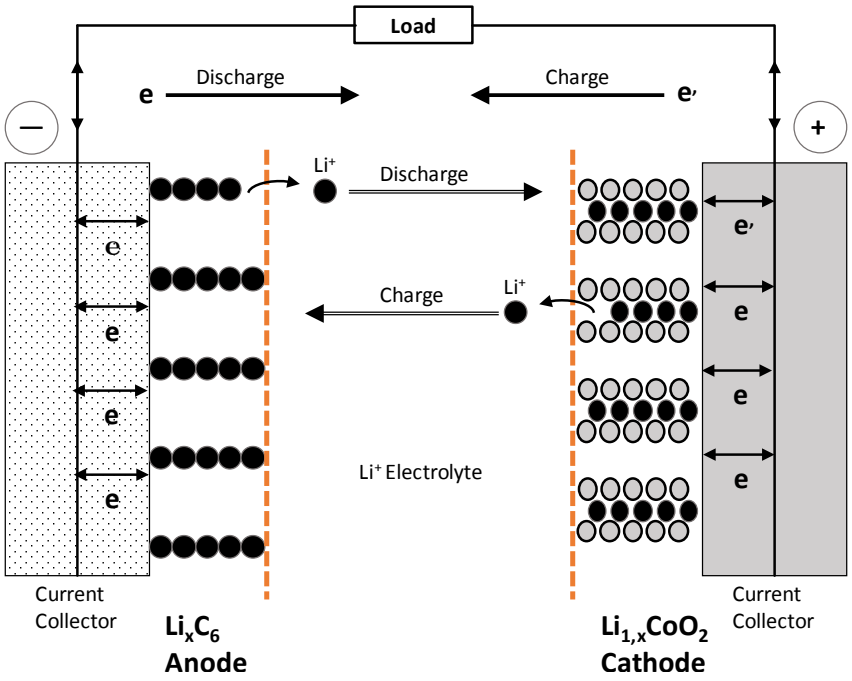


Figure 1.1: Overview of standard LCO lithium-ion battery function.

charge rates require high ionic mobility through all regions of the cell, which are often limited by low bulk mobility in the active materials. To increase bulk mobility requires an in-depth understanding of mechanisms that govern ionic transport in solid ionic conductors, which will be briefly introduced in the following section.

### 1.2.2 Solid State Ionic Transport

The study of solid ionic conductors dates back to work done by Schottky, Wagner, and Mott and Littleton in the 1930s where they derived much of the theory governing mass/charge transport in solids [27]. In general, solid ionic transport involves charged 'defects' that move by means of jump diffusion: they jump between specific sites in the lattice, changing places with the vacancy/atom that previously occupied the site [28]. The probability of a defect making a successful jump is related to the energy barrier along the path between the two sites, which can be derived using the dynamical theory of diffusion [29]. These mobile defects are generally of two types: Schottky defects, which

consist of a pair of vacancies ('missing' atoms) in ionic crystals, or simple (single) vacancies in non-ionic crystals; and Frenkel defects where atoms occupy interstitial sites, i.e. sites in the lattice that are not normally occupied. These are illustrated in Fig. 1.2.

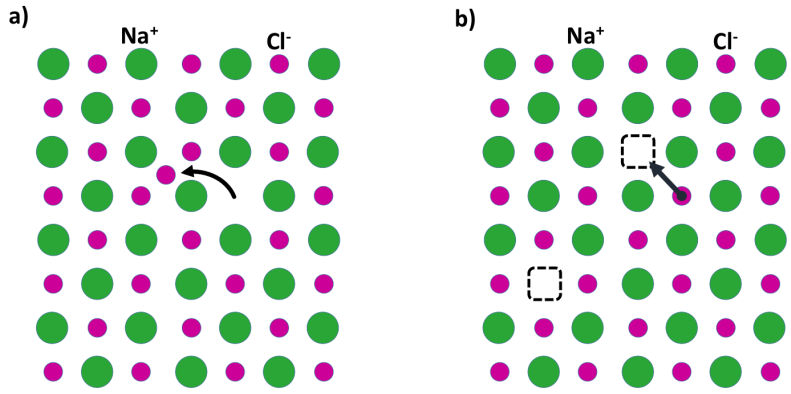


Figure 1.2: 2D representation of NaCl showing (a) a Frenkel, and (b) a Schottky defect along with a possible jump transition of a $Cl^-$ ion. Reproduced from [30].

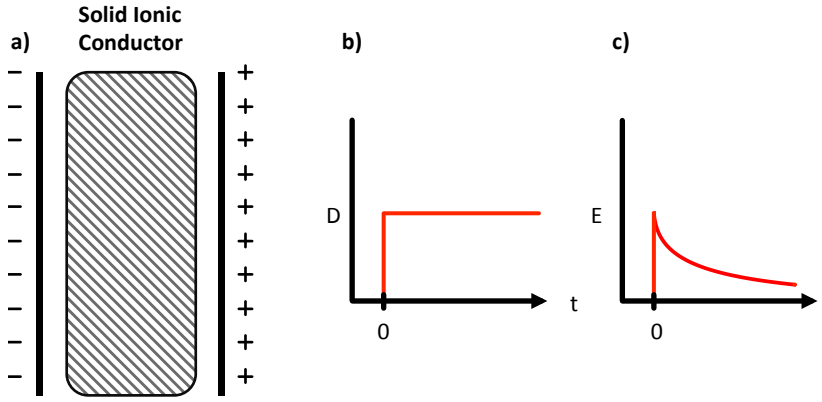


Figure 1.3: "(a) Solid ionic conductor between two conducting plates, (b) electric displacement field, D, is applied at t=0, (c) ensuing electric field decay due to ionic hopping effectively screening the field." [30].

Ionic transport in a solid ionic conductor is generally described by Fick's second law (the diffusion equation) [27]:

$$\frac{\partial C}{\partial t} = \nabla \cdot (D \nabla C) \tag{1.1}$$

where $C$ is the defect concentration and $D$ is the diffusivity. However, this model fails to capture the non-randomness of the ionic jumps that result from their strong interactions. Considering, for example, an ion such as that seen in Fig. 1.2(b), we see that after the ion has completed a jump into the vacant site, the most likely subsequent hop is back into its original location as the rest of the neighbouring sites are occupied. A first-order correction factor ($f$, $0 < f < 1$) can be introduced to capture this behaviour by writing: $D = fD_{UC}$ where $D$ is now the 'true' diffusivity and $D_{UC}$ is the uncorrelated diffusivity (from Eq. 1.1). This correction factor also appears when looking at the time-response of ions moving in a solid ionic conductor, illustrated in Fig. 1.3. If a step potential is applied across a solid ionic conductor there will be an (effectively) instantaneous change in the electric field through the material. This causes the mobile charge to separate in order to shield out the internal field (Fig. 1.3(c)), the time response of which is given by:

$$E(t) = E(0) \exp\left[-\left(\frac{t}{\tau}\right)^{\beta}\right] \tag{1.2}$$

where $\tau$ is the characteristic decay time and $\beta$ is a stretching factor ($0 < \beta < 1$) resulting from the interactions between charge carriers (as discussed above) [28]. The functional form of this response is the basis for much of the work in this thesis and will be elaborated on in detail in Chapter 2.

### 1.2.3 Standard Techniques and Measurements

Transport through liquid electrolytes is typically measured by standard techniques such as electrochemical impedance spectroscopy (EIS) [31–33], while interfacial transport and SEI formation have been studied by a wide range of characterization techniques including X-ray diffraction, scanning electron microscopy, raman spectroscopy, time of flight secondary-ion mass spectroscopy and many others [13]. Ionic transport through the bulk, on the other hand, can typically only be measured by solid-state impedance spec-

troscopy, which uses large conducting electrodes to measure the ionic response to applied ac electric fields [32, 34, 35]. This effectively measures the average response across the entire sample, thus averaging over any inhomogeneities that may be present. Real world battery materials, however, are known to be highly heterogeneous over length scales ranging from millimeters down to nanometers [36–39]. Many techniques exist to characterize local composition and structure across these length scales, however experimental measurements of dynamic processes are typically limited to large scale measurements (like impedance spectroscopy [32] or nuclear magnetic resonance [40]) or have time resolution much slower than the charge transport they aim to capture [41–43]. From this, it is clear that an experimental method that can spatially and temporally quantify ionic transport is necessary to help determine rate-limiting factors in lithium ion battery materials. Atomic force microscopy and it's related techniques demonstrate great promise in this regard, as will be discussed in the following section.

## 1.3 Atomic Force Microscopy

The field of scanning probe microscopy is broad and interdisciplinary with techniques that span all fields of experimentation. With the invention of the scanning tunneling microscope (STM) in 1981 [44], followed by the atomic force microscope (AFM) in 1986 [45], came a plethora of new tools for materials scientists. The basic principle of both types of microscopy involves moving a very sharp (in some cases, atomically sharp) probe over a sample surface while measuring some aspect of the interaction between the probe and the sample. The former measures the small electrical current between a conducting probe and a conducting sample, while the latter measures the mechanical status of a cantilever as the probe tip interacts with the sample. AFM is therefore capable of probing properties of both conducting and insulating samples. These properties include surface topography [44], local contact potential difference (which can be used to extract the

local work function) [46], local piezoelectric response [47], mechanical properties such as young's modulus and surface friction [48, 49], dopant profiles [50–52], and charge transport dynamics (electronic and ionic) [53–57]. All of these measurements exploit the highly sensitive force detecting nature of AFM in different ways, demonstrating the versatility of these instruments. This section will briefly introduce topographic imaging using AFM, followed by electrostatic force microscopy (EFM), achieving time resolution in EFM, and conclude by discussing some of the implications in calibrating AFM cantilevers to perform quantitative measurements. Each of these topics will be put into context and sufficiently explained in order to understand the measurements that will be discussed in the following chapters.

### 1.3.1 Topographic Imaging

A standard technique for performing topographic measurements using AFM is commonly known as tapping mode. In tapping mode AFM, the cantilever is oscillated at a fixed drive frequency ($\omega_D$), which differs slightly from the cantilever's free resonance frequency ($\omega_0$), and it is approached vertically to the sample surface, illustrated in Figure 1.4(a). As the probe tip begins to interact with the sample, the resonance frequency shifts, causing a decrease in the oscillation amplitude [45], illustrated in Figure 1.4(b). This is referred to as slope detection and is a stable imaging method that can reliably obtain atomic resolution as long as the quality factor ($Q$) of the cantilever is sufficiently low [58, 59]. In cases where $Q$ is very high – in vacuum, for example – slope detection suffers from slow amplitude response times due to the lack of strong dissipative forces acting on the cantilever (see Chapter 4 for an in-depth discussion). This results in unreasonably long measurement times as the tip-sample distance feedback can generally only operate as fast as the amplitude changes occur. It is therefore common in vacuum AFM systems to measure the change in resonance frequency directly instead of observing the amplitude

response, which is known as frequency-modulation AFM (FM-AFM) [59].

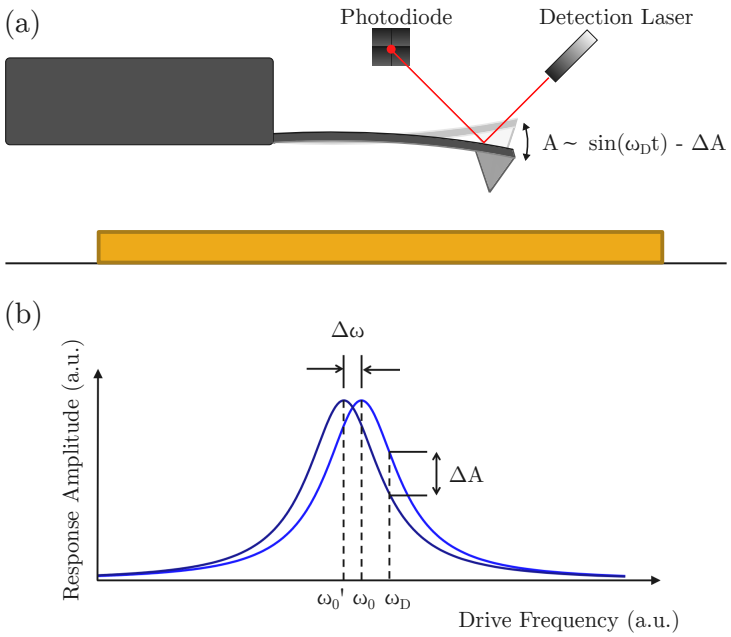


Figure 1.4: (a) Schematic illustration of a driven oscillating AFM cantilever using optical beam deflection sensing, modified from Ref. [60]. (b) Illustration of slope detection for tapping mode AFM, recreated from Ref. [59].

FM-AFM not only solves the challenge of topographic imaging in vacuum, but it also allows for significantly higher force sensitivity due to the large $Q$ of cantilevers in vacuum [59]. When used for topographic imaging, the primary pitfall of FM-AFM is due to instabilities in the oscillation, which can result in a tip crash [61]. These instabilities occur when the oscillation deviates significantly from its assumed sinusoidal behaviour due to abrupt changes in the interaction, dissipation, or excitation signals [61]. Practically, this has the effect of limiting the scan speed and the maximum topographic feature size that can be imaged; imaging very large, abrupt changes in topography will therefore result in tip crashes. This makes imaging of large features in vacuum conditions especially challenging using FM-AFM. A much more reliable technique is to image using tapping mode while artifically lowering the quality factor to allow for faster imaging times (i.e. adding artificial damping). This is known as Q-control and is done by adding an additional, nearly out of phase signal to the driving signal [62].

The topographic images in Chapter 2 were obtained using tapping mode in vacuum using Q-control (Figure 2.1), and standard FM-AFM topography (Figure 2.2). Topographic images were used extensively to find regions of interest to perform spectroscopy experiments, discussed below.

### 1.3.2 Electrostatic Force Microscropy

In the frequency-modulation mode, the cantilevers effectively act as very sensitive detectors of tip-sample interaction forces. These forces are dominated by electrostatics at large tip-sample separations ($\gtrsim$1 nm). The tip and sample effectively form a capacitor; the electrostatic force between them is given by:

$$F_E = -\frac{1}{2}\frac{\partial C}{\partial z}V^2 \tag{1.3}$$

where $C$ is the tip-sample capacitance, $z$ is the tip-sample separation, and $V$ is the total potential between the tip and sample. There exists a natural potential difference, $V_{CPD}$, between the tip and sample due to their difference in work functions. If an external potential, $V_{DC}$, is also applied, the voltage is then given by: $V = V_{DC} - V_{CPD}$. The electrostatic force acting on the cantilever can therefore be controlled by applying a potential between the tip and sample. A change in either the capacitance gradient, $\frac{\partial C}{\partial z}$, or the $V_{CPD}$ will then manifest as a change in the mechanical status of the cantilever. One example of this is a subset of EFM techniques known as Kelvin probe force microscopy (KPFM) that allows $V_{CPD}$ to be measured by applying both ac and dc voltages between the tip and sample [46]. In this case the total voltage is:

$$V = V_{DC} - V_{CPD} + V_{AC}\sin(\omega_E t) \tag{1.4}$$

where $V_{AC}$ and $\omega_E$ are the magnitude and frequency of the ac voltage, respectively.

The electrostatic force is then given by:

$$\begin{aligned} F_E = & \frac{\partial C}{\partial z}\left[\left((V_{DC}-V_{CPD})^2+\frac{1}{2}V_{AC}^2\right)\right. \\ & +(V_{DC}-V_{CPD})V_{AC}\sin(\omega_E t) \\ & \left.+\frac{1}{4}V_{AC}^2\cos(2\omega_E t)\right]. \end{aligned} \tag{1.5}$$

A standard implementation of KPFM is to utilize the second term in Equation 1.5 by varying $V_{DC}$ such that the amplitude of the force at $\omega_E$ goes to zero. This occurs when $V_{DC} = V_{CPD}$, thereby allowing a direct measurement of the local contact potential difference by simply measuring the applied bias, $V_{DC}$. This method, known as amplitude-modulation KPFM, is only one of many variations of techniques that extract local contact potential differences. These are summarized in detail in a recent review, Ref. [63].

Other EFM-based techniques have been used to quantify local capacitive properties [64–66], local dielectric constants [67–71]. Although each of these measurements uses a different approach to extracting information about local sample properties, they all fundamentally rely on the electrostatic forces between the tip and sample that mechanically affect the cantilever. The main advantage common through all EFM measurements are the high spatial resolution attainable due to the localized sensing inherent to atomic force microscopy.

Recently there has been significant interest in studying not only static material properties, but also dynamic properties on the nanometer-scale. This has led to the development of a variety of methods of measuring fast, time-resolved signals through EFM. These techniques can generally be subdivided into two main branches, those that use pulsed light sources, and those that use voltage pulses, although there exists at least one implementation that uses a combination of both [63, 72].

Pulsed light source measurements have had a long history of exploiting progress in ultrafast laser technology to temporally resolve charge transport. This dates back to one

of the earliest time-resolved EFM measurements by Hamers and Cahill that used 1 ps light pulses to measure the surface potential ($V_{CPD}$) as a function of pulse spacing to observe the decay of photoexcited charge carriers [54]. This implementation, including their use of a chopper to perform simultaneous 'dark' and 'light' measurements, has seen a recent resurgence, with demonstrated time-resolution as low as 1 ps [73, 74]. Compared to time-resolved optical spectroscopy measurements (e.g. pump-probe), illumination-assisted KPFM has significantly better spatial resolution as this is limited by the radius of the probe tip (which can be atomically sharp, in principle), while the latter has spatial resolution set by the diffraction limit of the light sources used [75, 76]. While optical pump-probe measurements are temporally limited only by the delay time between the pump and probe pulses [77, 78], pump probe KPFM measurements are fundamentally limited by the thermal noise of the cantilever, as are all time-resolved EFM measurements including voltage-pulsed EFM [79]. Thus, pump-probe EFM measurements sacrifice temporal resolution for spatial resolution to some degree.

Early time-resolved EFM measurements using voltage pulses employed direct measurements of the electrostatic force acting on the cantilever as a function of time directly after a voltage pulse is applied; this is referred to as direct time-domain EFM [53]. This technique, its limitations, and more recent variations to drastically improve the attainable time-resolution are discussed in Chapter 3. Since ionic mobility can only be probed by the application of a voltage pulse between the tip and sample, these are of particular interest in the field of battery materials. Thus, Chapter 3 provides an in-depth review of the most recent FM-AFM based voltage-pulsed EFM measurements and discusses their application to ionic transport measurements.

## 1.4 Atomic Force Microscopy and Battery Materials

### 1.4.1 History and State of the Art

The use of AFM techniques to study energy materials dates back to the early use of surface photovoltage measurements to probe the time decay of photoexcited charge carriers [54]. The first direct mention of AFM in the context of energy materials, however, would not be until 1996 when Aurbach and Cohen used topographic imaging on a copper electrode (current collector) in a lithium electrolyte before and after 'cycling' to image the plating and stripping of $Li^+$ [80]. These images used the high spatial resolution afforded by AFM to demonstrate that 'non-active' components, in this case the metal current collectors, used in lithium ion batteries can react with electrolytic solutions within the working potential of a standard cell. Later measurements on battery materials used KPFM to spatially resolve the local contact potential difference of a nickel electrode that had been plated and stripped multipled times with $Li^+$ [81]. Bealieu et al. used in situ AFM measurements to study the morphology changes in both crystalline and amorphous materials as they react with lithium to understand strain responses in lithium ion batteries [82]. Clemencon et al. later mapped volume expansion of LCO in situ during lithium deintercalation directly using contact mode AFM [83].

In order to probe charge transport characteristics, Semenov et al. performed dc conductance mapping on $V_2O_5$ on a $Li_3PO_4$ electrolyte [84], while Kuriyama et al. measured dc currents on the surface of $LiMn_2O_4$ in air while increasing the electric field [85]. These measurements, however, are unable to decouple contributions from ionic and electronic transport, and, as they use metalling tips that have no ionic conductivity, effectively only measure the latter.

A number of other authors have used AFM to probe local electrochemical impedance spectroscopy to study ionic and electronic transport [86–89]. However, as stated in

Ref. [90]: “the simple comparison of the tip-surface junction and cantilever surface impedances illustrates that direct measurements are possible only for well-defined mesoscopic objects (i.e., single-crystalline conductive grain with insulating grain boundaries, or micron-size battery element) but not local volume of material below the tip."

Electrochemical strain microscopy (ESM) is a recently developed technique to probe local ionic transport by studying the strain response of a material [90, 91]. ESM uses a conducting probe in contact with an ionically conducting material and analyzes the strain response (the tip displacement) as a function of the applied bias. This localized strain response is related to ionic conductivity in the material [91], however there exist many other potential contributions to the signal that must be corrected for, including: piezoelectric, flexoelectric, deformation potential, space charge, surface chemistry contributions, electroosmotic flow, and contact stiffness, which may not always be possible [92–94].

Other techniques, such as time-domain EFM, have been used to study ionic transport in various materials including glassy electrolytes [56], and other glassy ceramics [95, 96]. These techniques have not been used to investigate materials for applications in lithium ion batteries until recently, however.

The following chapter will present a novel application of time-domain EFM to a relevant battery material ($LiFePO_4$) with significantly improved time resolution, while Chapter 3 will discuss other techniques to further improve the time resolution, and Chapter 4 will discuss important considerations for calibrating the spring constant of AFM cantilevers to perform quantitative measurements, such as those detailed in Chapter 3.

# Preface to Chapter 2

The challenges faced to further develop lithium ion batteries are not only limited by materials synthesis and engineering aspects, but also by a fundamental understanding of ionic transport in solid ionic conductors. As outlined in the previous chapter, there have been many experimental techniques developed to probe ionic transport at nanometer length scales, but many of them are mired by difficulty in signal interpretation and extraction. In the following chapter, time-domain EFM with improved time resolution by implementation of a real-time averaging system will be demonstrated on a relevant lithium ion conductor ($LiFePO_4$), and the extracted data will be used to validate theoretical calculations of ionic hopping barriers calculated using density functional theory (DFT). The EFM measurements can be directly correlated with the local composition and structure using scanning electron microscopy (SEM), electron backscatter diffraction (EBSD), and time-of-flight secondary ion mass spectrometry (TOF-SIMS) on the exact same region. This allows for a renewed understanding of lithium ion transport in these types of materials with an emphasis on the collective nature of ionic transport due to the strong ion-ion interactions, as opposed to 'standard' transport models of charge carriers with negligible interactions (e.g. electrons). The following is the integral text from:
Mascaro, Aaron, et al. "Measuring spatially resolved collective ionic transport on lithium battery cathodes using atomic force microscopy." *Nano Letters* 17.7 (2017): 4489-4496.

# 2

# Measuring Spatially Resolved Collective Ionic Transport on Lithium Ion Battery Cathodes using Atomic Force Microscopy

Aaron Mascaro*[1], Zi Wang[2], Pierre Hovington[3], Yoichi Miyahara[1], Andrea Paolella[3], Vincent Gariepy[3], Zimin Feng[3], Tyler Enright[1], Connor Aiken[1], Karim Zaghib[3], Kirk H. Bevan[2], and Peter Grutter[1]

[1] *Department of Physics, McGill University, 3600 rue University, Montreal, Québec H3A2T8, Canada*

[2] *Materials Engineering, McGill University, 3610 rue University, Montreal, Québec H3A0C5, Canada*

[3] *Institut de Recherche d'Hydro Québec, 1800 Boulevard Lionel-Boulet, Varennes, Québec J3X1S1, Canada*

*E-mail: *mascaroa@physics.mcgill.ca*

# Abstract

One of the main challenges in improving fast charging lithium-ion batteries is the development of suitable active materials for cathodes and anodes. Many materials suffer from unacceptable structural changes under high currents and/or low intrinsic conductivities. Experimental measurements are required to optimize these properties, but few techniques are able to spatially resolve ionic transport properties at small length scales. Here we demonstrate an atomic force microscope (AFM)-based technique to measure local ionic transport on $LiFePO_4$ to correlate with the structural and compositional analysis of the same region. By comparing the measured values with density functional theory (DFT) calculations, we demonstrate that Coulomb interactions between ions give rise to a collective activation energy for ionic transport that is dominated by large phase boundary hopping barriers. We successfully measure both the collective activation energy and the smaller single-ion bulk hopping barrier and obtain excellent agreement with values obtained from our DFT calculations.


## 2.1 Introduction

A major challenge in the widespread deployment of sustainable energy sources such as solar and wind is maintaining grid stability due to their time varying nature. Distributed energy storage in electric vehicle batteries is an attractive option to stabilize the grid. Since private vehicles are only used for one hour per day on average [1], batteries in electric vehicles could be connected to the grid for the remaining 23 hours per day. Power utilities could then develop the infrastructure to both charge and discharge the batteries as needed in order to stabilize the grid. A major issue inhibiting widespread consumer acceptance and thus broader deployment of this concept is the low maximum charge rate (c-rate) of the current battery materials and chemistries. The maximum c-rate for most lithium-ion

batteries is typically limited by low electronic and ionic conductivity in the cathode or unacceptable structural changes under high charging currents [2, 3]. In order to improve these transport properties, a fundamental understanding of their underlying mechanisms is essential, but lacking. Measurements of many properties such as activation energy for ionic transport, in particular, differ significantly from values obtained from modeling. Here we show through both experiment and theory that for ionic transport through solids this discrepancy arises due to the collective transport behaviour of the ions.

## 2.2 Ionic Transport

It is generally accepted that lithium transport primarily takes place along 1-dimensional channels oriented along the [010] axis in $LiFePO_4$ (see Figure 2.1A), while cross-channel diffusion is possible by a concerted process involving two lithium ions along the [001] axis; the channels are effectively blocked along the [100] axis making transport impossible in this direction. This was first predicted by calculating the hopping barriers for several possible migration paths and then demonstrated by high-temperature neutron diffraction experiments [4, 5]. Most calculations of the minimum lithium hopping barrier (i.e. along the [010] direction) found values in the range of $\approx 0.3$ eV [6–10], which is significantly smaller than many experimentally measured values ($\approx 0.5$ eV) [4, 11–15]. These calculations typically involve a single lithium ion hopping through an $FePO_4$ lattice and do not take into account the effects of differing polaronic environments as well as neighbouring ions. As we will show, these calculations are extremely sensitive to the surrounding polarons and ions. Their results must also be compared with techniques that measure equivalent phenomena, namely bulk ionic hopping barriers, which we have done using electrostatic force microscopy (EFM) in the time-domain.

The first measurement of ionic conductivity using AFM was demonstrated by Bennewitz and co-workers where the conductivity of $F^-$ ions in $CaF_2$ were probed by measur-

ing the relaxation as a function of time after applying a step potential [16]. More recent developments in AFM-based techniques have aimed to exploit the high spatial resolution afforded by the nanometer-sized AFM tip to correlate local ionic transport with topography. These include: nanoimpedance spectroscopy [17]; electrochemical strain microscopy (ESM) [18, 19], which measures the strain response to applied bias pulses; and time-domain electrostatic force microscopy [20], which measures the relaxation as a function of time similar to the measurement performed by Bennewitz et al. [16] The technique we have employed is an extension of the time-domain method to faster time scales using fast detection electronics and ultra-high frequency AFM cantilevers (see Methods).

Ionic transport in solids is a vacancy-mediated process involving discrete hops by ions in a lattice from their initial sites to neighbouring vacant sites. Applying an electric field to an ionic conductor causes the ions to move in response to the field applied through the material. Ionic hopping leads to, and can thus be observed as, a decay of the internal electric field, $\phi(t)$. On very short timescales (shorter than some cutoff time $t_c$, $t_c$ ~ps according to [21]), the decay is accurately described by a simple exponential as in Eq. 2.1. However, on longer time scales the electric field decays as a stretched exponential as in Eq. 3.1 [21, 22]:

$$\phi(t) = \exp\left[-t/\tau\right] \qquad for \quad t < t_c \tag{2.1}$$

$$\phi(t) = \exp\left[-(t/\tau^*)^\beta\right] \quad for \quad t > t_c, \quad 0 < \beta < 1 \tag{2.2}$$

where $\beta$ is the stretching factor, $\tau$ is the time constant for individual ionic hops at short timescales, and $\tau^*$ is the effective time constant that is observed over time scales larger than $t_c$. This transition is due to the fact that beyond the cutoff time, ionic hopping is no longer random because the probability of a specific hop occurring is influenced by the previous hops of nearby ions. This process was described by the “coupling model" by Ngai [23] and this result (Eqs. 2.1 and 3.1) also appears in the “jump relaxation model"

by Funke [22]. These models are both very similar in many ways and even though their approaches are quite different, they obtain the same result in the time regime of interest for this application [22].

The relaxation time constant ($\tau^*$) varies with temperature according to the Arrhenius law:

$$\tau^* = \tau^*_\infty \exp E^*_a/kT \tag{2.3}$$

where $E^*_a$ is the effective activation energy (for collective transport), $\tau^*_\infty$ is the effective attempt rate, $k$ the Boltzmann constant, and $T$ temperature. Ngai and co-workers showed that $E^*_a$ is not the energy barrier encountered by individual ions, but rather an overall activation energy for collective ionic transport through a material (i.e. the effective activation energy)[21, 23]. This is due to the Coulomb interactions between ions, which cause the local energy landscape to change as neighbouring ions hop into vacant sites. An intuitive description of this process is as follows: an ion that has hopped into a higher energy site can either hop back into its original site to lower the energy, or the surrounding ions can reorganize around it in a correlated relaxation effect. If a backward hop by the initial ion requires less energy than the neighbouring ions relaxing around it, it has a higher probability of occurring. However, on long enough time-scales ( $\gg t_c$), the neighbouring ions reorganize to sufficiently raise the backward hopping barrier so that the less-likely forward hopping event does occur; this gives rise to net transport and effectively dominates any signal related to charge transport in these systems [22, 24]. The single-ion hopping barrier (for hopping through the bulk phase), $E_a$, can be recovered by the following relation:

$$E_a = \beta E^*_a \tag{2.4}$$

Since $E_a$ is the single-ion bulk-phase hopping barrier it can therefore be directly compared with the theoretical energy barrier obtained from modeling. The collective transport activation energy $E^*_a$, however, is the quantity typically measured using conventional

techniques such as impedance spectroscopy. $E_a$ can be recovered from impedance spectroscopy measurements by power law analysis with $\sigma(\omega) \propto (\omega\tau)^n$ where $\beta = 1 - n$ in the intermediate (dispersive) frequency regime, although this analysis is seldom done [22, 23, 25, 26].

## 2.3 Time-domain Electrostatic Force Microscopy

The time-domain electrostatic force spectroscopy technique was originally developed by Schirmeisen et al. [20] where a step potential is applied between a conductive AFM tip and sample and the measured interaction (i.e. change in cantilever resonance frequency) is recorded over time. This technique has been successfully used to measure $Li^+$ transport in $LiAlSiO_4$ with varying degrees of crystallinity, $K^+$ transport in $K_2O{\cdot}2CaO{\cdot}4SiO_2$ (KCS) glass, and $Na^+$ transport in $Na_2O{\cdot}GeO_2$ (NG) glass samples [20, 27–29]. The electric field generated inside the bulk is perpendicular to the surface in the region directly under the tip (Figure 2.1A), which causes ions to move as they attempt to shield the internal field. As charge builds up on the surface directly beneath the AFM tip, the electric field at the tip increases. An increased electric field leads to a stronger attractive tip-sample force, which manifests as a reduction in cantilever resonance frequency. Recording the resonance frequency over time gives the ionic response signal directly that can be fitted to the general form of the ionic response, Eq. 3.1. The ionic conductors probed previously all had relaxation times on the order of seconds and could thus be measured using AFM detection techniques under normal operating conditions. $LiFePO_4$, however, has relaxation times on the order of milliseconds at room temperature, thus requiring high-speed frequency detection electronics and an averaging protocol to reduce noise, which we have developed and implemented (see Methods).

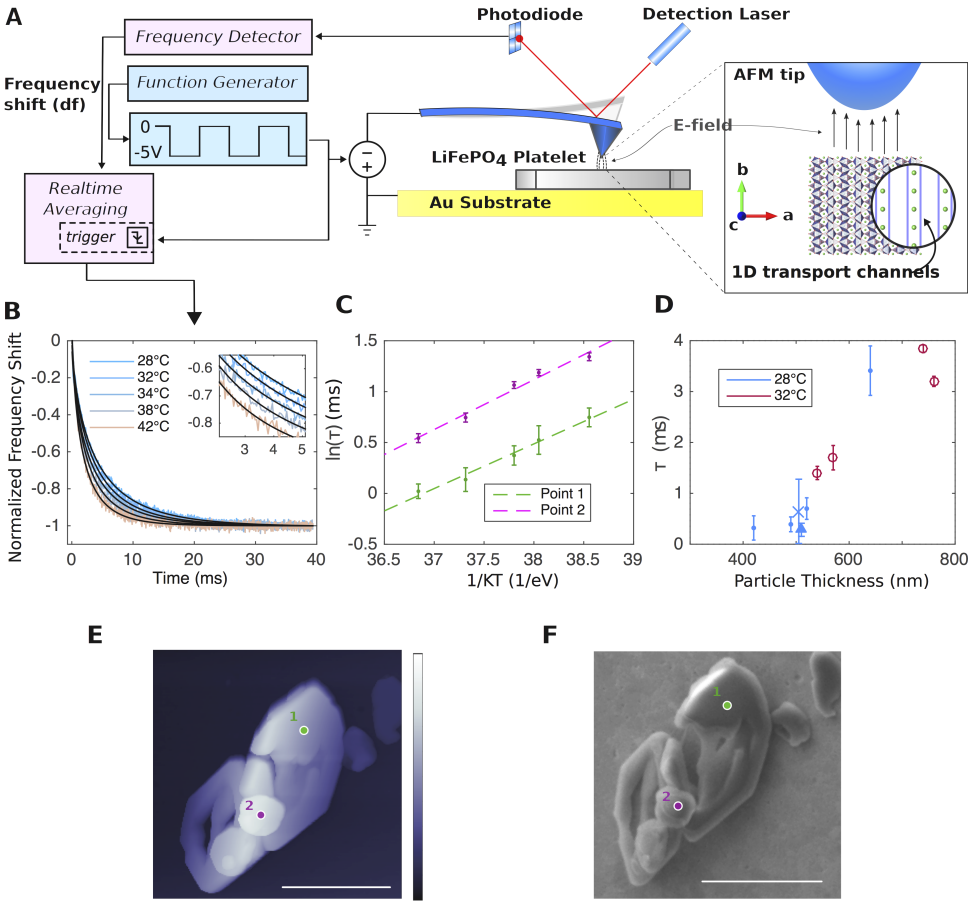


Figure 2.1: Localized time-domain spectroscopy of ionic transport on pure $LiFePO_4$ platelets using AFM. (**A**) Block diagram of AFM electrostatic force spectroscopy measurement. Inset illustrates crystallographic direction with closeup of 1-dimensional transport channels of $LiFePO_4$ platelet with respect to the applied electric field between the AFM tip and back electrode (gold substrate). (**B**) Example of averaged frequency shift vs. time curves (normalized for clarity) obtained after realtime averaging of 100 pulses for slower responses ($< 34°C$) and 700 pulses for faster responses. Black lines are fits obtained using Eq. 3.1, inset shows a close-up of the data and fitted curves from 2ms to 5ms. (**C**) Arrhenius plot of the natural log of the time constants (in ms) obtained from fitted decay curves vs. $1/kT$ and their best-fit lines for both points labelled in (**E**). Error bars represent the standard deviation of time constants obtained at each point for each temperature (see Methods). (**D**) Time constant obtained by fitting frequency shift vs. time curves taken at various points on 4 different particles (indicated by different symbols) plotted against the particle thickness. (**E**) Tapping mode topography AFM image of pure $LiFePO_4$ platelets on gold substrate with probe points labeled. (**F**) SEM image of the same platelets taken while conducting EBSD measurements. All scale bars are $2\mu$m.

### 2.3.1 Measurements

$LiFePO_4$is a well-characterized and relevant material for high power-density batteries and is a good candidate for furthering our understanding of ionic transport in solids. A hydrothermally synthesized $LiFePO_4$ platelet (see Methods) on a gold substrate was probed using the high-speed electrostatic force spectroscopy technique with a step potential of -5 V applied to the tip at 5 different temperatures. The frequency shift values were recorded over 40 ms and averaged 100 to 700 times to obtain an acceptable signal to noise ratio (SNR). The measurements were performed at a tip-sample separation of $\approx 20$ nm. Altering the lift height showed no change on the measured relaxation times, the only change was the absolute value of the saturation frequency shift, which is one of the fit parameters. A block diagram of the probe measurements is shown in Figure 2.1A, while the resulting frequency shift vs. time traces are shown in Figure 2.1B (see Methods).

### 2.3.2 Results

The two points probed on this particle are indicated in the tapping-mode AFM topography image (see Methods) in Figure 2.1E. Hydrothermally synthesized $LiFePO_4$ platelets are known to form with the largest facet in the ac-plane, meaning that the [010] axis in these particles is perpendicular to the surface being probed [30]. This was verified using electron back-scatter diffraction (EBSD, see Figure S1, Appendix A). The scanning electron microscope (SEM) image taken simultaneously is shown in Figure 2.1F. Thus, the 1-dimensional transport channels along the [010] axis are oriented directly along the applied electric field from the AFM tip, illustrated in the inset of Figure 2.1A. The Arrhenius plot of the relaxation time constants $\tau^*$ is shown in Figure 2.1C along with linear fits to the natural log of the relaxation time vs. $1/kT$, which give us the effective attempt rate, $\tau^*_\infty$, and the activation energy for collective ionic transport, $E^*_a$, as per Eq. 2.3.

The collective ionic transport activation energy (0.47 eV) is very similar to values reported from several other techniques for transport along the [010] direction [4, 11–15]. Using Eq. 2.4 we see that the single-ion energy barrier for bulk hopping is around 0.3 eV, which is in very good agreement with values reported from modeling [4]. The results are summarized in Table A.2 (see Table S1, Appendix A, for full fitting results).

After probing several particles with varying thicknesses we observed a clear trend of increasing relaxation time with increasing particle thickness (Figure 2.1D). This indicates that the ionic transport being probed is truly a bulk effect that involves the collective motion of all the ions in the channels in this high lithium-ion concentration limit (i.e. low-vacancy concentration). The electronic conductivity of $LiFePO_4$ is several orders of magnitude higher than the ionic conductivity[13], thus the electronic polarization takes place much faster than the ionic transport probed here. The result is a relaxation signal due entirely to the $Li^+$ transport. Measurements were also done on both conducting and insulating samples without mobile ions present and no response was observed, demonstrating that ionic transport is truly the origin of the observed signal (see Figure S2, Appendix A). To further investigate the observed relaxation, probe experiments were also conducted with -4 V and -5 V applied on the same location (see Figure S3, Appendix A). The time constant and stretching factors obtained after fitting were identical. The only notable effect is a difference in the maximum frequency shift value due to the quadratic dependence of frequency shift on applied voltage (see Methods).

| | **Theory** | **Experiment** |
|---|---|---|
| Collective Activation Energy (eV) | 0.5 - 0.6 | 0.47(7) |
| Bulk Hopping Barrier (eV) | 0.31 - 0.33 | 0.30(4) |
| Collective Diffusivity ($cm^2/s$) | 2 x$10^{-13}$ | 2.8(4) x$10^{-13}$ |
| Bulk Diffusivity ($cm^2/s$) | 1 x$10^{-9}$ | 0.2 $\pm$ 2.0 x$10^{-10}$ |

Table 2.1: Summary of the results obtained for transport along the [010] direction from points 1 and 2 in Figure 2.1E. Theoretical diffusivity values were obtained using Equation (2.5) with a $\nu^*$ value of 2 x$10^{12}s^{-1}$. T = 300K was used for all diffusivity calculations. Uncertainties are the standard deviation values obtained from the parametric bootstrap analysis (see Methods).

A partially delithiated $Li_xFePO_4$ ingot with large grain sizes was synthesized and characterized using various techniques to correlate local structure with local ionic transport properties (see Methods). X-ray diffraction was used to check the bulk phase purity. $LiFePO_4$ and $FePO_4$ phases were identified in $\sim$ 80 : 20 wt.-% ratio, and only trace amounts of $K_2S_2O_8$ were found. Figure 2.2A shows a Scanning Electron Microscope (SEM) secondary-electron image of the sample. The local composition of this exact region of the sample was further investigated using time-of-flight secondary ion mass spectrometry (TOF-SIMS, see Methods). The TOF-SIMS mapping of $Li_7^+$ is shown in Figure 2.2B with an outline of the center region (light region in the SEM image) drawn to guide the eye. Figure 2.2C shows the frequency-modulated AFM (FM-AFM) topography image taken over the same region of interest. The TOF-SIMS mapping clearly shows that region B (also containing point A1 as indicated in the topography image) is lithium-poor while the outer regions (C and A2) are lithium-rich. It has been shown that chemically delithiated $Li_xFePO_4$ spontaneously phase segregates into lithium-rich ($x \approx 1$) and lithium-poor ($x \approx 0$) regions [31], thus the upper and lower regions in the TOF-SIMS data are nearly fully lithiated ($x \approx 1$), while the center region is nearly fully delithiated ($x \approx 0$).

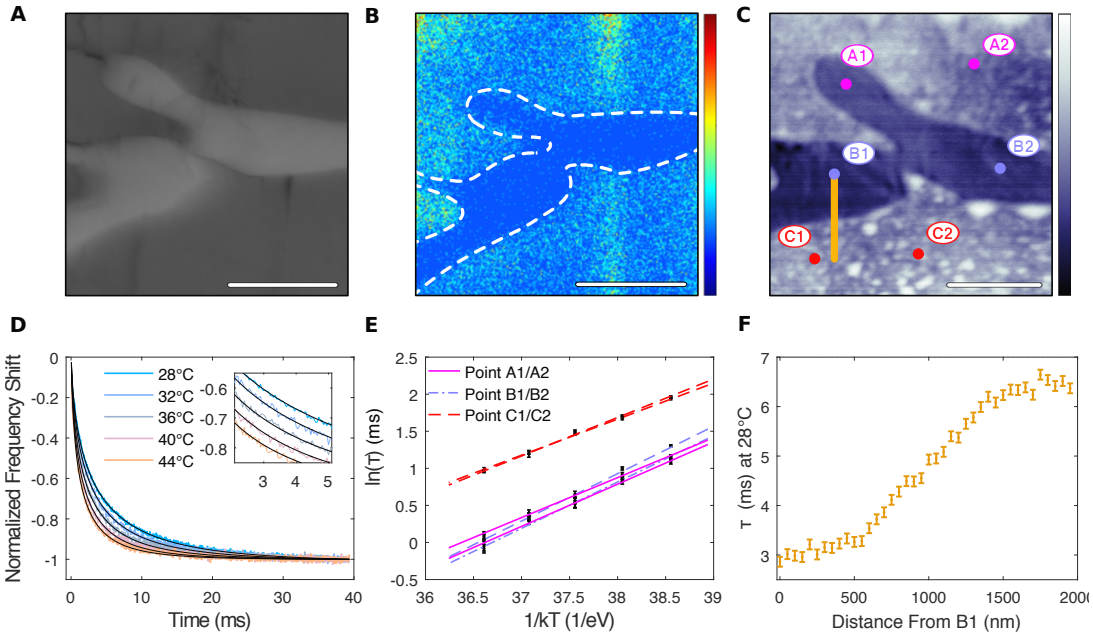


Figure 2.2: Composition and ionic transport on bulk partially delithiated $LiFePO_4$. (**A**) SEM secondary electron image of the region of interest. (**B**) TOF-SIMS map of $Li_7^+$ counts with the grain boundaries outlined (white dashed lines) the colour scale indicates $Li_7^+$ counts/TOF-SIMS extraction from 0 to 0.08, the center region is clearly lithium-poor while the upper and lower regions are lithium-rich. (**C**) FM-AFM topography, vertical scale extends from 0 (black) to 35nm (white). Each labelled point was probed using the electrostatic force spectroscopy technique (see text). (**D**) Example of frequency shift (normalized for clarity) vs. time data for 5 temperature values taken at point A2 in (**C**). Black lines are fits obtained using Eq. 3.1, inset shows a close-up of the data and fitted curves from 2ms to 5ms. (**E**) Arrhenius plot of the natural log of the relaxation times (in ms) obtained from fitted decay curves vs. $1/kT$ and their best-fit lines (solid, dash-dot, and dashed lines) for all points labelled in (**C**). Error bars represent the standard deviation of relaxation times obtained at each point for each temperature (see Methods). (**F**) Spatial variation of relaxation time ($\tau$) taken along line indicated in (**C**) with 50nm spacing between points, error bars are the standard deviations of the measurements done at points B1 and C1 (100$\mu$s). All scale bars are 2$\mu$m.

Each point labeled in Figure 2.2C was probed using the high-speed electrostatic force spectroscopy technique. A summary of the activation energies and bulk hopping barriers measured in each of the three regions (A,B,C) is shown in Table 2.2. The full results including stretching factors and attempt frequencies for all 6 points are found in Table S2 (Appendix A). With the exception of region B, the activation energies and hopping barriers are identical to those measured on the platelet sample. The slightly higher collective activation energy and hopping barrier in region B is most likely due to an increased concentration of antisite defects resulting from the delithiation process. This has been shown to force ions to follow a 2-dimensional transport pathway along the (010) and (001) directions with a higher hopping barrier of $\sim$ 0.36eV, which is consistent with our measured values [32, 33]. This region still displays the collective transport phenomenon, however, with a collective activation energy significantly higher than the bulk hopping-barrier.

| | **A** | **B** | **C** |
|---|---|---|---|
| Collective Activation Energy (eV) | 0.54(3) | 0.62(4) | 0.50(1) |
| Bulk Hopping Barrier (eV) | 0.30(1) | 0.37(1) | 0.32(1) |
| Collective Diffusivity ($cm^2/s$) | 2.3(1) x$10^{-13}$ | 2.2(1) x$10^{-13}$ | 1.08(3) x$10^{-13}$ |
| Bulk Diffusivity ($cm^2/s$) | 2(2) x$10^{-9}$ | 3(6) x$10^{-9}$ | 1.1(8)x$10^{-9}$ |

Table 2.2: Summary of the results obtained for the 3 regions labeled in Figure 2.2C. Average values for each region (i.e. A1 & A2, B1 & B2, C1 & C2) are reported (see Table S2, Appendix A, for full results). Uncertainties are the standard deviation values obtained from the parametric bootstrap analysis (see Methods).

A large variation in relaxation times was also observed between region B and C, which proved useful for demonstrating spatially resolved measurements as shown in Figure 2.2F. This variation is most likely due to elastic coherency strain arising from large concentration gradients (due to phase separation during crystallization), which has been shown to significantly effect local chemical potential and collective ionic diffusivity [34, 35]. The full transition from the characteristic relaxation time of the center grain to that of the outer grain occurs over $\sim$1 micron. This $\sim$1 micron variation across this boundary is also observed in the Kelvin Probe Force Microscopy (KPFM) image (see Figure S3, Appendix

A), indicating that the long length-scale variation is intrinsic to the sample and not the resolution limit of the technique, which has previously been reported as <100nm [27].

EBSD was also conducted on this region and revealed that the $LiFePO_4$ outer regions are not perfectly oriented with the b-axis normal to the surface, but still with a component in that direction (see Figure S5, Appendix A). This demonstrates that 1-dimensional transport can be probed at least in all but the most extreme cases where the 1D channels have no component along the applied field direction. There was some uncertainty in determining the orientation of the $FePO_4$ center region from the EBSD data and so it is not reported here (see Supplementary Materials, Appendix A).

The local diffusivity was calculated using Eq. 2.5, where $\nu^*$ is the attempt frequency ($1/\tau^*$) and $a$ is the intersite distance (3.07Å) [4].

$$D = a^2 \nu^* \exp\left(-E_a/kT\right) \tag{2.5}$$

Using the collective transport activation energies ($E_a^*$) to calculate the collective diffusivity, we obtain the same values as reported from other experimental techniques ($\approx 10^{-13}$ - $10^{-15}$ $cm^2/s$) [37–40]. However, inputting the experimentally determined single-ion bulk hopping barriers and attempt frequencies, the diffusivity values (1 - 3 x$10^{-9}$ $cm^2/s$ from the ingot sample measurements, 0.2 ± 2.0 x$10^{-10}$ $cm^2/s$ from the platelet measurements) are much closer to those calculated from DFT calculations ($\approx 10^{-9}$ $cm^2/s$, described below).

## 2.4 Theory

We performed DFT + U calculations on a $LiFePO_4$ slab ($1 \times 4 \times 2$ unit 'cells) with carefully controlled polaronic and ionic configurations (see Methods). This is illustrated in Figure 2.3 where the system is initialized in a partially lithiated state with part of the

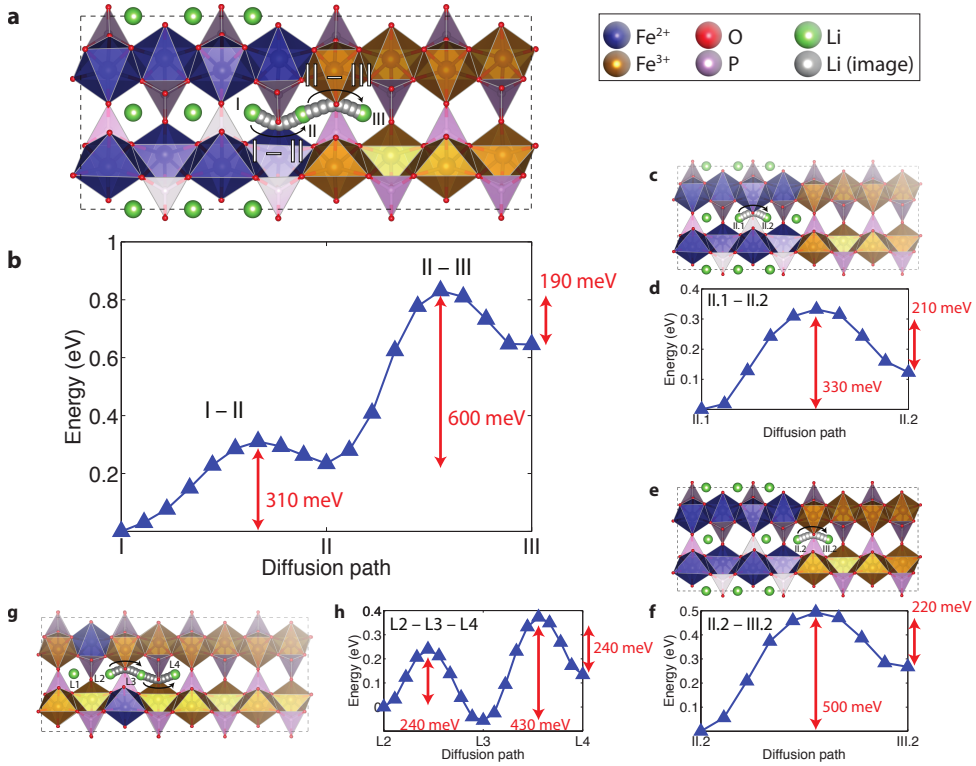


Figure 2.3: The $1 \times 4 \times 2$ slab of $LiFePO_4$ used for the DFT calculations. Lithium ions are coloured in green, oxygen atoms in red, $Fe^{2+}$ (and its $O_6$ octahedral coordination shell) in blue, and $Fe^{3+}O_6$ in orange. In this $1 \times 4 \times 2$ slab, there is a total of 8 layers of sites that can be occupied by Li ions (and a corresponding 8 layers of Fe atoms that can take extra electrons from the Li atoms). To simulate a phase boundary, we added three layers of Li ions and four layers of $Fe^{2+}$ on one half of the slab, with an additional layer of $Fe^{2+}$ added to preserve b-axis directional symmetry, while the other half of the slab remains in $FePO_4$ configuration. Intermediate images of the position of the Li ion during hopping are shown in silver. (**A**) Calculated pathways of the middle rightmost ion hopping from the initial configuration (labelled as I) through the last $Fe^{2+}$ layer to the next site (labelled as II), and further through the $LiFePO_4/FePO_4$ phase boundary to an empty $FePO_4$ site (labelled as III). (**B**) Calculated energies of the I-II and II-III hopping pathways. (**C**) & (**D**) Calculated pathway and energies of the second Li ion hopping after the first ion has hopped from I to II. The endpoints of this pathway are labelled as II.1 and II.2. (**E**) & (**F**) Calculated pathway and energies of the first Li ion hopping from the arrangement in (**B**) and (**D**) through the phase boundary (II.2 to III.2). (**G**) & (**H**) Calculated pathway and energies in the dilute limit, a configuration with just two Li ions. The first ion is kept at the point labelled as L1, and the second ion is moved from L2 to L3 and finally to L4. The induced polarons are kept at their Fe centers as shown in (**G**) throughout the calculation. (**A**), (**C**), (**E**), and (**G**) were produced using VESTA 3 [36].

periodic unit cell in the $LiFePO_4$ phase, and the other part in the $FePO_4$ phase. The $LiFePO_4$ phase is a phase segregated cluster containing Li ions and electrons that reduce the surrounding Fe atoms to a 2+ oxidation state. For collective ionic transport to take place, the leading lithium ion must first hop into the nearest vacant site as in Figure 2.3A. The barrier of the initial hop is highly dependent on the neighbouring polaronic structure (Figure 2.3A and 2.3B): if the first hop is within the $LiFePO_4$ phase (i.e. the neighbouring Fe atoms are in the 2+ state) the barrier is 0.31 eV, whereas if the first hop is across the $LiFePO_4/FePO_4$ phase boundary the barrier is much larger, either 0.6 eV or 0.5 eV depending on whether there is a neighbouring ion or not (Figure 2.3C, 2.3D and 2.3E, 2.3F). Once the initial hop takes place, the initial ion can either hop back into its original site over a small energy barrier ($\approx 0.2$ eV), or the next ion can hop into the now vacant site over an energy barrier of 0.33 eV, which is the bulk diffusion barrier. The lower energy event has a much higher probability of occurring, but does not result in net ionic transport. Over a long enough time period the second process will eventually occur. Once the secondary relaxation takes place the remaining ions can hop along the channel over the lower bulk hopping barriers, which are the values reported from previous calculations of ionic hopping barriers ($\approx 0.3$ eV) [7]. This highlights the sensitivity of hopping barriers to their local environment, which must be accounted for in modeling.

To further elucidate this phenomenon, we have studied a configuration in which there are only two Li ions in the same supercell (Figure 2.3G and 2.3H). In this extreme dilute limit there is no phase boundary, although the Li ions and their polarons will prefer a configuration that minimizes their electrostatic interaction energy. Our calculations indicate that the "L3" configuration as shown in Figure 2.3G is the lowest in energy. The "L2" configuration has a slightly higher total energy, whereas the "L4" configuration is significantly higher in energy. In a fashion analogous to the configurations previously studied, the "L2-L3" barrier is bulk-like whereas the "L3-L4" barrier is significantly higher.

In this configuration, we argue that the higher (and asymmetric) barrier arises mostly due to the Coulomb interactions between the two ions (and their polarons).

Realistically, there are countless different configurations in partially lithiated $LiFePO_4$ and the configurations studied in this work are but a select few of them. The statistical variance can only be revealed by performing an unfeasibly large number of calculations. The studied configurations are, however, self-consistent and both demonstrate the two distinct energy regimes that arise from correlated interactions between multiple lithium ions and their associated polarons. These two regimes (bulk-like diffusion and boundary-crossing events) are present in both ends of the concentration spectrum: high-concentration with phase segregated configurations, and the dilute, two-ion limit.

## 2.5 Discussion

The true meaning of the measured (collective) activation energy and hopping barriers is now more apparent. The $E_a^*$ is the overall activation energy for collective ionic transport, which is dominated (due to the collective motion of ions) by the large local in-channel phase-boundary hopping barriers, whereas the hopping barrier $E_a$ is the energy barrier for a single-ion hopping through the bulk phase. Recall that it is more likely for a leading ion to hop back into its original site over a small energy barrier ($\approx 0.2$ eV) after completing a phase-boundary hop (II-III in Figure 2.3A) than for a second ion to hop into the now vacant site over the larger bulk diffusion barrier ($\approx 0.3$ eV, similar to II.1-II.2 in Figure 2.3C), but only the latter contributes to net ionic transport. This difference in relative probabilities gives rise to a correlated forward backward hopping process, leading to dispersive transport governed by Eq. 3.1 consistent with our experimental observations. This is supported by the jump relaxation model developed by Funke [22] as well as the dispersive transport picture described by Scher and co-workers [24].

Recent measurements have shown that a solid solution phase forms during the non-

equilibrium stage that occurs during fast charge/discharge [41, 42]. Our study indicates that when there is no net external field present, the partially lithiated system will favour phase segregation and clustering on the nanoscale along the 1-dimensional transport channels with high initial energetic barriers due to the local phase boundaries. When a strong external field is applied during the measurements (as in charge/discharge) the dispersive behaviour of the Li ions will lead to a metastable state where the ionic distribution is such that a solid solution of $LiFePO_4/FePO_4$ forms. Therefore, we have shown that the initial two-phase state and its corresponding high initial hopping barrier lead to the measured collective activation energies, while the hopping barriers in the solid solution state are the bulk hopping barriers and thus lead to the observed fast charge/discharge rates.

## 2.6 Conclusion

We have demonstrated an AFM-based electrostatic force spectroscopy technique to probe local ionic transport properties with high spatial resolution on a $LiFePO_4$ sample. We have successfully correlated these measurements with the local composition and crystallographic structure using SEM, EBSD, and TOF-SIMS. The measured activation energies for collective ionic transport along the [010] direction were in good agreement with typical values obtained using other techniques ($\approx 0.5$ eV) [4, 11–15]. Our DFT calculations show that a higher hopping barrier is present as lithium ions cross the $LiFePO_4/FePO_4$ phase boundary along the [010] direction ($0.5-0.6$ eV), which we have identified as the origin of the collective transport activation energy. Moreover, our DFT calculations indicate that the hopping barrier for single-ion transport through the bulk $LiFePO_4$ phase along the [010] direction is $\approx 0.3$ eV, which has also been reported in the literature [6–9]. Through several orders of magnitude improvement in time resolved AFM measurements, we have demonstrated the ability to extract these single-ion bulk hopping barriers from collective ion motion and obtained values in excellent agreement with both collective ion and

single-ion calculations. In conclusion, our AFM-based technique allows for direct correlation of transport properties with the local structure measured using other techniques. By combining these techniques we have refined our understanding of ionic transport to better engineer active materials for high c-rate and high-power lithium-ion batteries. These materials will play a crucial role in the widespread deployment of renewable energy generation and fully electric vehicles with fast charge and discharge requirements.

## Supporting Information - Appendix A

Experimental methods, Materials preparation

Figures:

1. EBSD data
2. Ionic response validation measurements
3. Ionic response at differing applied voltages
4. KPFM data
5. KPFM energy level diagrams
6. Ingot sample EBSD data
7. TOF-SIMS data
8. LiFePO4 platelet probe data
9. Ingot sample probe data

The authors declare no competing financial interests.

## Acknowledgements

The authors acknowledge financial support from the Natural Sciences and Engineering Research Council of Canada and computational support from Canada Foundation for Innovation, Compute Canada, and Calcul Quebec. Z.W. acknowledges financial support from Mitacs of Canada, and Fonds Québécois de la Recherche sur la Nature et les Technologies. A.M. would like to acknowledge technical support from Percy Zahl (Brookhaven National Laboratory) in customizing the GXSM software to perform the AFM spectroscopy measurements.

# References

[1] Adella Santos et al. *Summary of travel trends: 2009 national household travel survey.* Tech. rep. FHWA-PL-ll-022. Washington, D.C.: U.S. Department of Transportation, 2011.

[2] Byoungwoo Kang and Gerbrand Ceder. "Battery materials for ultrafast charging and discharging". In: *Nature* 458.7235 (2009), pp. 190–193.

[3] Xiao Hua Liu et al. "Ultrafast electrochemical lithiation of individual Si nanowire anodes". In: *Nano Lett.* 11.6 (2011), pp. 2251–2258.

[4] Dane Morgan, Anton Van der Ven, and Gerbrand Ceder. "Li conductivity in Li x MPO 4 (M= Mn, Fe, Co, Ni) olivine materials". In: *Electrochem. Solid-State Lett.* 7.2 (2004), A30–A32.

[5] Shin-ichi Nishimura et al. "Experimental visualization of lithium diffusion in $Li_xFePO_4$". In: *Nat. Mater.* 7.9 (2008), pp. 707–711.

[6] Jianjun Yang and John S Tse. "Li ion diffusion mechanisms in $LiFePO_4$: an ab initio molecular dynamics study". In: *J. Phys. Chem. A* 115.45 (2011), pp. 13045–13049.

[7] Gopi Krishna Phani Dathar et al. “Calculations of Li-ion diffusion in olivine phosphates”. In: *Chem. Mater.* 23.17 (2011), pp. 4032–4037.

[8] Jaekwang Lee, Stephen J Pennycook, and Sokrates T Pantelides. “Simultaneous enhancement of electronic and Li+ ion conductivity in LiFePO4”. In: *Appl. Phys. Lett.* 101.3 (2012), p. 033901.

[9] Kyu-Sung Park et al. “Enhanced charge-transfer kinetics by anion surface modification of LiFePO4”. In: *Chem. Mater.* 24.16 (2012), pp. 3212–3218.

[10] M Saiful Islam et al. “Atomic-scale investigation of defects, dopants, and lithium transport in the LiFePO4 olivine-type battery material”. In: *Chem. Mater.* 17.20 (2005), pp. 5085–5092.

[11] J Molenda et al. “Diffusional mechanism of deintercalation in LiFe 1- y Mn y PO 4 cathode material”. In: *Solid State Ionics* 177.26 (2006), pp. 2617–2624.

[12] R Amin et al. “Ionic and electronic transport in single crystalline $LiFePO_4$ grown by optical floating zone technique”. In: *Solid State Ionics* 179.27 (2008), pp. 1683–1687.

[13] Ruhul Amin, Palani Balaya, and Joachim Maier. “Anisotropy of electronic and ionic transport in LiFePO4 single crystals”. In: *Electrochem. Solid-State Lett.* 10.1 (2007), A13–A16.

[14] Sung-Yoon Chung, Jason T Bloking, and Yet-Ming Chiang. “Electronically conductive phospho-olivines as lithium storage electrodes”. In: *Nat. Mater.* 1.2 (2002), pp. 123–128.

[15] Jiying Li et al. “Lithium ion conductivity in single crystal LiFePO 4”. In: *Solid State Ionics* 179.35 (2008), pp. 2016–2019.

[16] R Bennewitz, M Reichling, and E Matthias. "Force microscopy of cleaved and electron-irradiated CaF 2 (111) surfaces in ultra-high vacuum". In: *Surf. Sci.* 387.1 (1997), pp. 69–77.

[17] Rui Shao, Sergei V Kalinin, and Dawn A Bonnell. "Local impedance imaging and spectroscopy of polycrystalline ZnO using contact atomic force microscopy". In: *Appl. Phys. Lett.* 82.12 (2003), pp. 1869–1871.

[18] Nina Balke et al. "Local detection of activation energy for ionic transport in lithium cobalt oxide". In: *Nano Lett.* 12.7 (2012), pp. 3399–3403.

[19] Shan Yang et al. "In situ studies of lithium-ion diffusion in a lithium-rich thin film cathode by scanning probe microscopy techniques". In: *Phys. Chem. Chem. Phys.* 17.34 (2015), pp. 22235–22242.

[20] A Schirmeisen et al. "Probing ion transport at the nanoscale: Time-domain electrostatic force spectroscopy on glassy electrolytes". In: *Appl. Phys. Lett.* 85.11 (2004), pp. 2053–2055.

[21] KL Ngai, Y-N Wang, and LB Magalas. "Theoretical basis and general applicability of the coupling model to relaxations in coupled systems". In: *J. Alloys Compd.* 211 (1994), pp. 327–332.

[22] K Funke. "Jump relaxation in solid electrolytes". In: *Prog. Solid State Chem.* 22.2 (1993), pp. 111–195.

[23] KL Ngai and O Kanert. "Comparisons between the coupling model predictions, Monte Carlo simulations and some recent experimental data of conductivity relaxations in glassy ionics". In: *Solid State Ionics* 53 (1992), pp. 936–946.

[24] Harvey Scher, Michael F Shlesinger, and John T Bendler. "Time-scale invariance in transport and relaxation". In: *Phys. Today* 44.1 (1991), pp. 26–34.

[25] AS Nowick and BS Lim. "Analysis of ac conductivity data for Na2O· 3SiO2 glass by stretched exponential and Jonscher power-law methods". In: *J. Non-Cryst. Solids* 172 (1994), pp. 1389–1394.

[26] Andrew K Jonscher. "Dielectric relaxation in solids". In: *J. Phys. D: Appl. Phys.* 32.14 (1999), R57.

[27] Andre Schirmeisen et al. "Ion Jump Dynamics in Nanoscopic Subvolumes Analyzed by Electrostatic Force Spectroscopy". In: *Z. Phys. Chem. (Muenchen, Ger.)* 224.10-12 (2010), pp. 1831–1852.

[28] Ahmet Taskiran et al. "Time-domain electrostatic force spectroscopy on nanostructured lithium-ion conducting glass ceramics: analysis and interpretation of relaxation times". In: *Phys. Chem. Chem. Phys.* 11.26 (2009), pp. 5499–5505.

[29] André Schirmeisen et al. "Fast interfacial ionic conduction in nanostructured glass ceramics". In: *Phys. Rev. Lett.* 98.22 (2007), p. 225901.

[30] Kaoru Dokko et al. "Particle morphology, crystal orientation, and electrochemical reactivity of LiFePO 4 synthesized by the hydrothermal method at 443 K". In: *J. Mater. Chem.* 17.45 (2007), pp. 4803–4810.

[31] Akiho Nakamura et al. "Phase Boundary Structure of LixFePO4 Cathode Material Revealed by Atomic-Resolution Scanning Transmission Electron Microscopy". In: *Chem. Mater.* 26.21 (2014), pp. 6178–6184.

[32] Craig AJ Fisher, Veluz M Hart Prieto, and M Saiful Islam. "Lithium battery materials Li M PO4 (M= Mn, Fe, Co, and Ni): insights into defect association, transport mechanisms, and doping behavior". In: *Chem. Mater.* 20.18 (2008), pp. 5907–5915.

[33] Andrea Paolella et al. "Cation exchange mediated elimination of the Fe-antisites in the hydrothermal synthesis of LiFePO 4". In: *Nano Energy* 16 (2015), pp. 256–267.

[34] Daniel A Cogswell and Martin Z Bazant. "Coherency strain and the kinetics of phase separation in LiFePO4 nanoparticles". In: *ACS Nano* 6.3 (2012), pp. 2215–2225.

[35] Michael J Welland et al. "Miscibility Gap Closure, Interface Morphology, and Phase Microstructure of 3D Li x FePO4 Nanoparticles from Surface Wetting and Coherency Strain". In: *ACS Nano* 9.10 (2015), pp. 9757–9771.

[36] Koichi Momma and Fujio Izumi. "VESTA 3 for three-dimensional visualization of crystal, volumetric and morphology data". In: *J. Appl. Crystallogr.* 44.6 (2011), pp. 1272–1276.

[37] Pier Paolo Prosini et al. "Determination of the chemical diffusion coefficient of lithium in LiFePO 4". In: *Solid State Ionics* 148.1 (2002), pp. 45–51.

[38] Siqi Shi et al. "Enhancement of electronic conductivity of LiFePO 4 by Cr doping and its identification by first-principles calculations". In: *Phys. Rev. B* 68.19 (2003), p. 195108.

[39] Yong-Nian Xu et al. "Electronic structure and electrical conductivity of undoped LiFePO4". In: *Electrochem. Solid-State Lett.* 7.6 (2004), A131–A134.

[40] AV Churikov et al. "Determination of lithium diffusion coefficient in LiFePO 4 electrode by galvanostatic and potentiostatic intermittent titration techniques". In: *Electrochim. Acta* 55.8 (2010), pp. 2939–2950.

[41] Hao Liu et al. "Capturing metastable structures during high-rate cycling of LiFePO4 nanoparticle electrodes". In: *Science* 344.6191 (2014), p. 1252817.

[42] Karena W Chapman. "Emerging operando and x-ray pair distribution function methods for energy materials development". In: *MRS Bull.* 41.03 (2016), pp. 231–240.

# Preface to Chapter 3

In the previous chapter, time-domain EFM was used to study ionic conductivity in pure $LiFePO_4$, which is a relatively slow ionic conductor when compared with many newer materials [97]. To study ionic transport in faster materials using time-resolved EFM will, of course, require improved time resolution. Fig. 2.4 provides an outline of the temporal resolution required to measure various properties and their approximate timescales.

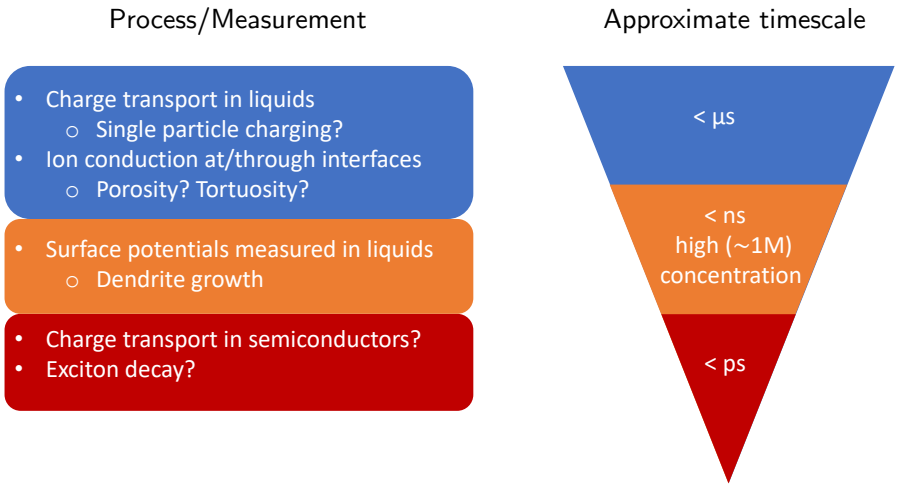


Figure 2.4: Approximate timescale/required temporal resolution to measure various processes/properties.

Charge transport measurements in liquid environments via EFM would unlock the ability to measure charging times of single particles (such as those found in real-world batteries) and correlate these with properties such as interfacial porosity and tortuosity, while measuring *surface potentials* in liquids would allow for direct characterization of dendrite and SEI formation. In the sub-picosecond time-regime we see a variety of electronic/excitonic transport properties, which are generally probed using optical tech-

niques instead of voltage-driven measurements. Optical-driven measurements are, at present, less relevant for ionic transport processes, which (typically) occur at timescales orders of magnitude slower than electronic/excitonic transport. Thus, in the following chapter we will review a variety of time-resolved EFM techniques that have applications to measuring ionic transport (i.e. voltage-pulsed techniques). Standard time-domain EFM, voltage-pulse averaging (a new technique described herein), fast free time-resolved EFM, phase-kick EFM, and intermodulation spectroscopy will all be discussed in detail, along with their respective limitations and challenges in applications to ionic transport. The following is the integral text from:

Mascaro, Aaron, et al. "Review of time-resolved non-contact electrostatic force microscopy techniques with applications to ionic transport measurements" *Beilstein Journal of Nanotechnology*, 10.1 (2019): 617-633.

# 3

# Review of time-resolved non-contact electrostatic force microscopy techniques with applications to ionic transport measurements

Aaron Mascaro*, Yoichi Miyahara, Tyler Enright, Omur E. Dagdeviren, and Peter Grütter

*Department of Physics, McGill University, 3600 rue University, Montreal, Québec H3A2T8, Canada*

*E-mail: *mascaroa@physics.mcgill.ca*

## 3.1 Abstract

Recently, there have been a number of variations of electrostatic force microscopy (EFM) that allow for the measurement of time-varying forces arising from phenomena such as ion transport in battery materials or charge separation in photovoltaic systems. These forces reveal information about dynamic processes happening over nanometer length scales due to the nanometer-sized probe tips used in atomic force microscopy. Here, we review in detail several time-resolved EFM techniques based on non-contact atomic force microscopy, elaborating on their specific limitations and challenges. We also introduce a new experimental technique that can resolve time-varying signals well below the oscillation period of the cantilever and compare and contrast it with those previously established.

## 3.2 Introduction

Since the inception of the atomic force microscope (AFM) a variety of techniques have been developed aimed at measuring local electronic and ionic properties on a wide range of samples. By carefully controlling the electric field between the tip and sample many properties can be measured with high spatial resolution including static properties such as local contact potential difference (which can be used to extract the local work function) [1] and local piezoelectric response [2], and dynamic properties such as the charging and decay times of photoexcited carriers [3–6], and local activation energies for ionic transport [7, 8]. These measurements play a crucial role in understanding local charge dynamics and composition of numerous materials with applications across many fields including energy generation and storage. Capturing time-resolved dynamic processes at ever-decreasing time and length scales has become of increased interest in recent years due to the importance of understanding transport properties of real-world, often heterogeneous materials relevant for energy generation and storage. A number of AFM techniques

have been developed to study relevant materials including: time-resolved EFM to measure photoexcited charge accumulation and charge transfer [6, 9–11], time-domain EFM to measure ionic transport [7, 12], time-resolved electrochemical strain microscopy (ESM) to measure ionic transport [8, 13], various time-resolved Kelvin probe force microscopy (KPFM) techniques that utilize either optical pump-probe or advanced signal processing to measure time-resolved surface potentials [14–18], and other techniques that exploit non-linear signal mixing or heterodyning to extract the time evolution of the tip-sample interaction [19, 20]. All of these techniques share a common goal of furthering the understanding of charge generation and transport processes to develop a clear picture of the underlying mechanisms that govern them. This requires an extensive toolbox of experimental techniques of which EFM-based ones will most certainly play an essential role.

In this review we explore in detail several techniques that allow for time-resolved electrostatic force measurements to probe ionic transport. More specifically, these techniques are able to capture time-varying changes in the tip-sample coupling due to the movement of mobile ions within the sample in the sample volume directly underneath the probe tip. The ionic motion is initiated by an electric potential applied across the sample; the movement of mobile ions leads to a change in the tip-sample capacitance and, thus, a change in the electrostatic force acting on the cantilever probe tip. The electrostatic tip-sample force is proportional to the capacitance gradient $\frac{\partial C}{\partial z}$ times the square of the applied potential $V(t)^2$, i.e. $F \sim \frac{\partial C(t)}{\partial z} V(t)^2$. In ionic transport measurements it is the time-dependence of the capacitance $C(t)$ that is to be measured; however, this is not usually a known quantity, therefore in order to validate a technique for suitability in measuring this quantitatively, a known time-varying voltage with the same functional time-dependence that mimics the expected $C(t)$ can be used instead. This allows for a quantitative assessment of the extracted parameters and is the method used to validate

each technique discussed herein.

Since there are a multitude of similar techniques, each with their own clever implementations and analyses, we have restricted our review to exclude all pump-probe and KPFM techniques as these are generally unsuitable for probing ionic transport. For a recent review of all KPFM and related techniques, we refer the reader to Ref. [21].

We begin by describing the direct time-domain method and its limitations, we then introduce a new technique we refer to as voltage-pulse averaging EFM, and then continue to explain and examine three other techniques with applications to ionic transport measurements, specifically: fast free time-resolved EFM [22], phase-kick EFM [23], and intermodulation spectroscopy [20]. Table 3.1 lists these techniques along with their respective time resolutions (smallest value demonstrated), limitations, and strengths.

| **Technique** | **Time Resolution** | **Limitations** | **Strengths** |
|---|---|---|---|
| Direct Time-Domain | $>2$ $\mu$ s | Resonance frequency and detection bandwidth limit time resolution. | Simple implementation. |
| Voltage-pulse averaging EFM | $\sim$ 200 ns | Significant averaging time.<br><br>Difficulty in extracting stretched exponential.<br><br>Functional form of C(t) must be known. | Simple implementation.<br><br>Time resolution not limited by detection bandwidth. |
| Fast free time-resolved EFM [22] | $\sim$ 10 ns | Slowly varying relationship between $\tau$ and extracted signal $t_{fp}$ for sub-cycle time constants.<br><br>Difficulty in extracting stretched exponential for small time constants. | Excellent spatial resolution.<br><br>Fast imaging times with simultaneous acquisition and analysis. |
| Phase-kick EFM [23] | $\sim$ 35 ns | Requires precisely phase-locked excitation signals.<br><br>Tip-sample force gradient must be approximately constant over oscillation cycle. | Strong signal to noise ratio due to averaging.<br><br>Time resolution not limited by detection bandwidth. |
| Intermodulation Spectroscopy | $\sim$ 30 ns | High Q-factor cantilevers result in lower signal to noise ratio.<br><br>A time dependent capacitance will likely lead to a complicated analytic representation needed to extract the system's time-evolution. | Time resolution theoretically only limited by measurement time.<br><br>Full time-evolution can be captured using only a single measurement. |

Table 3.1: Overview of the five techniques explored in this review. Time resolution is the smallest demonstrated value.

## 3.3 Direct time-domain EFM

### 3.3.1 Background

Direct time-domain EFM measurements are the most straightforward methods of measuring time-varying interactions. In the commonly used frequency-modulated AFM configuration, the resonance frequency of an oscillating cantilever is measured while the probe tip interacts with a surface [24]. The interactions are purely electrostatic – in other words, the tip and sample form a capacitor. The oscillation of the cantilever can therefore be modulated by the electric field between the tip and sample, which may vary with time. The first use of an AFM to measure the time evolution of sample charge carriers was reported by Schönenberger and Alvarado [25]. They first applied a voltage pulse between the tip and sample to inject charge into the sample. They subsequently measured the (ac) electrostatic force as a function of time using a lock-in amplifier where the observed force decayed over several seconds.

In the case of photovoltaic samples, simply shining light on them photoexcites charge carriers, which can result in charge build-up in the sample at the location of the AFM tip if an appropriate voltage is applied across the tip-sample gap. Measuring the resonance frequency shift as a function of time after the light is turned on/off then allows for the charging/discharging time to be directly acquired, revealing information about charge generation and transport in the sample. This was first performed by Krauss et al., where they observed charging of photoexcited CdSe nanocrystals by direct frequency shift measurements after illumination [26].

The concept outlined above can be applied to measure ionic transport in ionic conducting materials as well. To probe ionic transport a step potential is applied between

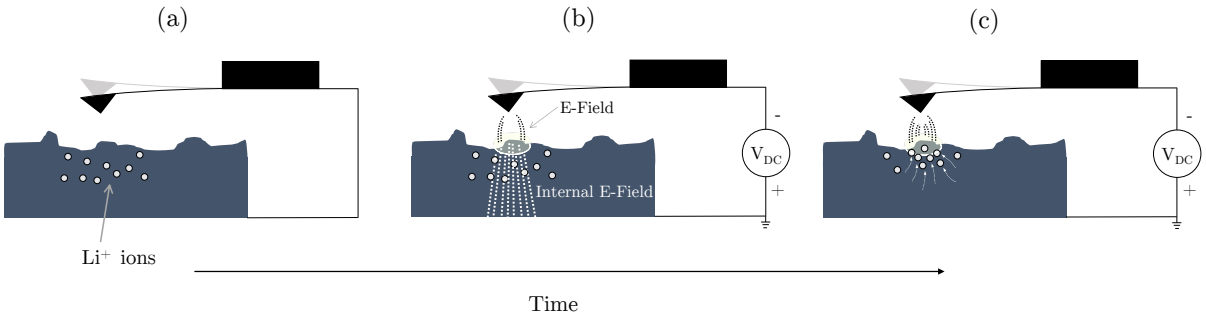


Figure 3.1: Illustration of ionic transport measurements in the time domain. (a) A conducting AFM tip is brought close (typically from ∼1-20 nm) to the surface of a sample containing mobile ions ($Li^+$ in this case). (b) A step potential ($V_{DC}$) is applied between the tip and back electrode, creating an electric field that extends through the sample. (c) The mobile ions move towards the tip (in the case of a negative tip bias and grounded back electrode), shielding the internal electric field.

the AFM tip and a conducting back electrode, creating an electric field across the tip-sample gap and through the sample, illustrated in Figure 3.1(b). The mobile ions inside the sample move in response to this field over time, resulting in a change in the field (and field gradient) at the tip as illustrated in Figure 3.1(c). This changing electric field as a result of screening by the mobile ions leads to a shift of the cantilever resonance frequency as a function of time, which can be directly measured, typically by using a phase-locked loop (PLL). This was first performed by Bennewitz et al. to measure the mobility of $F^-$ vacancies in a $CaF_2$ crystal [27]. Schirmeisen et al. later improved the technique by performing the measurements at various temperatures to extract the activation energy for ionic transport in $Li^+$ conducting glasses [7]. To further expand the power of the technique, Mascaro et al. developed a real-time averaging system used in conjunction with a fast (high-bandwidth) PLL to improve the time resolution [12]. This enabled ionic transport measurements to be performed on lithium iron phosphate ($LiFePO_4$), a relevant lithium-ion battery cathode material. In this configuration the time resolution (and thus the fastest ionic conductor that can be measured) is limited by the time response of the PLL, which depends on many parameters including the free resonance frequency of the cantilever as well as the various PLL settings.

### 3.3.2 Limitation - Direct Frequency Detection

A critically damped second order PLL (i.e. optimized settings) has an exponentially decaying time response to abrupt changes in the frequency being tracked (the center frequency, $f_0$) [28]. The response time-constant of the phase detector is determined directly by the center frequency: $\tau_{PD} = 1/f_0$. Thus, the theoretical minimum response time to achieve >95% tracking is 3 cycles. This is difficult to realize in practice as it neglects amplification/filtering before and after the phase detector and other non-ideal effects such as jitter and noise. The overall response time of the system ($\tau_{PLL}$, inversely proportional to the overall bandwidth) serves as a more practical metric as it takes all contributions into account. This can either be measured by stepping the frequency of a known signal and measuring the response time or in the case of some digital PLLs by a built-in function that models the response [29].

In general, ionic transport in solid ionic conductors follows a stretched-exponential time response to applied electric fields:

$$\phi(t) \;=\; \phi_0 \exp\left[-(t/\tau^*)^{\beta}\right] \qquad 0 < \beta < 1 \tag{3.1}$$

where $\phi$ represents the internal electric field, $\phi_0$ is the initial field strength, $\beta$ is the stretching factor, and $\tau^*$ is the collective (or overall) time constant for the response [30]. Note that this stretched exponential behaviour is due to the correlated nature of ion transport, which is dependent on the atomic and electronic structure of the material and not necessarily due to a distribution of relaxation times [31]. Nonetheless, this complicates time-domain measurements of ionic transport as the functional form of the relaxation must be fully captured in order to reliably extract the relevant parameters, namely $\tau^*$ and $\beta$. With slow ionic relaxation times (>ms) and typical operating (scanning) parame-

ters (bandwidth ∼100 Hz) the PLL response will not affect the extracted values obtained from directly fitting the data. However, as the relaxation time approaches the response time of the PLL, the output signal will become a convolution of the PLL response function and the ionic relaxation. This makes any quantification of the transport properties challenging.

To investigate the effect of $\tau_{PLL}$ on the ability to extract parameters from measured signals, a digitially synthesized voltage waveform varying in time as a stretched exponential (Equation 3.1, $\beta = 0.7$) was applied between a Pt coated AFM-tip and a gold substrate (separated by ∼20 nm) under high vacuum ($\sim 10^{-6}$ mbar, Jeol JSPM-5200) to simulate ionic transport in the sample with a known decay time constant. Note that a separation $\gtrsim$1 nm is necessary in general to ensure that no charge is injected into the sample. In this case, the electric field follows the applied voltage instantaneously on the relevant time scales. For each programmed time constant (from 0.1 - 10 ms), the voltage was varied from 0 V initially to 5 V; the measured response is shown in Figure 3.2(a) where the blue curve is the result of the smoothly varying stretched-exponential applied voltage. The orange curve is the result of applying an initial instantaneous jump from 0 to 2.5 V followed by a stretched-exponential increase to 5 V. This is intended to mimic experimental conditions as the step voltage applied causes an initial jump in the resonance frequency (due to the stepped electric field between the tip and sample before the ions respond) followed by the slow sample relaxation (as the ions move to shield the initial electric field). Since the actual time constant is given by the synthesized voltage waveform, the percent error can be directly calculated from the fit results. Note that since the frequency shift is quadratic in voltage and it is the voltage being changed here, we must first take the square root of the data before fitting. The results are shown in Figure 3.2(b) where the shaded area is the region for which $\tau^* < \tau_{PLL} \approx 600\mu s$. To replicate

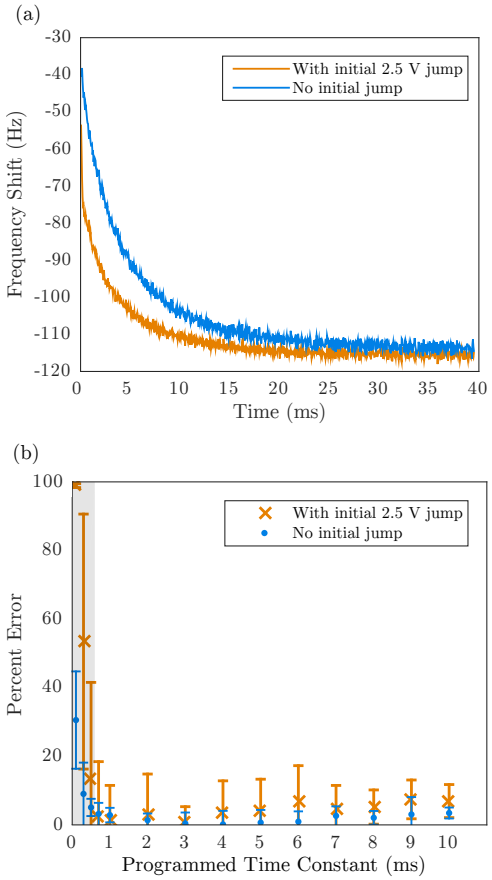


Figure 3.2: (a) AFM frequency shift response to stretched-exponential voltage pulses (from 0 to 5 V) with and without an intial 2.5 V jump. (b) Percent error of fitted relaxation time constant ($\tau^*$) as a function of relaxation time constant of applied voltage pulse for fixed PLL response time ($\tau_{PLL}$). Shaded region shows where $\tau^* < \tau_{PLL}$.

measurement conditions, 100 waveforms were applied as a pulse train (50% duty cycle) and the response signals were averaged together using our realtime averaging system to reduce noise (described in Ref [12]). In both cases (with and without the initial jump) we are able to accurately extract the relaxation time constant; the initial jump only leads to a higher statistical uncertainty, which is due to the slow initial response of the PLL relative to the fast jump from 0 to 2.5 V. This becomes especially apparent for $\tau^* \sim \tau_{PLL}$. The stretching factor displays exactly the same behaviour (not shown).

Clearly the practical limitation for high fidelity measurements is determined by $\tau_{PLL}$ as the percent error increases drastically for $\tau^* < \tau_{PLL}$. Simply increasing the PLL bandwidth will decrease $\tau_{PLL}$ although this will result in higher noise due to the less aggressive filtering. By taking a larger number of averages, the same signal to noise ratio (SNR) can be achieved, however the cantilever resonance frequency will ultimately determine the minimum $\tau_{PLL}$. Empirically we have found that the minimum PLL response time achievable is $\tau_{PLLmin} \approx 10 \times 1/f_0$. The highest resonance frequency cantilevers currently commercially available have frequencies of $f_0 \approx 5$ MHz, thus the realistic minimum measurable relaxation time by this technique is $\sim 2$ $\mu$s.

## 3.4 Voltage-pulse averaging EFM

### 3.4.1 Motivation

Improving the time resolution beyond the limitations of direct time-domain measurements is possible in several ways using careful instrumentation and signal analysis. The basic concept is to detect (using a slow detector) the change in average response of the sample due to a change in the frequency (or repetition rate, delay time etc.) of an excitation signal. This is also the basis for pump-probe spectroscopy, which is routinely employed to measure ultrafast dynamics of condensed matter systems using a variety of pulsed light sources [32–35]. In some systems the probe pulse is not even necessary as the pump both excites the response being investigated and engages the probing behaviour simultaneously. One example of this is in time-resolved Kelvin probe force microscopy (KPFM) experiments that measure the surface photovoltage of a sample as a function of time after a light source is pulsed. This was first implemented by Takihara et al. to measure the photovoltage dynamics of a sample at time scales faster than the KPFM

feedback loop can track [36]. In this measurement mode, the tip-sample coupling is in an 'always-on' state and the time-resolution is achieved by modulating the length of time the system is allowed to decay (i.e. the pulse-off time). The minimum time resolution is no longer limited by the detection electronics, but instead is theoretically limited only by the thermal noise of the cantilever [18]. This principle can be easily extended to ionic systems (such as those discussed previously) by simply replacing the pulsed light source with a pulsed voltage. In this case, the electric field engages the tip-sample coupling and simultaneously moves the mobile ions in the substrate, which leads to a changing tip-sample capacitance. Since the applied voltage controls the tip-sample coupling, turning the voltage off decouples the tip from changes occurring in the sample, thus the ionic transport is only probed during the pulse-on time, which can be directly controlled. Finding a relationship between the average frequency shift $\langle f_0 \rangle$ and the relaxation time constant of the sample $\tau^*$ as a function of the pulse width $T$ then allows for the sample transport dynamics to be extracted beyond the time resolution of the detection electronics. To relate the frequency shift of a cantilever to the tip-sample forces for FM-AFM, we turn to canonical perturbation theory using action angle variables similar to the work done by Giessibl [37].

### 3.4.2 Derivation using Canonical Perturbation Theory

Starting with the Hamiltonian for a harmonic oscillator and using a capacitive force perturbation Hamiltonian ($\Delta H = \frac{1}{2}CV^2$), we transform the momentum and position variables to action and angle variables: ($p$,$q$) $\rightarrow$ ($\alpha$,$\beta$), where the first order perturbation solution for the angle variable $\beta_1$ (not to be confused with the earlier use of $\beta$ as the exponential stretching factor) has the property:

$$\dot{\beta_1} = \left. \frac{\partial \Delta H(\alpha, \beta, t)}{\partial \alpha} \right|_0 \tag{3.2}$$

where the $\cdot$ denotes the time derivative and the subscript 0 indicates that the $\alpha$ and $\beta$ are to be replaced by their unperturbed, constant values ($\alpha_0$,$\beta_0$) after differentiation [38].

Writing $q$ in terms of the action and angle variables explicitly:

$$q \;=\; \sqrt{\frac{2\alpha}{m\omega^2}}\sin(\omega t+\beta) \tag{3.3}$$

we see that $\dot{\beta}$ is the time derivative of the phase change due to the perturbing force. Taking the average therefore gives us the steady-state frequency shift $\langle\Delta f\rangle = \langle\dot{\beta}\rangle$, which can easily be measured. Re-writing:

$$\left.\frac{\partial\Delta H(\alpha,\beta,t)}{\partial\alpha}\right|_0 \;=\; \frac{\partial\Delta H(\alpha,\beta,t)}{\partial q}\left.\frac{\partial q}{\partial\alpha}\right|_0 \tag{3.4}$$

it can be easily shown that:

$$\frac{\partial q}{\partial\alpha} \;=\; \frac{q}{2\alpha_0} \tag{3.5}$$

and $\alpha_0 = kA_0^2/2f_0$ where $A_0$ is the oscillation amplitude, $k$ is the spring constant, and $f_0$ is the resonance frequency of the oscillator. In the simplest experiment where a time-varying voltage is applied between a conducting tip and sample, $C$ has only an explicit $q$ dependence and $V$ only an explicit $t$ dependence:

$$\left.\frac{\partial\Delta H(\alpha,\beta,t)}{\partial\alpha}\right|_0 \;=\; \frac{\partial}{\partial q}\left[\frac{1}{2}C(q)V(t)^2\right]\Bigg|_0 \frac{qf_0}{kA_0^2} \tag{3.6}$$

However, $C$ does have an implicit time dependence because the position $q$ is not constant.

The capacitance, $C(q)$, between a conducting sphere and conducting plane can be

approximated by [39]:

$$C \approx 4\pi\epsilon_0 R\left[1+\frac{1}{2}\log\left(1+\frac{R}{q'}\right)\right] \tag{3.7}$$

where $R$ is the radius of the sphere and $q'$ is the sphere-plane (tip-sample) separation, which changes as the (tip) position, $q$, oscillates. In other words: $q' = A_0 + d + A_0\sin(\omega_0 t + \phi_0)$, where $\phi_0$ is the initial cantilever phase, $\omega_0$ is the free resonance frequency, $A_0$ is the amplitude, and $d$ is the closest tip-sample separation of the oscillating cantilever. Assuming this is an acceptable approximation for an AFM tip and conducting sample, the average frequency shift can be written:

$$\langle\Delta f\rangle = \langle\dot{\beta}\rangle = \frac{2\pi\epsilon_0(R/A_0)^2}{k}\frac{1}{1/f_0}\int_0^{1/f_0}\frac{V(t)^2}{q'+R}dt \tag{3.8}$$

with the integral taken over one cycle ($1/f_0$). Thus far we have only made an assumption regarding the functional form of the tip-sample capacitance. This relation (Equation 3.8) is thus valid for arbitrary oscillation amplitudes and timescales as long as the tip-sample interaction remains a small perturbation to the overall mechanical energy of the cantilever oscillation. This condition is fulfilled for a periodic voltage pulse with its frequency, $f_V$, away from any of the cantilever's mechanical resonances ($f_V < f_{i+1}$ and $f_V > f_i$ where $f_i$ is the $i$th mechanical eigenfrequency of the cantilever). This is due to the large quality factor enhancement present on resonance, which would lead to a significant contribution to the total mechanical energy from even a small voltage (and thus field) applied near resonance, invalidating the perturbation approach to derive Equation 3.8.

### 3.4.3 Validation Measurement

To demonstrate the time resolution of this technique a validation measurement was performed using a cantilever with a low resonance frequency (16.7kHz) and a conducting tip over a gold sample. The tip was retracted a short distance (∼20nm) with the z-feedback turned off and a train of exponential voltage pulses was applied, resulting in a change in the average frequency shift as a function of the width of the voltage pulse ($T$), illustrated in Figure 3.3(a). The frequency shift was averaged over several seconds for each value of $T$, and $T$ was then stepped as per the values in Figure 3.3(b). This full measurement was repeated 20 times with the z-feedback turned on and then back off between each measurement to minimize drift. Each pulse had the form $V(t) = V_0 + \Delta V\left(1 - e^{-t/\tau}\right)$ during the pulse-on period and $V(t) = V_0$ during the pulse-off period with a duty cycle of 20%. To fit the data, the integral in Equation 3.8 was performed piecewise over the corresponding on and off time periods for one full cantilever oscillation: $(0 \to T/5,\, T/5 \to T)$, $(T \to 6T/5,\, 6T/5 \to 2T)$, ... , $(..., (5N-4)T/5 \to NT)$, where $NT$ $1/f_0$ (note that $NT \neq 1/f_0$ because the pulse width can not be an integer multiple of the oscillation period as discussed above). This integral has no closed form solution and therefore must be computed numerically in order to fit the data. Since the phase between the applied pulses and the cantilever's oscillation is arbitrary, the integral must be computed for many oscillation cycles (starting with an arbitrary phase) and then averaged to minimize the effect of the initial relative phase.

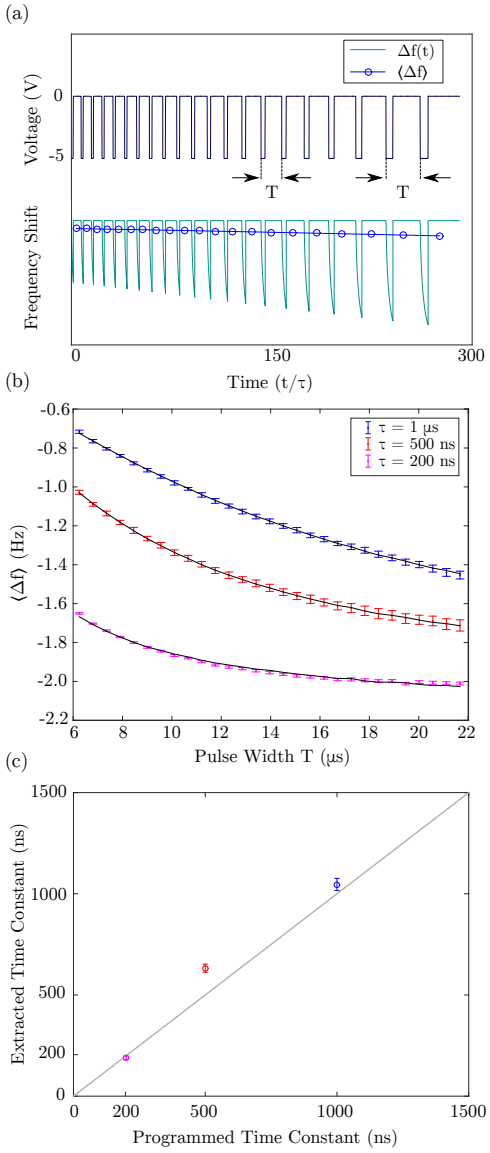


Figure 3.3: (a) Schematic illustration of the voltage-pulse averaging EFM technique: top shows the applied voltage pulses with different pulse width ($T$), while the bottom shows the (simulated) instantaneous ($\Delta f$) and average ($\langle \Delta f \rangle$) frequency shift due to an exponentially varying sample response. (b) Measured average frequency shift response vs. pulse width ($T$) for exponential voltage pulses with 1 $\mu$s (blue), 500 ns (red) and 200 ns (purple) time constants ($\tau$), cantilever $f_0 = 16.7$ kHz, 2 s averaging per measurement, 20 measurements per point. Errorbars are the standard deviation of 20 measurements, and the black lines show fits to Equation 3.8. (c) Extracted time constant ($\tau$), vs programmed time constant for the three measurements in (b); the solid gray line has a slope of unity to illustrate where points would lie for a perfect 1:1 relationship.
Measured values: $\tau = 1.05 \pm 0.03$ $\mu$s, $\tau = 633 \pm 20$ ns, $\tau = 192 \pm 3$ ns. Note that a decay time of 190 ns is ~300 times faster than the cantilever oscillation period.

The results are shown in Figure 3.3 along with the fits to Equation 3.8 where we set: $V(t) = A + B\mathrm{e}^{-t/\tau}$, giving 3 fit parameters: $A$, $B$, and the time constant $\tau$. The effect of the finite number of oscillation cycles appears in the fitted curves (black lines in Figure 3.3) as small deviations from a perfectly smooth function. This can be minimized by integrating over more cycles at the expense of increased computation time, which can be significant and has a negligible effect on the extracted fit parameters. The extracted time constants are plotted versus the programmed time constants in Figure 3.3(c).

Extending this technique to ionic transport systems requires only the insertion of an explicit time dependence of the capacitance $C(t)$ in place of the time dependent voltage in Equation 3.8. The capacitance follows the time dependence of the system after a bias is applied, which is typically a stretched exponential as in Equation 3.1. Although this is in principle feasible, the main challenge is to perform the fitting. We attempted to fit the data in Figure 3.3 to a stretched exponential with an additional parameter, $\beta$, which should result in an extracted value of $\beta = 1$ since this is a 'pure' exponential decay. The fitting was very problematic due to the dependence of the fit results on the chosen initial conditions. This is a general challenge when using functions with numerous fit parameters, in accordance with the famous quote about fitting an elephant by John Von Neumann [40].

### 3.4.4 Assumptions and Limitations

As shown by this validation measurement, this technique can be used to measure transport processes occuring faster than the period of the cantilever. Fundamentally the time resolution should only be limited by the minimum electrical pulse width that can be reliably applied to the sample (which is likely much larger than the theoretical limit [18]).

The only assumption used that may not be true for all cases is the functional form of the tip-sample capacitance (Equation 3.7). To test the accuracy of this assumption we investigated both a conducting sample and a thick dielectric sample (200$\mu$m thick sapphire, $\epsilon_r = 11.3$) by measuring the frequency shift vs. distance curve with a constant applied bias. The force was then extracted from the frequency shift using the Sader-Jarvis method [41] while taking care to ensure that the inversion procedure is mathematically well-posed for this particular experiment [42, 43].

The results are shown in Figure 3.4 where the black lines are fits to the approximate force between a conducting sphere held at a constant potential and a conducting plane:

$$F \approx \widetilde{F}\left[\frac{1}{(z/\widetilde{R}) + (z/\widetilde{R})^2}\right] \tag{3.9}$$

where $\widetilde{F}$ and $\widetilde{R}$ are fit parameters. Theoretically, $\widetilde{F} = 4\epsilon V^2$, where $\epsilon$ is the permittivity and $V$ is the applied voltage, and $\widetilde{R}$ is the effective tip radius. The oscillation amplitude for both experiments was 6 nm, thus the $x$-axis is the average tip-sample separation and the zero point was chosen as the point when the oscillation stopped due to contact with the sample. The resulting values for $\widetilde{F}$ were 0.6 nN for gold and 38.5 nN for sapphire and the effective tip radii obtained were $\widetilde{R} = 4.3$ nm and 0.23 nm for gold and sapphire, respectively. The $\widetilde{F}$ obtained for gold is very close to the theoretical value of 0.53 nN, but the value for sapphire is off by approximately a factor of 5, while the tip radii are significantly smaller than the true tip radius ($\approx 30$ nm). These results are not surprising as there are many potential sources of error that can affect the absolute value of the force including the cantilever spring constant calibration, background forces from the conical probe and the cantilever itself, and uncertainty in the zero-point for both the tip-sample separation and the force itself, which are typically chosen arbitrarily [44–49]. Note that this experiment aims only to demonstrate the validity of the functional form

of the relationship and not as a quantitative measurement of these parameters. Better approximations than the simple sphere-plane one used here have been developed, but would introduce significant challenges in computing the integral in Equation 3.8. Using this simple approximation for both the gold and sapphire substrates, the residuals are normally distributed to within experimental uncertainty (i.e. the $\chi^2$ goodness of fit test performed on the residuals does not reject the null hypothesis to 0.05 significance [50]). This demonstrates that the functional form of this approximation is valid with this particular probe type on samples of two extremes (a smooth conductor and a thick dielectric material), however it is not necessarily valid in all cases and should therefore be verified via spectroscopy measurements such as this on a case-by-case basis.

Sapphire was chosen for its high dielectric constant ($\epsilon_r > 10$), which is similar to those found in many solid ionic conductors such as $LiFePO_4$ and $LiCoO_2$, and for its low electronic conductivity and lack of mobile ions. This experiment is therefore a reliable validation of the z-dependence of the tip-sample capacitance expected for actual ionic transport measurements on relevant samples.

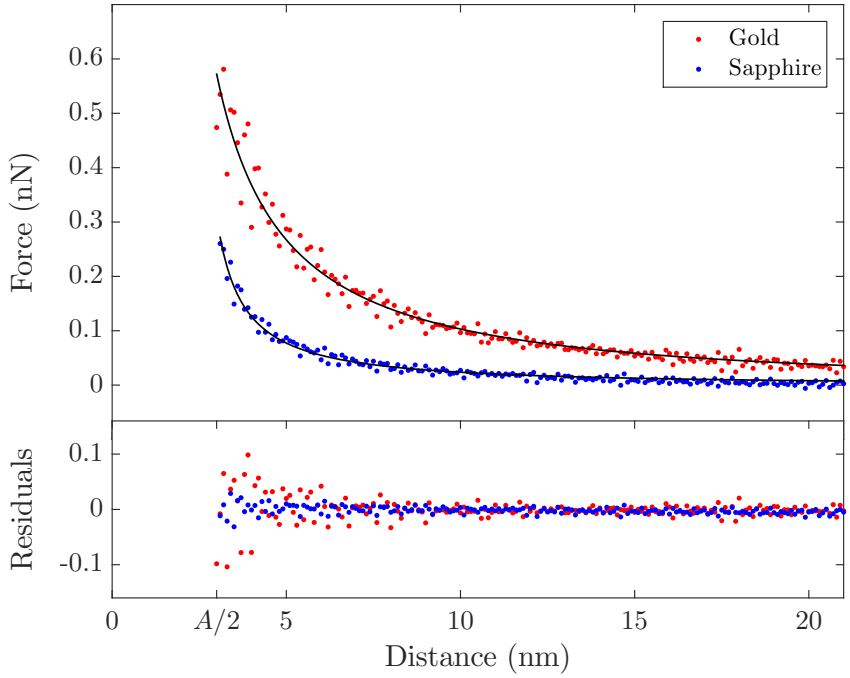


Figure 3.4: Measured tip-sample force vs. distance for a gold-coated tip over a grounded gold substrate (red) and a grounded 200$\mu$m thick sapphire substrate (blue) with 4V applied to the tip. Cantilever parameters: $f_0 = 295.621$ kHz, $k = 27$N/m, $A = 6$nm (Mikromasch NSC15/CR-AU).

## 3.5 Fast free time-resolved EFM

### 3.5.1 Motivation

It is clear that there exist challenges in using time-averaged AFM signals to extract fast sample dynamics, namely a priori knowledge or assumptions of the specific temporal functional form of the dynamics. Some techniques have sought to avoid this by directly capturing the deflection signal using high speed data acquisition systems and performing offline analysis to reconstruct the sample response. One such technique is fast free time-resolved electrostatic force microscopy (FF-trEFM), first proposed by Giridharagopal et. al [22]. FF-trEFM captures the full dynamics of an oscillating cantilever when an interaction force between the tip and sample is turned on. An overview of this technique is shown in Figure 3.5 (reproduced from [51]).

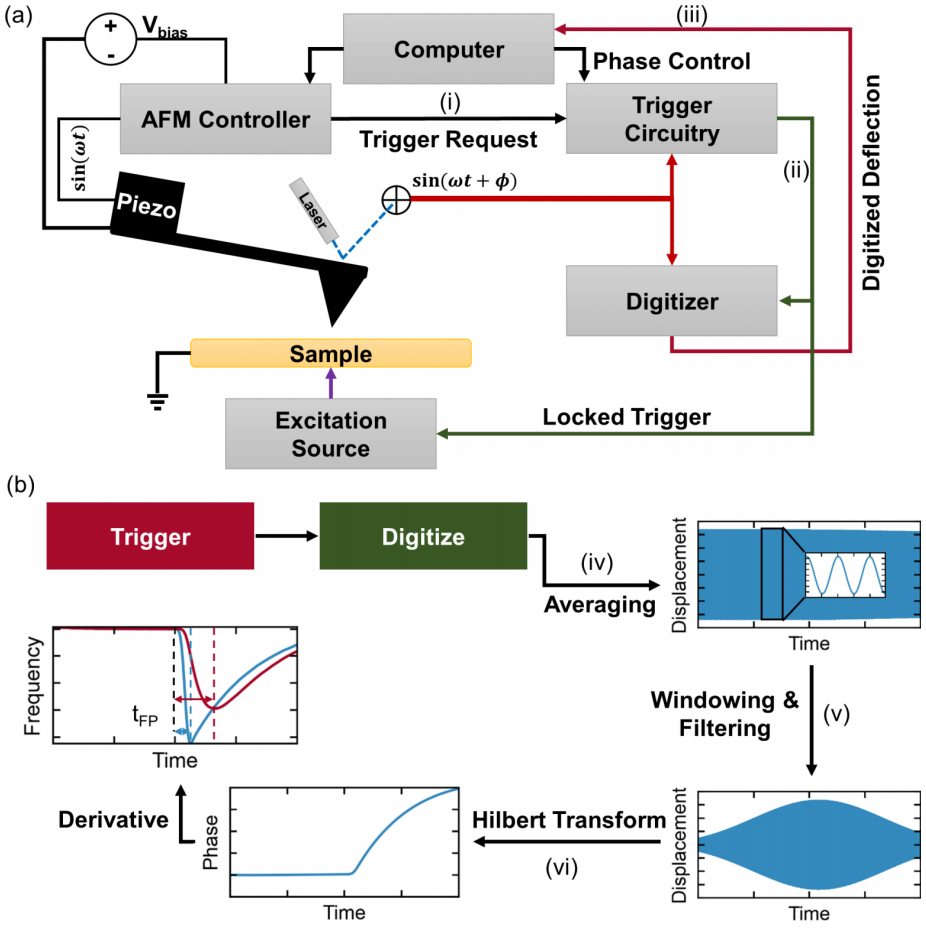


Figure 3.5: "(a) Schematic of the experimental setup: (i) Computer requests a trigger at a defined phase of the oscillation, (ii) trigger circuitry triggers the digitizer and the excitation source accordingly, and (iii) the digitizer transfers the acquired signals to computer. (b) Flow diagram of the data analysis procedure after the acquisition: (iv) signals are averaged together, (v) windowed and filtered, and (vi) demodulated via Hilbert transform to find the instantaneous frequency of the cantilever (instantaneous frequency curves for excitations with time constants of 25 ns and 100 $\mu$s are shown)." Reproduced from [51] with permission.

### 3.5.2 Description and Implementation

To implement FF-trEFM requires the addition of a high speed data acquisition system to a standard AFM, which is not overly expensive or onerous. Acquiring the raw deflection signal in the time-domain precludes the necessity for expensive detection electronics which are commonly used to acquire and demodulate the cantilever's oscillation. The only limitation on standard AFM systems are the photodetectors, which typically have bandwidths of 1-2 MHz, although faster photodiodes are available. The raw signal can then be filtered and postprocessed using a Hilbert transform to extract the analytical signal and what is known as the 'instantaneous frequency' (the time derivative of the instantaneous phase). Examining the extracted instantaneous frequency after applying a voltage with an exponential rise time $\tau$ (shown in Figure 3.5B for simulated data), it is clear that the response shows observable differences as a function of $\tau$. Since the cantilever is continuously driven throughout the experiment, the instantaneous frequency shows a fast transient response to the applied pulse, followed by a slow relaxation towards a new steady-state value. This leads to a clear initial peak in the frequency shift, which is defined as the 'time to first frequency shift peak' ($t_{\mathrm{FP}}$) by Giridharagopal et. al [22]. The authors demonstrated that simulated results (both numerical simulations of a damped-driven harmonic oscillator and finite element simulations) and their experimental results show excellent agreement given the same parameters and subject to the same postprocessing (windowing, filtering, and analytical signal extraction).

It is instructive to note that the extracted instantaneous frequency contains a time-delay introduced by the bandpass filter used in the processing to smooth the response, which cannot be completely corrected for. This leads to attenuation of high frequency components, especially for decay times faster than the oscillation period. Because of this attenuation, the extracted signal is a representation of the true 'instantaneous frequency',

leading to difficulty in determining the full functional form of the time-dependent tip-sample interaction.

### 3.5.3 Application to Ionic Transport Measurements

To accurately quantify ionic transport requires the capability to fully resolve the functional form of a stretched exponential response to extract the two main parameters of interest, $\tau$ and $\beta$. To test the suitability of FF-trEFM for these measurements, we performed numerical simulations (of a damped driven harmonic oscillator, see Supporting Information File B.1, Appendix B, for MATLAB code) similar to those performed by Karatay et al. [51], using instead a resonance frequency varying in time as a stretched exponential and a stretched exponential electrostatic force term:

$$\omega_0(t \geq 0) \;=\; \omega_0(t=0) + \Delta\omega(1 - \mathrm{e}^{-(t/\tau)^{\beta}}) \tag{3.10}$$

$$F_e(t) = F_{e0}(1 - \mathrm{e}^{-(t/\tau)^{\beta}}). \tag{3.11}$$

The parameters used were $\omega_0 = 2\pi\times277$ kHz, $\Delta\omega = 2\pi\times277$ Hz, and $F_{e0} = 3$ nN, similar to those used in Ref. [22]. The results after windowing, filtering, and performing the Hilbert transform are shown in Figure 3.6. The colours denote different time constants and the $\beta$ values are shown by different linestyles. For slower time constants ($\tau \geq 10$ $\mu$s) the different values of $\beta$ are visually distinct; however, at much smaller timescales these distinctions are no longer visible, making ionic transport measurements using FF-trEFM challenging and possibly no more advantageous than direct time-domain EFM.

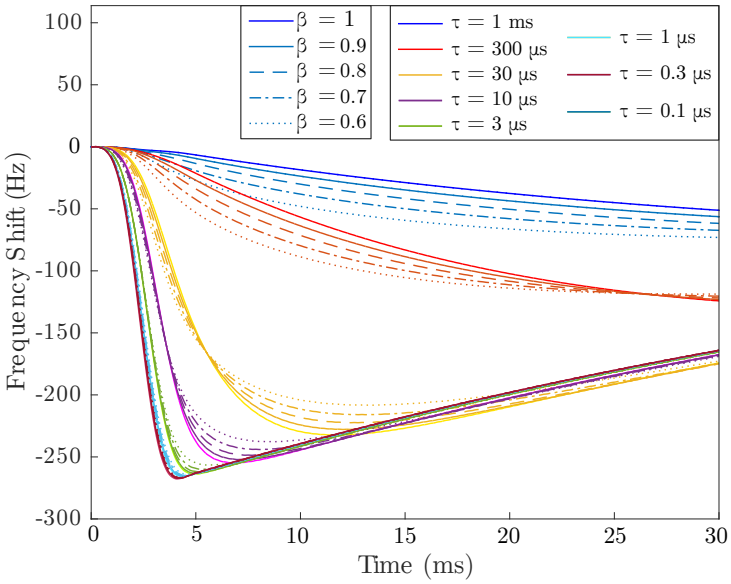


Figure 3.6: Extracted FF-trEFM signals from numerical simulations of tip-sample interactions with a stretched-exponential time response (Equation 3.1) with various relaxation time constants, $\tau$, and stretching factors, $\beta$.

### 3.5.4 Demonstration of Spatial Resolution

In more recent work by Karatay et al., they analyzed how a variety of factors including noise and the phase difference between the cantilever oscillation and the applied pulses affect the achievable time resolution [51]. They presented guidelines for implementation of their technique, in particular the use of photothermal excitation to reduce other sources of mechanical noise. To study the relationship between the system dynamics and the measured $t_{\mathrm{FP}}$ response they mapped $t_{\mathrm{FP}}$ as a function of true exponential time constant $\tau$ to generate a calibration curve (Figure 3.7(a)). They observed statistically significant differences in the measured signal in differences in $\tau$ down to 10 ns, which they designated as the minium attainable time resolution. The authors then utilized $t_{\mathrm{FP}}$ to study differences in local charging times of an organic photovoltaic thin film (MDMO-PPV:PCBM), shown in Figure 3.7, and demonstrated the ability of the technique to spatially resolve heterogeneities. Due to the difficulty in quantitatively extracting $\tau$ from the measured $\tau_{\mathrm{FP}}$, spatially resolved measurements are limited to relative charging rates presented as spatial mapping of $\tau_{\mathrm{FP}}$. These results can still provide useful insight into sample dynamics (in this case the quantum efficiency of the photovoltaic material) even though direct quantitative measurements of decay time constants may not always be possible.

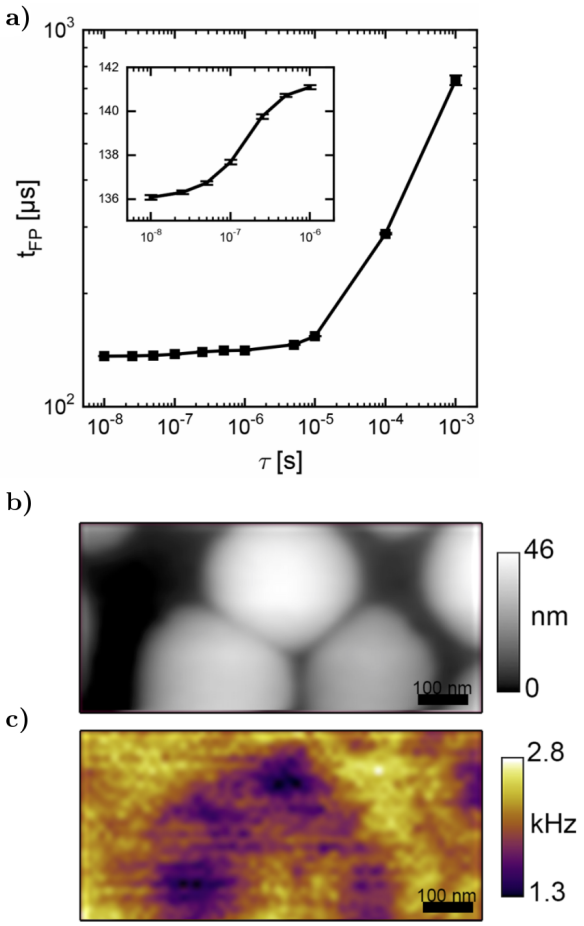


Figure 3.7: "(a) Calibration curve for a range of characteristic times of exponential decay ($\tau$) (inset shows a zoom-in for shorter times)." "(b) Topography and (c) inverse $\tau_{\mathrm{FP}}$ ($\tau_{\mathrm{FP}}^{-1}$) images of a 1:4 ratio MDMO-PPV:PCBM thin film photovoltaic device cast from toluene. Excitation wavelength is 488 nm and intensity at the tip is $\sim$290 W/cm$^2$. Data are acquired at 10 nm lift height, 10 V bias between the cantilever and the sample, with 60 averages per pixel." Adapted from [51] with permission.

## 3.6 Phase-kick EFM

### 3.6.1 Background and Implementation

Another technique recently developed by Dwyer et. al, referred to as “phase-kick" EFM (pk-EFM), uses an indirect measurement of the cumulative change of a cantilever parameter (phase or amplitude) in order to reconstruct a time-varying signal [23]. One implementation of pk-EFM utilizes a carefully timed voltage pulse applied between the tip and sample that controls the tip-sample coupling while a light pulse is also applied, as illustrated in Figure 3.8 (reproduced from [23]). Initially, the cantilever is driven on resonance at a steady-state amplitude and a voltage is applied. The voltage engages the tip-sample coupling and leads to an initial frequency shift, which can be seen at $t$ = -50 ms in Figure 3.8F. A short time later the drive is turned off so that the cantilever is freely oscillating; practically, this removes the drive signal as a source of noise in the experiment. At $t = 0$ a light pulse is then applied and the capacitance varies temporally as the sample charges due to the photoexcitation. By then abruptly turning off the tip-sample coupling (by setting the voltage back to 0) the total photocapacitance change measured by the cantilever can be controlled. The applied voltage therefore acts as a gate that controls the cumulative sample response that is captured in the cumulative change in the cantilever oscillation. The total phase shift $\Delta\phi$ from the time the light pulse is applied ($t = 0$) to when the voltage is returned to 0 ($t = t_p$) is then proportional to the integrated photocapacitance since the voltage is held constant over this time:

$$\Delta\phi \;=\; -\frac{f_0 V^2}{4k_0}\int_0^{t_p} C_t''(t)\,dt \tag{3.12}$$

where $C_t''$ is the is the second derivative of the tip-sample capacitance with respect to vertical separation, $f_0$ is the resonance frequency, and $k_0$ is the spring constant. This

result is derived from the relationship between the frequency shift and the capacitive force between the tip and sample:

$$\delta f(t) \;=\; -\frac{f_0}{4k_0} C_t''(t) V^2 \tag{3.13}$$

which is a valid approximation in the limiting case of small oscillation amplitudes [37]. More specifically, this approximation is only valid if the force gradient is constant over one full oscillation of the tip [52]. This can be acheived under typical experimental conditions (1-5 nm oscillation amplitude) by simply performing the measurement with a larger tip-sample separation, but this comes at the cost of degraded spatial resolution. Achieving smaller oscillation amplitudes ($\ll$ 1 nm) is possible using more sensitive detection methods (interferometry, for example [53]) and cleaner excitation schemes such as photothermal excitation [54]. Using higher stiffness probes, however, is not expected to be advantageous due to the inverse relationship between the measured phase shift and cantilever spring constant.

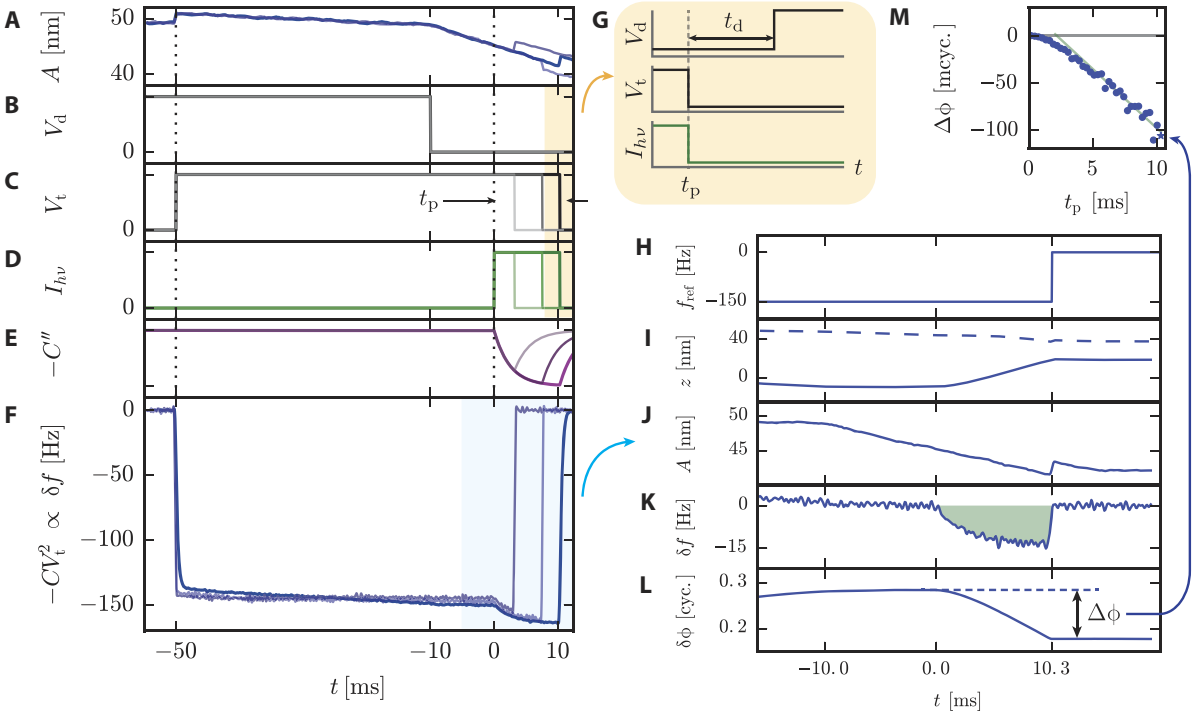


Figure 3.8: "For three representative pulse times, we plot (A) cantilever amplitude; (B) cantilever drive voltage, turned off at $t$ = -10 ms; (C) tip voltage, with the pulse time $t_p$ indicated; (D) sample illumination intensity, turned on at $t = 0$; (E)sample capacitance; and (F) cantilever frequency shift. (G) Timing of applied voltages and light pulses. The voltage and light turn off simultaneously at $t = t_p$. After a delay $t_d$ (typically 5 to 15 ms), the cantilever drive voltage is turned back on. Next, we illustrate how the phase shift $\Delta\phi$ is calculated using the $t_p$ = 10.3 ms data. We process the cantilever displacement data using a software lock-in amplifier. (H) The software lock-in amplifier reference frequency changes at $t = t_p$. The software lock-in amplifier outputs (I) the in-phase (solid) and out-of-phase (dashed) components of the cantilever displacement; (J) cantilever amplitude; (K) frequency shift; and (L)phase shift. The total phaseshift $\Delta\phi$ is equal to the highlighted area under the cantilever frequency shift curve. (M) The voltage- and light-induced phase shift $\Delta\phi$ is measured as a function of the pulse time $t_p$. We show only every other data point for clarity. The $t_p$ = 10.3ms data point is denoted with a star. Experimental parameters: PFB:F8BT on indium tin oxide (ITO) film, h = 250 nm, $V_t$ = 10V, $I_{h\nu}$ = 0.3 kW m$^{-2}$, delay time between pulses = 1.5 s." The cantilever used had a resonance frequency of 62 kHz. Reproduced from [23] with permission.

### 3.6.2 Validation Measurement

To demonstrate the sub-cycle time resolution of this technique, Dwyer et al. used the Magnus expansion in order to solve the system of linear differential equations describing the cantilever motion [23]. Modelling the photocapacitance as a single exponential with a risetime of $\tau$, $C_t''(t) = C_t''(0) + \Delta C_{h\nu}''(1 - e^{-t/\tau})$, resulted in two expressions relating the cumulative amplitude ($\Delta A$) and phase shifts ($\Delta\phi$) to the time constant:

$$\Delta A \approxeq \delta x h\nu \frac{\omega_0}{1+\tau^2\omega_0^2}\left[t_p - \tau + \tau e^{-t_p/\tau}\right]\sin\phi_p \tag{3.14}$$

$$\Delta\phi \approxeq \frac{\delta x h\nu}{A_0}\frac{\omega_0}{1+\tau^2\omega_0^2}\left[t_p - \tau + \tau e^{-t_p/\tau}\right]\cos\phi_p \tag{3.15}$$

where $\delta x_{h\nu} = V^2\Delta C_{h\nu}'/(2k_0)$ ($\delta x_{h\nu}$ is the DC deflection due to the photocapacitive force). This result is valid for very short times after the voltage is abruptly returned to 0. It is especially interesting as it relates the change in amplitude and phase with the phase of the cantilever when the voltage is turned off, $\phi_p = \theta(t = t_p)$. By tuning $t_p$, a phase shift, an amplitude change, or a combination of both can be induced. The technique is fully illustrated in Figure 3.9 where the amplitude data in E ($\Delta A$) was obtained by voltage pulses alone. The voltage pulses resulted in charging/discharging of the sample (PFB:F8BT on ITO), which was also modelled as a single exponential in time: $V_t(t) = V(1 - e^{-t/\tau_c})$. This allowed for the amplitude to be written as a function of $t_p$ and $\tau_c$ where it again displayed a sinusoidal dependence on $\phi_p$. Note that $t_p$ in Figure 3.9 refers to the width of the voltage pulse whereas $t_p$ used in the derivation was the time at which the voltage was returned to zero. Relabelling the width of the voltage pulses as $t_p'$ this yields: $t_p = t_p' + t_d$; in other words the $t_p$ in Equations 3.14 and 3.15 can be tuned by changing the delay time $t_d$. This is shown in Figure 3.9E where the sinusoidal behaviour of $\Delta A$ as a function of $t_d$ is clear. Figure 3.9F shows the maximum amplitude

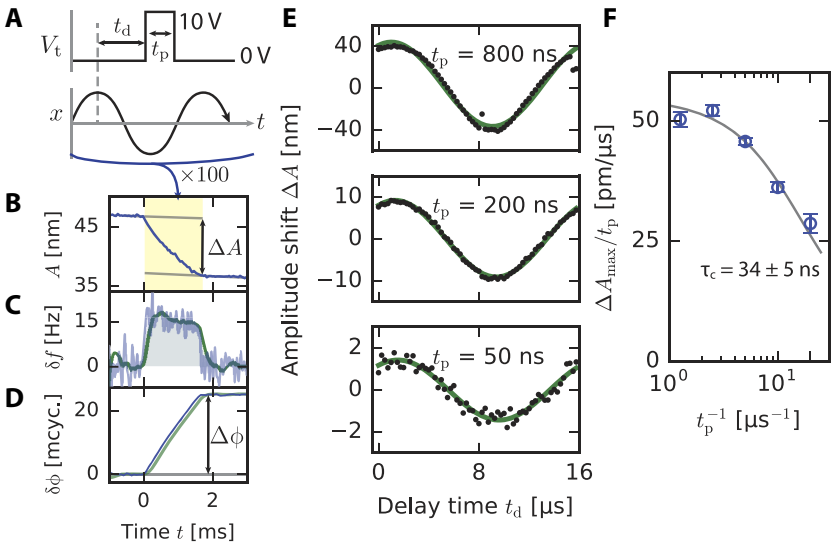


Figure 3.9: "Experiments and simulations demonstrating subcycle time resolution in pk-EFM. (A) Subcycle voltage-pulse control experiment (PFB:F8BT on ITO, h = 250 nm). A voltage pulse of length $t_p$ is applied to the cantilever tip (top) at a delay of $t_d$ relative to the cantilever oscillation (middle) for 100 consecutive cantilever oscillations. (B) The pulses shift the cantilever amplitude by $\Delta A$.(C) Measured frequency shift and (D) phase shift, demodulated with a 3-dB bandwidth of 4.8 kHz (blue) and 1.5 kHz (green). (E) The amplitude shift $\Delta A$ versus delay time $t_d$ for three representative pulse lengths. (F) The normalized response $\Delta A_{max}/t_p$ obtained by fitting data in (E) shows the cantilever wiring attenuating the response at short pulse times. The gray line is a fit to a single-exponential cantilever charging transient." Adapted from [23] with permission.

change $\Delta A_{max}$ as a function of the inverse pulse width $1/t'_p$. An exponentially decreasing amplitude change at smaller pulse widths is clearly visible, which the authors explain as due to the charge being unable to get in and out of the sample on these fast timescales. The extracted time constant for the charging time, $\tau_c$, was 34 ± 5 ns.

### 3.6.3 Application to Ionic Transport Measurements

From this voltage-pulse measurement it is clear that this technique can easily be extended to measure ionic transport. In fact, it may even be best suited to this application as it requires only a precisely timed voltage pulse instead of phase-locked voltage and light pulses. This technique operates in much the same way as the voltage-pulse averaging method previously described: a parameter of the cantilever's oscillation (be it phase, frequency shift, or amplitude) is averaged over a long time period while a coherent (i.e. phase locked with respect to cantilever oscillation) repeating signal is applied over a much smaller time period that induces a change in the measured parameter. By changing the length of time that the 'fast' signal is allowed to interact with the cantilever it can then be reconstructed by relating the slowly varying parameter to the fast dynamics. Although similar to pump-probe style measurements, these techniques are unique in that they operate by changing the cumulative interaction time between the probe and the sample instead of simply capturing 'snapshots' of the evolution of the sample dynamics as a function of time. This allows for sample dynamics that are driven only while the tip-sample coupling is engaged to be measured, such as ionic transport, for example. Directly applying this technique to measure ionic transport, however, would require the addition of a stretching factor, $\beta$, into the exponential as previously discussed. The main complication in this case is performing the time-integral over the capacitive gradient, which was assumed to be a simple exponential in Equations 3.14 and 3.15. The integral will not have a closed-form solution, which would require either a series expansion approximation or a numerical approximation in order to extract useful information from the data. This will likely result in the same challenge as we encountered with the voltage-pulse averaging technique where the least-squares fitting has many local minima for the fit parameters resulting in a strong dependence of the fit results on the initial conditions. Nonetheless, this technique is promising in terms of achieving better time-resolution in EFM-based

measurements.

## 3.7 Intermodulation Spectroscopy

### 3.7.1 Background and Implementation

Significant progress has clearly been made in measuring electrostatic force microscopy signals in the time-domain. The main challenges of the techniques discussed thus far have been the detection methods (specificially, bandwidth limitations) and various assumptions and approximations that have been made, which limit the useful parameter space of some experiments. Looking instead in the frequency domain, one very recent method of extracting fast sample dynamics appears to be a promising alternative to many of these challenges. Intermodulation spectroscopy, developed by Borgani and Haviland [20], utilizes the spectral response of a cantilever near resonance due to an applied pulse train (optical or electrical) in order to probe sample dynamics. This technique exploits the non-linear tip-sample interaction due to the applied pulse train that results in a spectrum of peaks at various sum and difference frequencies, illustrated in Figure 3.10. Each of these frequency components (referred to as intermodulation products, or IMPs) contains information about the interaction, which can be extracted by looking at the Fourier series expansion of the tip-sample interaction. Since the interaction is purely capacitive, the force is given by: $F = \frac{1}{2}\frac{\partial C}{\partial z}V^2$, which contains two separate variables each with their own periodicity: the capacitive gradient $\frac{\partial C}{\partial z}$, and the voltage $V$. Since $V$ is controlled by the applied excitation, it is periodic in $\omega_E$, the repetition rate of the applied pulses. The Fourier series for $V^2(t)$ is therefore given by:

$$V^2(t) \;=\; \sum_{j=-\infty}^{+\infty} v_j \mathrm{e}^{\mathrm{i}(j\omega_E t+\theta_j)}. \tag{3.16}$$

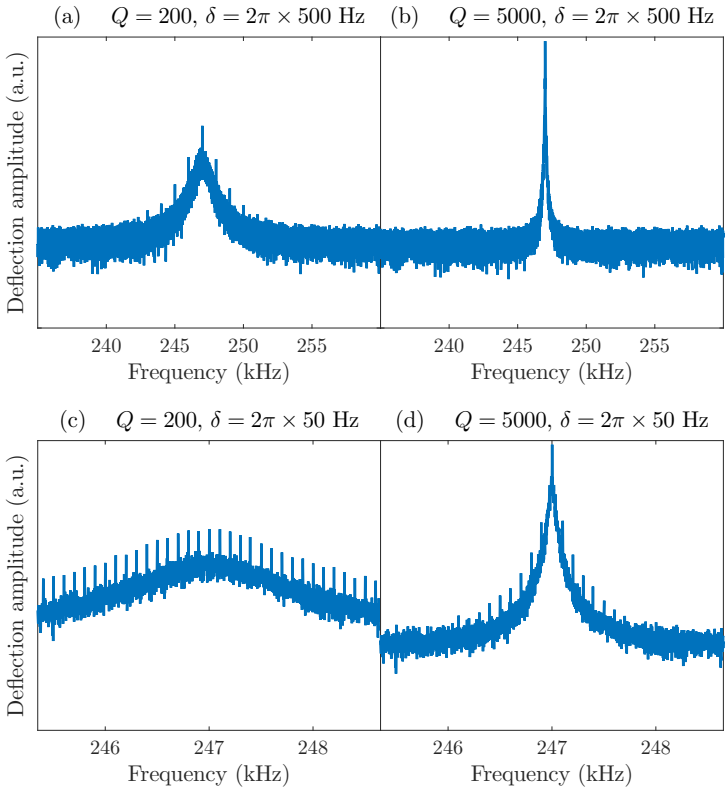


Figure 3.10: Synthetic data of cantilever deflection spectrum around the fundamental resonance frequency, $\omega_0 = 2\pi\times$ 247 kHz, with: (a) $\delta = 2\pi\times$ 500 Hz and a quality factor typical for ambient measurements, $Q = 200$; (b) $\delta = 2\pi\times$ 500Hz and $Q = 5000$, typical of vacuum measurements; (c) $\delta = 2\pi\times$ 50 Hz and $Q = 200$; and (d) $\delta = 2\pi\times$ 50 Hz and $Q = 5000$.

In the case where the sample capacitance remains constant (in a conducting sample, for example), the capacitance gradient has the same periodicity as the cantilever oscillation since the cantilever sweeps through the gradient as it oscillates. The Fourier series expansion for $\frac{1}{2}\frac{\partial C}{\partial z}[z(t)]$ can then be written:

$$\frac{1}{2}\frac{\partial C}{\partial z}[z(t)] \;=\; \sum_{k=-\infty}^{+\infty} c_k \mathrm{e}^{\mathrm{i}(k\omega_D t+\phi_k)}. \tag{3.17}$$

The authors proposed three distinct excitation schemes based on the frequency of the applied pulses, $\omega_E$, relative to the mechanical drive frequency $\omega_D$: resonant excitation, where $\omega_E = \omega_D + \delta$, with $\delta \ll \omega_0$; sub-resonant excitation, where $\omega_E = \delta \ll \omega_D$; and super-resonant excitation, where $\omega_E = 2\omega_D + \delta$. For each excitation scheme they showed

the Fourier coefficients for the first 6 IMPs, which have the form: $\hat{F}_{\pm n} = c_k v_j e^{i(\phi_k \pm \theta_j)}$. For resonant excitation, they determined that taking the ratio and product of certain pairs ($\hat{F}_{n+2}$ and $\hat{F}_{-n}$) yields quantities that depend only on the electrical response, which completely eliminates the dependence on the capacitance gradient. Thus, to extract information about the system using these quantities does not require any assumptions about the functional form of the capacitance gradient. The only (major, and possibly limiting) assumption is that the sample is metallic (see discussion below). The authors also derived similar ratios for both the sub-resonant and super-resonant schemes, allowing them to directly compare the time resolution and signal to noise ratio of each.

### 3.7.2 Validation Measurement

As a validation measurement, they applied electrical pulses with known exponential charging times between a conducting tip and sample and extracted the rise and fall time constants, $\tau_r$ and $\tau_f$, using an analytical model for $V^2(t)$. This allows for a high-fidelity reconstruction of the true signal using only a few Fourier coefficients. Using the resonant excitation scheme, they accurately extracted the time constants down to $\approx$ 20 ns, approaching the theoretical limit they derived for the technique. Their results are shown in Figure 3.11 for each of the three excitation schemes. Both the resonant and super-resonant schemes allowed signals more than an order of magnitude faster than the oscillation period of the cantilever to be extracted.

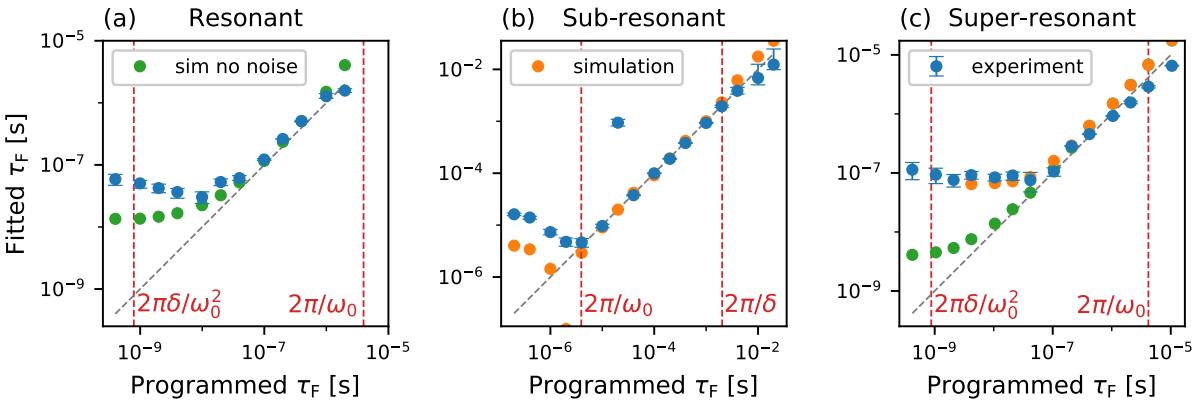


Figure 3.11: "Results from simulations and from the experimental validation for the proposed excitation schemes: (a) resonant, (b) sub-resonant and (c) super-resonant. The cantilever has a resonance frequency of about $2\pi\times250$ kHz, a value of $\delta = 2\pi\times500$ Hz is used in the sub-resonant scheme and $\delta = 2\pi\times50$ Hz in the resonant and super-resonant schemes. The fittted values $\tau_F$ are plotted versus the value programmed in the simulation and in the MLA. The gray dashed lines have slope unity and indicate where a perfect data point would be. For the experimental data, a series of 256 measurements is performed at each value of programmed $\tau_F$: the blue dots indicate the median of the reconstructed values, and the error bars indicate the inter-quartile range. The vertical red dashed lines mark the time resolution calculated in Sec. IV." of Ref. [20]. "(a) in the resonant scheme, both simulations without noise (green dots) and experiments fail to reach the predicted time-resolution, due to the violation of Eq. (7). (b) in the sub-resonant scheme, simulations with detector and force noise (orange dots) and experiments show the predicted time resolution. (c) in the super-resonant scheme, simulations without noise approach the predicted time resolution, while experiments are limited to about 50 ns. Simulations with detector and force noise reproduce the experimental data." Reproduced from [20] with permission.

They report that mapping of system dynamics can be done even at standard imaging speeds due to the simultaneous acquisition at multiple frequencies using a multi-frequency lock-in amplifier. This is a drastic improvement over many other time resolved EFM variations that require lengthy averaging times, which makes spatial mapping difficult and time consuming.

### 3.7.3 Challenges and Application to Ionic Transport Measurements

Thus far, measurements using this technique have only been performed in ambient conditions and on a conducting sample with known voltage pulses. One foreseeable challenge will be in performing measurements under vacuum conditions, which is typically beneficial due to the large increase in quality factor that leads to a greater force sensitivity. However, for intermodulation spectroscopy measurements, this will lead to a smaller frequency window in which quality factor enhancement will be available to boost the relative amplitudes of the IMPs. This is illustrated in Figure 3.10 where (a) shows synthetic data for a standard cantilever in ambient ($Q$=200) with several IMPs clearly visible above the noise. Figure 3.10(b) shows the exact same simulated experiment with a much higher quality factor (Q=5000), which is typical for vacuum applications. In both cases $\delta = 2\pi x500$ Hz. Reducing $\delta$ to 50 Hz, as was done for the resonant and super-resonant experiments, yields many more IMPs above the noise level as shown in Figure 3.10(c). Simultaneously demodulating several of these components allows for accurate reconstruction of the time-varying voltage. However, in the case of high $Q$, we see that many of the peaks are now well below the noise level due to the size of the resonance peak compared to the IMP spacing ($\delta$). The signal to noise ratio is significantly lower in this case, requiring a much smaller value of $\delta$ and, in turn, longer averaging times. Note that

since the time resolution is proportional to $\delta$ (Equations 15 and 16 in Ref. [20]), using a smaller $\delta$ actually results in better time resolution, at the expense of longer measurement times.

Another complication that may be encountered will be observed when performing measurements on samples with non-static capacitance gradients. For the analysis performed in this case the capacitance was assumed to have only the periodicity of the cantilever oscillation, $\omega_D$, which is, of course, valid because the sample is a conductor. This will not be the case when the capacitance gradient has an explicit time dependence, as with many photovoltaic and ionic conductors. In these samples, the tip-sample capacitance gradient will evolve with time after the application of the pulse (be it optical or electronic) and will therefore have a frequency component matching that of the applied pulses, $\omega_E$. This is due to sample dynamics such as photoexcitation or ionic transport [12, 23, 55]. This may make extracting the sample time response much more difficult if the capacitive Fourier coefficients cannot be eliminated by taking ratios of certain components. There may be methods of minimizing this effect, especially in the case of optical pulses for measuring time-resolved photocapacitance similar to the pk-EFM method discussed previously [23]. In this implementation, Dwyer et al. applied a large bias between the tip and sample to engage the coupling, having the fortunate side-effect of rendering the measurement insensitive to small variations in surface potential as the sample charges. This results in a response that is only sensitive to the time-varying capacitance, simplifying the analysis significantly. Similar techniques may be required to extract information from samples where large time-dependent changes in capacitance and surface potential are expected.

## 3.8 Conclusion

We have reviewed several established techniques that acheieve time-resolution using EFM and examined their assumptions, limitations, and potential applications. Direct time-domain EFM is the most straightforward to implement, but is limited to measuring on timescales much slower than the cantilever oscillation. The new technique we have demonstrated – voltage-pulse averaging EFM – allows for time resolution much faster than the cantilever oscillation period, but requires a priori knowledge of the time-evolution of the signal and the functional form of the tip-sample capacitance. FF-trEFM, which uses post-processing to extract the instantaneous frequency of the cantilever, allows for rapid data acquisition while scanning and high spatial resolution, but suffers from a nonlinear variation of the measured signal with the time constant of the sample response for fast responses. Phase-kick EFM provides a pathway to extract sample dynamics indirectly by observing cumulative changes in the cantilever oscillation, but relies on the assumption that the oscillation amplitude is small with regards to the capacitance gradient, which can be violated for large amplitudes and/or small tip-sample separations. Finally, we have looked in detail at intermodulation spectroscopy, which exploits the non-linear signal mixing of the cantilever oscillation and an applied pulse train by recording the various frequency components corresponding to specific Fourier coefficients. This technique may encounter difficulties in extracting information for measurements where the tip-sample capacitance also changes as a result of the applied pulse train.

Despite many of these assumptions and potential limitations, all of these techniques represent great strides in the advancement of time-resolution in EFM. With the need for measurements of faster and faster dynamics with higher spatial resolution, the role of time-resolved EFM as a key tool is more significant than ever.

## Supporting Information - Appendix B

Supporting Information contains

Supporting Information File 1:

File Name: sub_cycle_sim_beta.m

File Format: MATLAB

Title: MATLAB code to simulate FF-trEFM measurements with a stretched exponential response.

## Acknowledgements

We would like to thank Jake Precht, Rajiv Giridharagopal, and David S. Ginger for their help in simulating the FF-trEFM measurements. We would also like to thank Riccardo Borgani for discussions on Intermodulation Spectroscopy. We acknowledge financial support from the Natural Sciences and Engineering Research Council of Canada, and the Fonds de recherche du Quebec - Nature et Technologies.

## References

[1] M Nonnenmacher, MP o'Boyle, and H Kumar Wickramasinghe. "Kelvin probe force microscopy". In: *Applied Physics Letters* 58.25 (1991), pp. 2921–2923.

[2] P Güthner and K Dransfeld. "Local poling of ferroelectric polymers by scanning force microscopy". In: *Applied Physics Letters* 61.9 (1992), pp. 1137–1139.

[3] RJ Hamers and David G Cahill. "Ultrafast time resolution in scanned probe microscopies: Surface photovoltage on Si (111)–(7× 7)". In: *Journal of Vacuum Science & Technology B: Microelectronics and Nanometer Structures Processing, Measurement, and Phenomena* 9.2 (1991), pp. 514–518.

[4] Todd D Krauss and Louis E Brus. "Charge, polarizability, and photoionization of single semiconductor nanocrystals". In: *Physical Review Letters* 83.23 (1999), p. 4840.

[5] Liwei Chen et al. "Photoinduced interfacial charging and "explosion" of monolayer pentacene islands". In: *Nano Letters* 5.11 (2005), pp. 2241–2245.

[6] David C Coffey and David S Ginger. "Time-resolved electrostatic force microscopy of polymer solar cells". In: *Nature Materials* 5.9 (2006), pp. 735–740.

[7] A Schirmeisen et al. "Probing ion transport at the nanoscale: Time-domain electrostatic force spectroscopy on glassy electrolytes". In: *Applied Physics Letters* 85.11 (2004), pp. 2053–2055.

[8] Senli Guo et al. "Direct mapping of ion diffusion times on LiCoO2 surfaces with nanometer resolution". In: *Journal of the Electrochemical Society* 158.8 (2011), A982–A990.

[9] Obadiah G Reid et al. "Imaging local trap formation in conjugated polymer solar cells: a comparison of time-resolved electrostatic force microscopy and scanning Kelvin probe imaging". In: *The Journal of Physical Chemistry C* 114.48 (2010), pp. 20672–20677.

[10] Phillip A Cox et al. "Imaging charge transfer state excitations in polymer/fullerene solar cells with time-resolved electrostatic force microscopy". In: *The Journal of Physical Chemistry Letters* 6.15 (2015), pp. 2852–2858.

[11] Marin Alexe. "Local mapping of generation and recombination lifetime in BiFeO3 single crystals by scanning probe photoinduced transient spectroscopy". In: *Nano Letters* 12.5 (2012), pp. 2193–2198.

[12] Aaron Mascaro et al. "Measuring spatially resolved collective ionic transport on lithium battery cathodes using atomic force microscopy". In: *Nano Letters* (2017).

[13] Stephen Jesse et al. "Direct mapping of ionic transport in a Si anode on the nanoscale: time domain electrochemical strain spectroscopy study". In: *ACS Nano* 5.12 (2011), pp. 9682–9695.

[14] J Murawski et al. "Pump-probe Kelvin-probe force microscopy: Principle of operation and resolution limits". In: *Journal of Applied Physics* 118.15 (2015), p. 154302.

[15] Guozheng Shao et al. "Intensity-modulated scanning Kelvin probe microscopy for probing recombination in organic photovoltaics". In: *ACS nano* 8.10 (2014), pp. 10799–10807.

[16] Liam Collins et al. "Breaking the time barrier in Kelvin probe force microscopy: fast free force reconstruction using the G-Mode platform". In: *ACS Nano* 11.9 (2017), pp. 8717–8729.

[17] Pablo A Fernandez Garrillo et al. "Photo-Carrier Multi-Dynamical Imaging at the Nanometer Scale in Organic and Inorganic Solar Cells". In: *ACS Applied Materials & Interfaces* 8.45 (2016), pp. 31460–31468.

[18] Zeno Schumacher et al. "The limit of time resolution in frequency modulation atomic force microscopy by a pump-probe approach". In: *Applied Physics Letters* 110.5 (2017), p. 053111.

[19] Joseph L Garrett and Jeremy N Munday. "Fast, high-resolution surface potential measurements in air with heterodyne Kelvin probe force microscopy". In: *Nanotechnology* 27.24 (2016), p. 245705.

[20] Riccardo Borgani and David B Haviland. "Intermodulation spectroscopy as an alternative to pump-probe for the measurement of fast dynamics at the nanometer scale". In: *arXiv preprint arXiv:1809.08058* (2018).

[21] Sascha Sadewasser and Thilo Glatzel. *Kelvin Probe Force Microscopy: From Single Charge Detection to Device Characterization*. Vol. 65. Springer, 2018.

[22] Rajiv Giridharagopal et al. "Submicrosecond time resolution atomic force microscopy for probing nanoscale dynamics". In: *Nano Letters* 12.2 (2012), pp. 893–898.

[23] Ryan P Dwyer, Sarah R Nathan, and John A Marohn. "Microsecond photocapacitance transients observed using a charged microcantilever as a gated mechanical integrator". In: *Science Advances* 3.6 (2017), e1602951.

[24] TR Albrecht et al. "Frequency Modulation Detection using High-Q Cantilevers for Enhanced Force Microscope Sensitivity". In: *Journal of Applied Physics* 69.2 (1991), pp. 668–673.

[25] Ch Schönenberger and SF Alvarado. "Observation of single charge carriers by force microscopy". In: *Physical Review Letters* 65.25 (1990), p. 3162.

[26] Todd D Krauss, Stephen O'Brien, and Louis E Brus. "Charge and photoionization properties of single semiconductor nanocrystals". In: *The Journal of Physical Chemistry B* 105.9 (2001), pp. 1725–1733.

[27] R Bennewitz, M Reichling, and E Matthias. "Force microscopy of cleaved and electron-irradiated CaF2 (111) surfaces in ultra-high vacuum". In: *Surface Science* 387.1-3 (1997), pp. 69–77.

[28] Venceslav F Kroupa. *Phase lock loops and frequency synthesis*. John Wiley & Sons, 2003.

[29] "HF2LI lock-in amplifier". In: *Instruments, Zürich* Rev. 42300 (2017).

[30] KL Ngai and O Kanert. "Comparisons between the coupling model predictions, Monte Carlo simulations and some recent experimental data of conductivity relaxations in glassy ionics". In: *Solid State Ionics* 53 (1992), pp. 936–946.

[31] K Funke. "Jump relaxation in solid electrolytes". In: *Progress in Solid State Chemistry* 22.2 (1993), pp. 111–195.

[32] aS Woutersen, U Emmerichs, and HJ Bakker. "Femtosecond mid-IR pump-probe spectroscopy of liquid water: Evidence for a two-component structure". In: *Science* 278.5338 (1997), pp. 658–660.

[33] T Pfeifer, Ch Spielmann, and G Gerber. "Femtosecond x-ray science". In: *Reports on Progress in Physics* 69.2 (2006), p. 443.

[34] Adrian L Cavalieri et al. "Attosecond spectroscopy in condensed matter". In: *Nature* 449.7165 (2007), p. 1029.

[35] DG Cooke et al. "Electron mobility in dilute GaAs bismide and nitride alloys measured by time-resolved terahertz spectroscopy". In: *Applied Physics Letters* 89.12 (2006), p. 122103.

[36] Masaki Takihara, Takuji Takahashi, and Toru Ujihara. "Minority carrier lifetime in polycrystalline silicon solar cells studied by photoassisted Kelvin probe force microscopy". In: *Applied Physics Letters* 93.2 (2008), p. 021902.

[37] Franz J Giessibl. "Forces and frequency shifts in atomic-resolution dynamic-force microscopy". In: *Physical Review B* 56.24 (1997), p. 16010.

[38] Herbert Goldstein. *Classical Mechanics*. Pearson Education India, 2011.

[39] Joseph M Crowley. "Simple expressions for force and capacitance for a conductive sphere near a conductive wall". In: *Proc. ESA Annu. Meet. Electrostatics* (2008).

[40] Freeman Dyson. "A meeting with Enrico Fermi". In: *Nature* 427.6972 (2004), p. 297.

[41] John E Sader and Suzanne P Jarvis. "Accurate formulas for interaction force and energy in frequency modulation force spectroscopy". In: *Applied Physics Letters* 84.10 (2004), pp. 1801–1803.

[42] John E Sader et al. "Interatomic force laws that evade dynamic measurement". In: *Nature Nanotechnology* 13.12 (2018), p. 1088.

[43] Omur E Dagdeviren et al. "Quantifying Tip-Sample Interactions in Vacuum Using Cantilever-Based Sensors: An Analysis". In: *Physical Review Applied* 9.4 (2018), p. 044040.

[44] S Hudlet et al. "Evaluation of the capacitive force between an atomic force microscopy tip and a metallic surface". In: *The European Physical Journal B-Condensed Matter and Complex Systems* 2.1 (1998), pp. 5–10.

[45] John E Sader et al. "A virtual instrument to standardise the calibration of atomic force microscope cantilevers". In: *Review of Scientific Instruments* 87.9 (2016), p. 093711.

[46] Hans-Jürgen Butt, Brunero Cappella, and Michael Kappl. "Force measurements with the atomic force microscope: Technique, interpretation and applications". In: *Surface Science Reports* 59.1-6 (2005), pp. 1–152.

[47] J Colchero, A Gil, and AM Baró. "Resolution enhancement and improved data interpretation in electrostatic force microscopy". In: *Physical Review B* 64.24 (2001), p. 245403.

[48] André Schirmeisen et al. "Metallic adhesion and tunnelling at the atomic scale". In: *New Journal of Physics* 2.1 (2000), p. 29.

[49] H-J Güntherodt, D Anselmetti, and Ernst Meyer. *Forces in scanning probe methods*. Vol. 286. Springer Science & Business Media, 2012.

[50] William G Cochran. “Some methods for strengthening the common $\chi$ 2 tests”. In: *Biometrics* 10.4 (1954), pp. 417–451.

[51] Durmus U Karatay et al. “Fast time-resolved electrostatic force microscopy: Achieving sub-cycle time resolution”. In: *Review of Scientific Instruments* 87.5 (2016), p. 053702.

[52] Alfred John Weymouth and Franz J Giessibl. “The Phantom Force”. In: *Noncontact Atomic Force Microscopy*. Springer, 2015, pp. 71–92.

[53] D Rugar, HJ Mamin, and Peter Guethner. “Improved fiber-optic interferometer for atomic force microscopy”. In: *Applied Physics Letters* 55.25 (1989), pp. 2588–2590.

[54] Daniel Kiracofe et al. “High efficiency laser photothermal excitation of microcantilever vibrations in air and liquids”. In: *Review of Scientific Instruments* 82.1 (2011), p. 013702.

[55] Zeno Schumacher et al. “Measurement of surface photovoltage by atomic force microscopy under pulsed illumination”. In: *Physical Review Applied* 5.4 (2016), p. 044018.

# Preface to Chapter 4

To perform quantitative force measurements using AFM, including some of those described in Chapter 3, requires an accurate knowledge of the spring constant of the cantilever. Currently, the most prevalent method of calibrating this is to measure the small mechanical oscillations of the cantilever due to its thermal energy, which can be used to extract the resonance frequency and quality factor. There have been recent studies on the accuracy of these measurements that have demonstrated large variations even when the exact same cantilever is measured using different microscopes [98, 99]. In the following chapter, the accuracy of these measurements in the presence of ambient acoustic noise will be discussed, along with recommendations for reducing potential systematic errors. The following is the integral text from:

Mascaro, Aaron, et al. "Eliminating the effect of acoustic noise on cantilever spring constant calibration" *Applied Physics Letters* 133, 233105 (2018).

# 4

# Eliminating the effect of acoustic noise on cantilever spring constant calibration

Aaron Mascaro[a)], Yoichi Miyahara, Omur E. Dagdeviren, and Peter Grütter

*Department of Physics, McGill University, 3600 rue University, Montreal, Québec H3A2T8, Canada*

[a)]E-mail: *mascaroa@physics.mcgill.ca*

# Abstract

A common use for atomic force microscopy is to quantify local forces through tip-sample interactions between the probe tip and a sample surface. The accuracy of these measurements depends on the accuracy to which the cantilever spring constant is known. Recent work has demonstrated that the measured spring constant of a cantilever can vary up to a factor of five, even for the exact same cantilever measured by different users on different microscopes. Here we demonstrate that a standard method for calibrating the spring constant (using the oscillations due to thermal energy) is susceptible to ambient acoustic noise, which can alter the result significantly. We demonstrate a step-by-step method to measure the spring constant by actively driving the cantilever to measure the resonance frequency and quality factor, giving results that are unaffected by acoustic noise. Our method can be performed rapidly on any atomic force microscope without any expensive additional hardware.


## 4.1 Introduction

The atomic force microscope (AFM) has become an invaluable tool across many areas of materials science research due to its ability to probe structural and electrical properties of materials with extremely high spatial resolution. Modern AFMs rely on a micro-fabricated sharp probe tip protruding from the end of a cantilever beam to sense exceptionally small forces [1–5]. In many experiments the interaction force itself is to be measured, which is generally done by measuring the change in the mechanical status of the cantilever (static deflection, oscillation amplitude, or change in resonance frequency) as it interacts with the surface [4, 6–9]. Independent of the operation mode of the AFM, the spring constant of the cantilever needs to be known to convert the measured cantilever response to units of force, which can then be used to quantify the tip-sample interaction

strength [3, 10–12].

There are several methods currently used to quantify spring constants including the method of Cleveland et al. [13] where the cantilever's resonance frequency ($\omega_0$) is measured before and after adding known masses to the end of the cantilever, and Sader's method [14], which requires knowledge of the cantilever's resonance frequency ($\omega_0$), quality factor ($Q$), plan-view dimensions (length $L$ and width $b$), and the viscous medium the cantilever resides in (typically air). Due to its non-invasive nature, Sader's method has been widely adopted across commercial AFM systems for cantilever spring constant calibration. A common implementation of Sader's method is to measure the power spectral density (PSD) of the cantilever's deflection to observe the thermal oscillations, which can then be used to extract both the quality factor and resonance frequency, although Sader's method is fundamentally agnostic as to how the quality factor and resonance frequency are actually measured. Sader et al. have recently shown that the variation on these parameters obtained by fitting the measured thermal PSD can lead to differences of up to a factor of 5 in the spring constant obtained using Sader's method by different users on different microscopes even for the exact same cantilever, while a previous study by te Reit et al. demonstrated variations of up to a factor of 2 [15, 16]. This technique assumes that thermal fluctuations are the sole driving force acting on the cantilever, which results in spectrally white multiplicative noise [17]. This may be true in many cases, however, we demonstrate that additional noise sources such as ambient acoustic noise can cause the overall driving force to deviate from white Gaussian noise, which can alter the values obtained by fitting the measured PSD to that of a damped driven harmonic oscillator driven by Brownian noise. Furthermore, we demonstrate that by actively driving the cantilever we can obtain reliable measurements of the resonance frequency and quality factor that are impervious to increased ambient acoustic noise levels.

## 4.2 Results

### 4.2.1 Thermal Spectrum Measurements

Figures 4.1(a) and 4.1(c) show typical frequency spectra of the thermal oscillation peaks of two different cantilevers (Type 1: OPUS 4XC-NN-A, and Type 2: OPUS 4XC-NN-B) obtained by recording the AFM deflection signal at a sample rate of 2.5MHz for 2.5s, taking a fast-fourier transform (FFT), and then averaging 50 times (similar to the procedure in Ref. [18]). Modelling the cantilevers as damped driven harmonic oscillators, the frequency spectra of the oscillation peaks are given by:

$$F(\omega, \bar{\alpha}) = \frac{\alpha_1/\omega_0^2}{(1-(\omega/\omega_0)^2)^2 + (\omega/\omega_0 Q)^2} + \alpha_2 \tag{4.1}$$

where $F(\omega, \bar{\alpha})$ is the power spectral density (PSD) (in $V^2$/Hz or $m^2$/Hz), $\alpha_1$ is the amplitude, and $\alpha_2$ is the baseline noise level. A least-squares fit to the logarithm of Equation 4.1 is shown as the solid black line in each panel of Figure 4.1, where the window sizes are large compared to the spectral width of the lorentzians (corresponding to a normalized window size of $\beta \approx 17$ as defined by Sader et al. [19]), which results in small uncertainties on the fit parameters. Since the thermal noise is multiplicative, taking the logarithm of both sides of Equation 4.1 removes the weighting of the squared errors in the least-squares minimization procedure and results in residuals that are zero-centered. Fitting the PSD data directly (without taking the logarithm) decreases the effect of the off-resonance background noise, but is still significantly influenced by noise on the resonance peak (see Supplementary Materials, Figure S4, Appendix C).

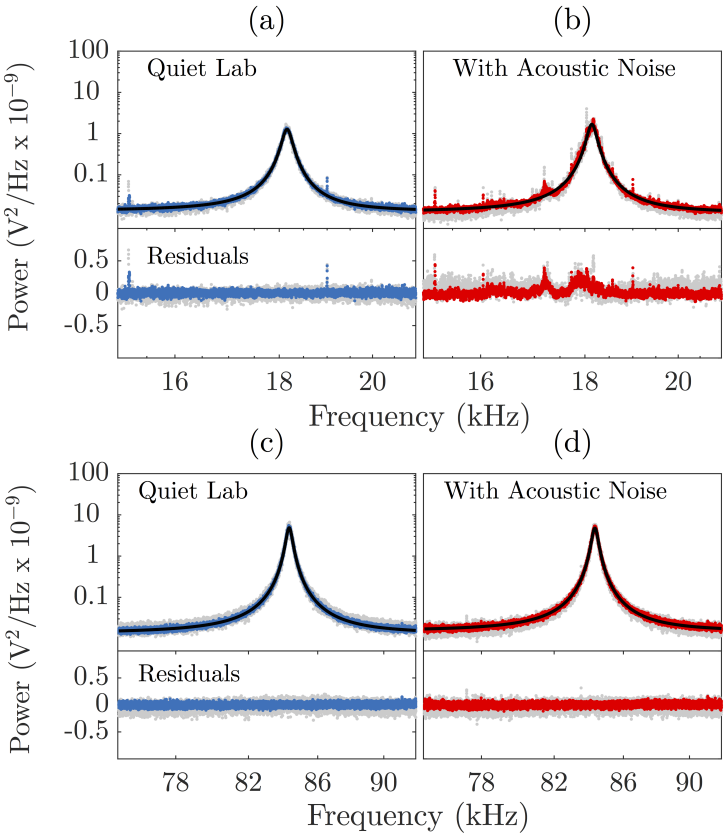


Figure 4.1: Measured PSD around the cantilever resonance for cantilever 1 - A: **(a)** without acoustic noise and **(b)** with ambient acoustic noise; and cantilever 2 - A: **(c)** without acoustic noise and **(d)** with ambient acoustic noise. Coloured data are the average of 5 independent measurements of 50 spectra averaged together, while the grey data shows one such measurement of 50 spectra averaged. Black lines are the fits to the logarithm of Equation 4.1.

### 4.2.2 Ambient Acoustic Noise

To study the effect of ambient noise on the measurements, a speaker (Motorola J03 type) was connected to the output of a function generator (Agilent 33220a) outputting white noise with a bandwidth of 9MHz and placed near the AFM. A similar experiment was conducted by Koralek et al. in which an AFM cantilever was driven by applying a white noise signal to the drive piezo in the cantilever holder allowing them to emulate thermal oscillations of the cantilever at much higher temperatures than physically accessible [20]. In our case the noise source is only coupled to the cantilever via air and thus simulates the effect of increased ambient acoustic noise. The frequency spectra for cantilevers 1 - A and 2 - A with ambient acoustic noise are shown in Figures 4.1(b) and 4.1(d). To preclude effects of slowly changing extrinsic variables that could affect the measurements, the quiet and noisy measurements were done in an alternating fashion.

Equation 4.1 was used to determine the quality factor, resonance frequency, baseline noise level, and amplitude of four different cantilevers, two of Type 1 with resonance frequencies in the audio range (∼20kHz), and two of Type 2 with resonance frequencies well into the ultrasonic range (∼80kHz). These results are shown in Figures 4.2(b)-(c) where the error bars are the standard deviation of the mean for 5 independent measurements of each cantilever. The shaded regions are the theoretical uncertainties for the fit parameters calculated using the formulas in Refs. [19] and [18] (see Supplementary Materials, Appendix C). The 'noisy' data (red data points in Figure 4.2) are values obtained from fitting the frequency spectra with ambient acoustic noise as described.

The spring constant for a rectangular cantilever can be directly calculated by:

$$k_n = 0.1906\rho b^2 LQ\,\Gamma_i(\omega_0)\omega_0^2 \tag{4.2}$$

where the prefactor (0.1906) comes from the normalized effective mass and $\Gamma_i$ is the

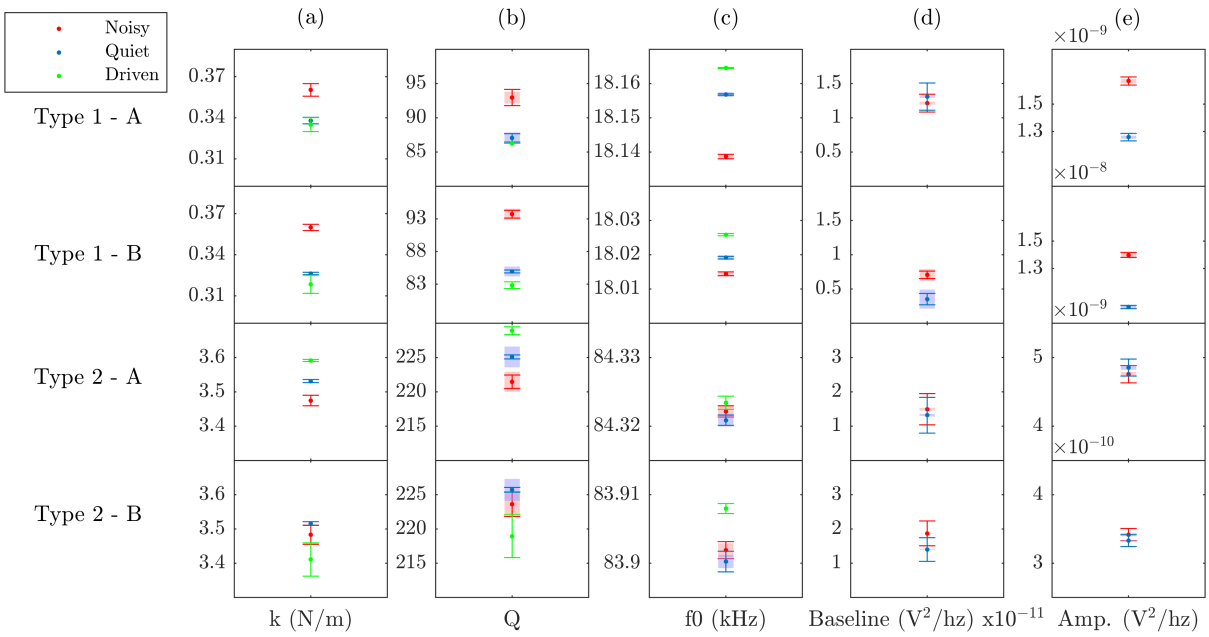


Figure 4.2: **(a)** Spring constants obtained from Equation 4.2. **(b)** quality factors, **(c)** resonance frequencies ($\omega_0/2\pi$), **(d)** baseline noise levels ($\alpha_2$) and **(e)** peak amplitudes ($\alpha_1$) obtained from fitting the 'thermal' oscillation PSD measurements of 4 different cantilevers with (red) and without (blue) ambient acoustic noise to Equation 4.1. Results for the driven-calibration method described in the text are shown in green. Error bars are the uncertainty on the mean from 5 measurements on each cantilever. Shaded regions are theoretical uncertainties on the fit parameters calculated using the formulas given in Refs. [19] and [18].

imaginary component of the hydrodynamic function [14]. The spring constants for all four cantilevers were calculated using Equation 4.2 and are shown in Figure 4.2(a).

To study the systematic effect of the acoustic noise level on the fit parameters, PSDs were also taken with increasing acoustic noise and the spring constants obtained from the fit parameters (Q and f0) were examined (see Supplementary Materials, Appendix C). The result shown in Figure 4.3 demonstrates a clear systematic change in measured spring constant with increasing acoustic noise (shown for cantilever 1 - A).

## 4.3 Driven Techniques

### 4.3.1 Resonance Frequency

Another method of measuring the resonance frequency is to drive the cantilever using a sine wave and sweeping its frequency. This can be done using a piezo-acoustic drive, which is susceptible to the non-flat transfer function of the system [21]. Since the quality factor is equal to $f_0$/FWHM (where $f_0$ is the resonance frequency in Hz and FWHM is the full width at half-max of the resonance peak) and typical quality factors are ∼200 for the ∼80kHz cantilevers used in this experiment, the frequency span required to measure $Q$ from a driven spectrum would be at least 1kHz. Thus, determing $Q$ from a driven cantilever response by fitting the peak would be highly susceptible to transfer function irregularities and/or spurious resonances within this ∼1kHz range. We can, however, measure the resonance frequency of the cantilever very accurately by sweeping over a small frequency window and fitting the response to Equation 4.1 as the transfer function should have a minimal impact as long as the frequency span is small enough (see Supplementary Materials, Figures S1 and S2, Appendix C). Multiple measurements on cantilever Type 2 - A are shown in Figure 4.4(a) along with their fitted curves (black lines). The inset shows the accuracy of the fits, each measurement is within 2Hz of the mean and the uncertainty on the mean is under 1Hz. The measurement is unaffected by adding acoustic noise (i.e. the results with and without noise are the same), which is expected because the additional acoustic energy being added to the system is orders of magnitude smaller than the kinetic energy of the driven cantilever.

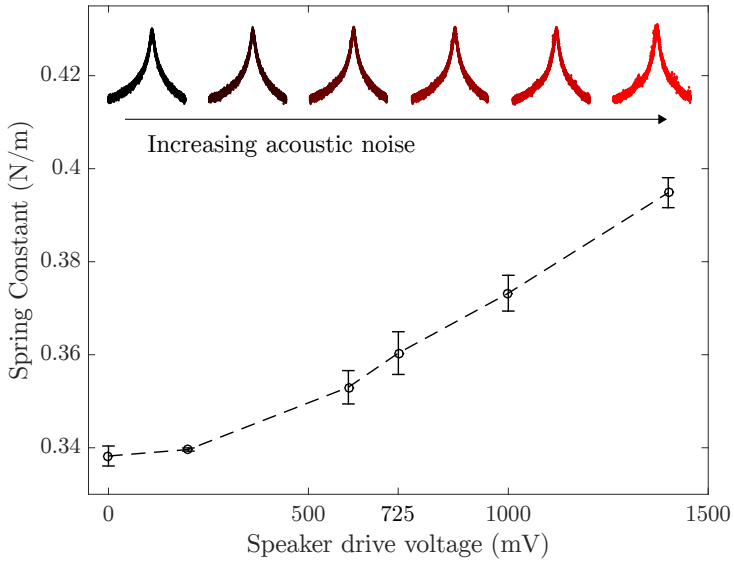


Figure 4.3: Spring constant obtained from thermal PSDs for cantilever 1 - A as a function of white noise drive voltage sent to the speaker. Inset plots show the raw spectra for each of the 6 data points.

### 4.3.2 Quality Factor

To measure the quality factor using a driven technique we can simply record the ringdown time. This was performed by driving the cantilevers at the resonance frequency previously measured and suddenly turning off the driving force. By directly recording the AFM deflection signal we can observe the oscillation amplitude decreasing, as shown in Figure 4.4(b). The peak values can be easily extracted using a peak-finding algorithm, and they decrease exponentially over time, given by:

$$y = Ae^{-t/\tau} \tag{4.3}$$

where $\tau$ is the decay time constant and $A$ is the exponential prefactor. The quality factor is related to the decay time constant by:

$$Q = \tau f_0 \pi \tag{4.4}$$

In fitting the peak amplitudes to Equation 4.3, one has to be aware of the effect of

the non-zero noise floor of the measurement device. This becomes apparent when plotted on a log-log scale: as the peak values approach the noise floor they begin to deviate from the expected straight-line behaviour, as shown by the red data points in Figure 4.4(c). This can easily be corrected for by simply measuring the noise-floor, which we define as the peak-to-peak noise on the deflection signal with the drive turned off, and then only including peak values greater than this value in the fit. These are shown in blue in Figure 4.4(c), while the red data points were not included in the fit.

Measuring the ringdown with the initial drive frequency slightly off resonance was also investigated to determine how accurately the resonance frequency must be measured initially. There were no significant deviations in the measured quality factor with the drive frequency within approximately $\pm$10Hz of resonance, thus demonstrating the robustness of this technique (see Supplementary Materials, Figure S3, Appendix C).

The results for each cantilever from the sweep and ringdown measurements are shown in green in Figure 4.2. The same values were obtained with and without ambient acoustic noise.

Although we used the ringdown method for quality factor measurements, there exist other driven techniques to extract the quality factor as well, including by taking the derivative of the measured phase vs. frequency data. This quantity is related to the quality factor by $\frac{d\phi}{d\omega}|_{\omega=\omega_0} = 2Q/\omega_0$ where $\phi$ is the oscillator phase with respect to the drive signal [22]. The main drawback of this technique is the numerical derivative that must be computed, which is widely known to greatly amplify noise present in the data. This technique therefore requires significant averaging in order to obtain reliable results, and in addition it is also susceptible to transfer function irregularities as with any measurement where the drive frequency is swept. The ringdown technique, on the other hand, requires excitation at a single frequency and is thus impervious to effects related to the mechanical transfer function.

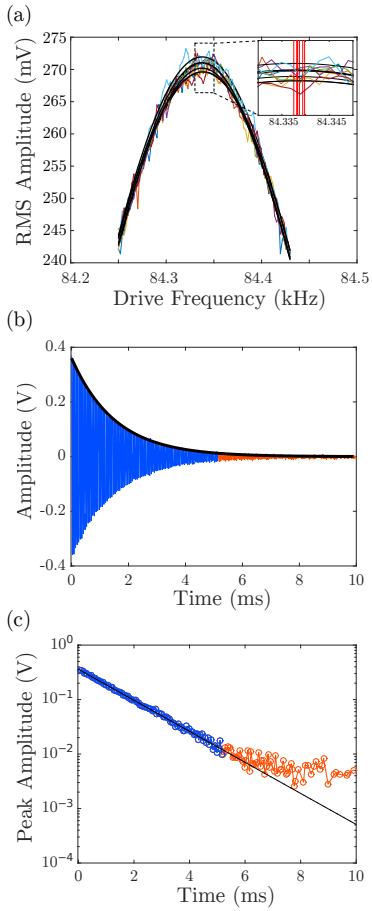


Figure 4.4: **(a)** Driven response amplitude (RMS) of cantilever 1 - A across the resonance frequency showing curves fitted to Equation 4.1. Inset shows a closeup where the red vertical lines mark the resonance frequency obtained from each fitted curve. **(b)** AFM deflection signal directly after turning off the driving force (at t=0) along with the fit to Equation 4.3 for multiple measurements on cantilever Type 1 - A. **(c)** Driven response amplitude (RMS) of cantilever Type 1 - A across the resonance frequency showing curves fitted to 4.1. Inset shows a closeup where the red vertical lines mark the resonance frequency obtained from each fitted curve.

## 4.4 Discussion

As can be observed in Figure 4.1, ambient acoustic noise can affect the measured PSD. This is immediately apparent in the case of the audio-frequency range cantilever Type 1- A (Figures 4.1(a) and (b)), while the spectrum for the ultrasonic frequency-range cantilever Type 2 - A is visually indistinguishable with and without ambient acoustic noise (Figures 4.1(c) and (d)). As shown in Figure 4.2(a), the spring constant obtained from fitting

the thermal PSD may be systematically overestimated by 10% in some cases (Type 1 cantilevers), while in others it may be underestimated (Type 2 - A), and in the best case there is no observed difference (Type 2 - B). Using the driven techniques we described, however, yeilded spring constants that were consistent with those obtained from the quiet thermal spectrum measurements and unaffected by acoustic noise.

The Type 2 cantilevers have both larger spring constants and resonance frequencies in the ultrasonic range. The acoustic noise generated by the speaker does extend well into the ultrasound, however atmospheric attenuation at higher frequencies is known to be severe [23]. Thus, as expected, the stiffer, higher frequency cantilevers are less affected by ambient acoustic noise, but not impervious to it. To understand why the fit results differ for cantilever 2 - A even though there are no clear visual differences in the data, it is instructive to look at the variance of the residuals ($R$) since the residuals are proportional to the logarithm of the noise. Taking $\mathrm{Var}[10^R]$ where $R = \log_{10}[y] - \log_{10}[F(\omega, \bar{\alpha})]$ (i.e. the logarithm of the data minus the logarithm of the fit function, Equation 4.1, which gives a unitless quantity) we can compare how 'noisy' the residuals are. For cantilever 1 - A the variances are: $3.0 \pm 0.3 \times 10^{-2}$ for the quiet data and $5.8 \pm 0.4 \times 10^{-2}$ for the noisy data, while for cantilever 2 - A the variances are: $2.06 \pm 0.04 \times 10^{-2}$ for the quiet data and $2.42 \pm 0.04 \times 10^{-2}$ for the noisy data. In both cases the residuals are significantly noisier when the acoustic noise is on.

This discrepancy is fundamentally due to the fact that the observed spectrum is not always thermally limited; there can be contributions from various sources of detection noise (e.g. optical shot noise), electronic noise, and mechanical vibrations (e.g. acoustic noise from vacuum pumps). The former have been investigated comprehensively for optical beam deflection systems such as the one used here [24–28], while the effect of mechanical vibrations on the thermal oscillations of tuning forks have been discussed in brief [29]. Since the energy of the thermal oscillations is so small, even a small amount

of mechanical noise (acoustic or otherwise) can have a non-negligible effect and lead to deviations from a spectrally white driving force. This is evident in the residuals plotted in Figure 4.1(b). The deviation from a Lorentzian is due to the acoustic energy being converted into mechanical oscillations of the cantilever around the cantilever's resonance frequency. Note that the mechanical transfer function of an AFM system is not flat in frequency due to many unavoidable non-linear mechanical couplings existing between the different microscope components. It is these couplings that lead to frequency dependent phase shifts described and measured in Ref. [21]. The exact mechanism by which acoustic noise presents in the cantilever deflection PSD is expected to be highly dependent on the geometry of the microscope and the noise source itself. By actively driving the cantilevers, however, the energy of the mechanical oscillations can be increased well above the noise floor making them insensitive to ambient acoustic noise.

### 4.4.1 Conclusion

As we have shown, ambient acoustic noise can introduce systematic errors into thermal measurements of cantilever quality factors, which can propagate to errors in calculated spring constants. This effect is especially pronounced for cantilevers with resonance frequencies in the audio range (<20kHz), but can also be present for cantilevers with resonance frequencies well above this. By actively driving the cantilever to measure the resonance frequency and quality factor, the effect of acoustic noise can be mitigated. The quality factor can reliably be measured by recording the ringdown directly and fitting this to a decaying exponential. The fit should be done such that only data above the noise floor is included. This procedure results in highly reproducible measurements that can be used to calculate the spring constant of a cantilever using standard techniques. It also precludes systematic errors due to ambient acoustic noise, which may contribute to observed differences in cantilever spring constants obtained on different atomic force

microscopes and/or by different users.

See supplementary material for transfer function effects, the effect of drive frequency on ringdown, results of fitting PSDs directly, and effects of acoustic noise on $f_0$ and $Q$.

The authors acknowledge financial support from the Natural Sciences and Engineering Research Council of Canada, and the Fonds de recherche du Quebec - Nature et Technologies.

# References

[1] TR Albrecht et al. "Microfabrication of cantilever styli for the atomic force microscope". In: *Journal of Vacuum Science & Technology A: Vacuum, Surfaces, and Films* 8.4 (1990), pp. 3386–3396.

[2] Frank Ohnesorge and Gerd Binnig. "True atomic resolution by atomic force microscopy through repulsive and attractive forces". In: *Science* 260.5113 (1993), pp. 1451–1456.

[3] Hans-Jürgen Butt, Brunero Cappella, and Michael Kappl. "Force measurements with the atomic force microscope: Technique, interpretation and applications". In: *Surface science reports* 59.1-6 (2005), pp. 1–152.

[4] Roberto Raiteri et al. "Micromechanical cantilever-based biosensors". In: *Sensors and Actuators B: Chemical* 79.2-3 (2001), pp. 115–126.

[5] Franz J Giessibl. "Atomic resolution of the silicon (111)-(7x7) surface by atomic force microscopy". In: *Science* 267.5194 (1995), pp. 68–71.

[6] Mo Li, Hong X Tang, and Michael L Roukes. "Ultra-sensitive NEMS-based cantilevers for sensing, scanned probe and very high-frequency applications". In: *Nature nanotechnology* 2.2 (2007), p. 114.

[7] Aleksandr Noy, Dmitri V Vezenov, and Charles M Lieber. "Chemical force microscopy". In: *Annual Review of Materials Science* 27.1 (1997), pp. 381–421.

[8] Paul A Wiggins et al. "High flexibility of DNA on short length scales probed by atomic force microscopy". In: *Nature nanotechnology* 1.2 (2006), p. 137.

[9] Nina Balke et al. "Exploring local electrostatic effects with scanning probe microscopy: implications for piezoresponse force microscopy and triboelectricity". In: *ACS nano* 8.10 (2014), pp. 10229–10236.

[10] Franz Josef Gießibl. "A direct method to calculate tip–sample forces from frequency shifts in frequency-modulation atomic force microscopy". In: *Applied Physics Letters* 78.1 (2001), pp. 123–125.

[11] John E Sader and Suzanne P Jarvis. "Accurate formulas for interaction force and energy in frequency modulation force spectroscopy". In: *Applied Physics Letters* 84.10 (2004), pp. 1801–1803.

[12] Ricardo Garcıa and Ruben Perez. "Dynamic atomic force microscopy methods". In: *Surface science reports* 47.6-8 (2002), pp. 197–301.

[13] JP Cleveland et al. "A nondestructive method for determining the spring constant of cantilevers for scanning force microscopy". In: *Review of scientific instruments* 64.2 (1993), pp. 403–405.

[14] John E Sader, James WM Chon, and Paul Mulvaney. "Calibration of rectangular atomic force microscope cantilevers". In: *Review of Scientific Instruments* 70.10 (1999), pp. 3967–3969.

[15] John E Sader et al. "A virtual instrument to standardise the calibration of atomic force microscope cantilevers". In: *Review of Scientific Instruments* 87.9 (2016), p. 093711.

[16] Joost Te Riet et al. “Interlaboratory round robin on cantilever calibration for AFM force spectroscopy”. In: *Ultramicroscopy* 111.12 (2011), pp. 1659–1669.

[17] Lev Davidovich Landau and Evgenii Mikhailovich Lifshitz. *Course of theoretical physics*. Elsevier, 2013.

[18] John E Sader et al. “Effect of multiplicative noise on least-squares parameter estimation with applications to the atomic force microscope”. In: *Review of Scientific Instruments* 83.5 (2012), p. 055106.

[19] John E Sader, Morteza Yousefi, and James R Friend. “Uncertainty in least-squares fits to the thermal noise spectra of nanomechanical resonators with applications to the atomic force microscope”. In: *Review of Scientific Instruments* 85.2 (2014), p. 025104.

[20] DO Koralek et al. “Probing deep interaction potentials with white-noise-driven atomic force microscope cantilevers”. In: *Applied Physics Letters* 76.20 (2000), pp. 2952–2954.

[21] Aleksander Labuda et al. “Decoupling conservative and dissipative forces in frequency modulation atomic force microscopy”. In: *Physical Review B* 84.12 (2011), p. 125433.

[22] Jerry B Marion. *Classical dynamics of particles and systems*. Academic Press, 2013.

[23] Beatrice D Lawrence and James A Simmons. “Measurements of atmospheric attenuation at ultrasonic frequencies and the significance for echolocation by bats”. In: *The Journal of the Acoustical Society of America* 71.3 (1982), pp. 585–590.

[24] H-J Butt and Manfred Jaschke. “Calculation of thermal noise in atomic force microscopy”. In: *Nanotechnology* 6.1 (1995), p. 1.

[25] Takeshi Fukuma. "Wideband low-noise optical beam deflection sensor with photothermal excitation for liquid-environment atomic force microscopy". In: *Review of Scientific Instruments* 80.2 (2009), p. 023707.

[26] Franz J Giessibl et al. "Calculation of the optimal imaging parameters for frequency modulation atomic force microscopy". In: *Applied Surface Science* 140.3-4 (1999), pp. 352–357.

[27] Aleksander Labuda, Jeffrey R Bates, and Peter H Grütter. "The noise of coated cantilevers". In: *Nanotechnology* 23.2 (2011), p. 025503.

[28] Frederick Gittes and Christoph F Schmidt. "Thermal noise limitations on micromechanical experiments". In: *European biophysics journal* 27.1 (1998), pp. 75–81.

[29] Joachim Welker, Frederico de Faria Elsner, and Franz J Giessibl. "Application of the equipartition theorem to the thermal excitation of quartz tuning forks". In: *Applied Physics Letters* 99.8 (2011), p. 084102.

# 5

# Conclusion

Throughout the previous chapters, a variety of quantitative measurements performed using AFM have been discussed. In Chapter 2, time-domain electrostatic force microscopy was conducted on several $LiFePO_4$ samples, including the well-characterized hydrothermal platelets. This allowed for quantitative extraction of the local ionic relaxation times, which was then used to calculate the activation energies by performing these measurements as a function of temperature. By correlating this with other characterizations performed at the exact same location, these activation energies were then used to quantitatively validate hopping barriers calculated using DFT. This demonstrates the true power of time-resolved EFM measurements, especially in their ability to extract the full functional form of the sample response, i.e. the stretched exponential. The stretching factor contains crucial information regarding the collective transport of the ions and is thus a key parameter to extract from the measured data. Moving to even faster ionic conductors will require a significant improvement in the time resolution; the smallest platelets measured in this experiment were nearing the time resolution limit for direct time-domain measurements. This was discussed in detail in Chapter 3 where the time resolution limit was experimentally demonstrated. Four other techniques were then in-

vestigated for conducting ionic transport measurements; voltage-pulse averaging EFM (newly developed), fast free time-resolved EFM, phase-kick EFM, and intermodulation spectroscopy. All of these techniques perform very well on validation measurements of conducting samples (most of them using known signals to determine the accuracy of the extracted response times), however, all of them have significant challenges associated with measuring ionic transport. A common challenge to each of them is the stretched exponential response, which drastically increases the difficulty in analyzing the acquired data. It is also noteworthy that each of these techniques required assumptions regarding the functional form of the time-evolution of the system, which may not always be known *a priori*. At present it is not clear which (if any) of these techniques will obtain the level of signal fidelity in their reconstructed sample responses in order to accurately measure ionic transport.

Another aspect considered in this thesis is the accuracy of cantilever spring constant calibration. Accurate knowledge of a cantilever's spring constant is essential for performing quantitative force measurements, or even for simple calibration of the amplitude for dynamic modes like tapping mode and FM-AFM. We demonstrated that ambient acoustic noise can significantly impact the measured spring constant (by >10% in some cases), which can be problematic if adequate acoustic isolation is not available/possible. It was then shown that driven techniques to measure the resonance frequencies and quality factors – frequency sweeps and amplitude ringdown measurements – are impervious to acoustic noise at the levels studied here. This is a significant finding, and the recommended protocol is expected to reduce the variation in cantilever spring constants measured by different users on different microscopes.

It is expected that quantitative AFM-based measurements will become increasingly popular as they gain in accessibility and usefulness in terms of the information they are able to extract. These techniques allow for highly localized measurements of various prop-

erties, including ionic transport, as was demonstrated throughout this thesis. Localized measurements are crucial in understanding effects related to inhomogeneities, which are especially prevalant in battery materials. The ability to correlate these measurements with other techniques to develop a full picture that relates local composition, structure, and transport properties makes the atomic force microscope an extremely powerful tool in this field. Continued advancement in extracting time-resolved signals from EFM measurements is essential for furthering our collective understanding of ionic transport and its limitations.

# References


[1] Intergovernmental Panel on Climate Change. *Climate change 2014: Mitigation of climate change*. Vol. 3. Cambridge University Press, 2015.

[2] Christian Breyer et al. "Solar photovoltaics demand for the global energy transition in the power sector". In: *Progress in Photovoltaics: Research and Applications* 26.8 (2018), pp. 505–523.

[3] Zachary P Cano et al. "Batteries and fuel cells for emerging electric vehicle markets". In: *Nature Energy* 3.4 (2018), p. 279.

[4] EV-Volumes. *Global Plug-in Sales for 2016, 2016*. `http://www.ev-volumes.com/news/global-plug-in-sales-for-2016/`. Accessed: 05 December 2018.

[5] IEA. *Energy Technology Perspectives, 2017*. `https://www.iea.org/etp2017/`. Accessed: 05 December 2018.

[6] Languang Lu et al. "A review on the key issues for lithium-ion battery management in electric vehicles". In: *Journal of power sources* 226 (2013), pp. 272–288.

[7] Michel Armand and J-M Tarascon. "Building better batteries". In: *nature* 451.7179 (2008), p. 652.

[8] Björn Nykvist and Måns Nilsson. "Rapidly falling costs of battery packs for electric vehicles". In: *nature climate change* 5.4 (2015), p. 329.

[9] Bruno Scrosati, Jusef Hassoun, and Yang-Kook Sun. "Lithium-ion batteries. A look into the future". In: *Energy & Environmental Science* 4.9 (2011), pp. 3287–3295.

[10] George E Blomgren. "The development and future of lithium ion batteries". In: *Journal of The Electrochemical Society* 164.1 (2017), A5019–A5025.

[11] Bruno Scrosati. "History of lithium batteries". In: *Journal of solid state electrochemistry* 15.7-8 (2011), pp. 1623–1630.

[12] M Stanley Whittingham. "Chemistry of intercalation compounds: metal guests in chalcogenide hosts". In: *Progress in Solid State Chemistry* 12.1 (1978), pp. 41–99.

[13] Pallavi Verma, Pascal Maire, and Petr Novák. "A review of the features and analyses of the solid electrolyte interphase in Li-ion batteries". In: *Electrochimica Acta* 55.22 (2010), pp. 6332–6341.

[14] Peter G Bruce, Bruno Scrosati, and Jean-Marie Tarascon. "Nanomaterials for rechargeable lithium batteries". In: *Angewandte Chemie International Edition* 47.16 (2008), pp. 2930–2946.

[15] Perla B Balbuena and Yixuan Wang. *Lithium-ion batteries: solid-electrolyte interphase*. Imperial college press, 2004.

[16] Huiqiao Li and Haoshen Zhou. "Enhancing the performances of Li-ion batteries by carbon-coating: present and future". In: *Chemical Communications* 48.9 (2012), pp. 1201–1217.

[17] J Maier. "Nanoionics: ion transport and electrochemical storage in confined systems". In: *Materials For Sustainable Energy: A Collection of Peer-Reviewed Research and Review Articles from Nature Publishing Group*. World Scientific, 2011, pp. 160–170.

[18] Lars Ole Valøen and Jan N Reimers. "Transport properties of LiPF6-based Li-ion battery electrolytes". In: *Journal of The Electrochemical Society* 152.5 (2005), A882–A891.

[19] Michael M Thackeray, Christopher Wolverton, and Eric D Isaacs. "Electrical energy storage for transportation—approaching the limits of, and going beyond, lithium-ion batteries". In: *Energy & Environmental Science* 5.7 (2012), pp. 7854–7863.

[20] Naoki Nitta et al. "Li-ion battery materials: present and future". In: *Materials today* 18.5 (2015), pp. 252–264.

[21] Liumin Suo et al. "A new class of solvent-in-salt electrolyte for high-energy rechargeable metallic lithium batteries". In: *Nature communications* 4 (2013), p. 1481.

[22] Maciej Galiński, Andrzej Lewandowski, and Izabela Stępniak. "Ionic liquids as electrolytes". In: *Electrochimica acta* 51.26 (2006), pp. 5567–5580.

[23] Byoungwoo Kang and Gerbrand Ceder. "Battery materials for ultrafast charging and discharging". In: *Nature* 458.7235 (2009), pp. 190–193.

[24] Yonggang Wang et al. "Nano active materials for lithium-ion batteries". In: *Nanoscale* 2.8 (2010), pp. 1294–1305.

[25] Rahul Malik et al. "Particle size dependence of the ionic diffusivity". In: *Nano letters* 10.10 (2010), pp. 4123–4127.

[26] B Ellis et al. "Nanostructured materials for lithium-ion batteries: Surface conductivity vs. bulk ion/electron transport". In: *Faraday discussions* 134 (2007), pp. 119–141.

[27] RG Fuller. "Point Defects in Solids". In: *Plenum, New York* (1972).

[28] K Funke. "Jump relaxation in solid electrolytes". In: *Prog. Solid State Chem.* 22.2 (1993), pp. 111–195.

[29] HR Glyde. “Rate processes in solids”. In: *Reviews of Modern Physics* 39.2 (1967), p. 373.

[30] Aaron Mascaro. “Development of Scanning Probe Microscopy Techniques for the Study of Lithium Ion Battery Materials”. PhD thesis. McGill University Libraries, 2015.

[31] Miriam Steinhauer et al. “Investigation of the solid electrolyte interphase formation at graphite anodes in lithium-ion batteries with electrochemical impedance spectroscopy”. In: *Electrochimica Acta* 228 (2017), pp. 652–658.

[32] Evgenij Barsoukov and J Ross Macdonald. *Impedance spectroscopy: theory, experiment, and applications*. John Wiley & Sons, 2018.

[33] J Vetter et al. “Ageing mechanisms in lithium-ion batteries”. In: *Journal of power sources* 147.1-2 (2005), pp. 269–281.

[34] Ruhul Amin, Palani Balaya, and Joachim Maier. “Anisotropy of electronic and ionic transport in LiFePO4 single crystals”. In: *Electrochem. Solid-State Lett.* 10.1 (2007), A13–A16.

[35] Bernard A Boukamp. “Electrochemical impedance spectroscopy in solid state ionics: recent advances”. In: *Solid state ionics* 169.1-4 (2004), pp. 65–73.

[36] Simon Müller et al. “Quantifying Inhomogeneity of Lithium Ion Battery Electrodes and Its Influence on Electrochemical Performance”. In: *Journal of The Electrochemical Society* 165.2 (2018), A339–A344.

[37] William C Chueh et al. “Intercalation pathway in many-particle LiFePO4 electrode revealed by nanoscale state-of-charge mapping”. In: *Nano letters* 13.3 (2013), pp. 866–872.

[38] Yiyang Li et al. "Current-induced transition from particle-by-particle to concurrent intercalation in phase-separating battery electrodes". In: *Nature materials* 13.12 (2014), p. 1149.

[39] Veronika Zinth et al. "Inhomogeneity and relaxation phenomena in the graphite anode of a lithium-ion battery probed by in situ neutron diffraction". In: *Journal of Power Sources* 361 (2017), pp. 54–60.

[40] Matilda Klett et al. "Quantifying mass transport during polarization in a Li Ion battery electrolyte by in situ 7Li NMR imaging". In: *Journal of the American Chemical Society* 134.36 (2012), pp. 14654–14657.

[41] Martin Ebner et al. "Visualization and quantification of electrochemical and mechanical degradation in Li ion batteries". In: *Science* 342.6159 (2013), pp. 716–720.

[42] Xiao Hua Liu et al. "In situ atomic-scale imaging of electrochemical lithiation in silicon". In: *Nature nanotechnology* 7.11 (2012), p. 749.

[43] Megan E Holtz et al. "Nanoscale imaging of lithium ion distribution during in situ operation of battery electrode and electrolyte". In: *Nano letters* 14.3 (2014), pp. 1453–1459.

[44] Gerd Binnig and Heinrich Rohrer. "Scanning tunneling microscopy". In: *Surface science* 126.1-3 (1983), pp. 236–244.

[45] Gerd Binnig, Calvin F Quate, and Ch Gerber. "Atomic force microscope". In: *Physical review letters* 56.9 (1986), p. 930.

[46] M Nonnenmacher, MP o?Boyle, and H Kumar Wickramasinghe. "Kelvin probe force microscopy". In: *Applied physics letters* 58.25 (1991), pp. 2921–2923.

[47] P Güthner and K Dransfeld. "Local poling of ferroelectric polymers by scanning force microscopy". In: *Applied Physics Letters* 61.9 (1992), pp. 1137–1139.

[48] DF Ogletree, Robert W Carpick, and Miguel Salmeron. "Calibration of frictional forces in atomic force microscopy". In: *Review of Scientific Instruments* 67.9 (1996), pp. 3298–3306.

[49] SN Magonov, V Elings, and M-H Whangbo. "Phase imaging and stiffness in tapping-mode atomic force microscopy". In: *Surface science* 375.2-3 (1997), pp. L385–L391.

[50] David W Abraham et al. "Lateral dopant profiling in semiconductors by force microscopy using capacitive detection". In: *Journal of Vacuum Science & Technology B: Microelectronics and Nanometer Structures Processing, Measurement, and Phenomena* 9.2 (1991), pp. 703–706.

[51] T Meoded et al. "Direct measurement of minority carriers diffusion length using Kelvin probe force microscopy". In: *Applied physics letters* 75.16 (1999), pp. 2435–2437.

[52] JMR Weaver and HK Wickramasinghe. "Semiconductor characterization by scanning force microscope surface photovoltage microscopy". In: *Journal of Vacuum Science & Technology B: Microelectronics and Nanometer Structures Processing, Measurement, and Phenomena* 9.3 (1991), pp. 1562–1565.

[53] Ch Schönenberger and SF Alvarado. "Observation of single charge carriers by force microscopy". In: *Physical Review Letters* 65.25 (1990), p. 3162.

[54] RJ Hamers and David G Cahill. "Ultrafast time resolution in scanned probe microscopies". In: *Applied physics letters* 57.19 (1990), pp. 2031–2033.

[55] R Bennewitz, M Reichling, and E Matthias. "Force microscopy of cleaved and electron-irradiated CaF 2 (111) surfaces in ultra-high vacuum". In: *Surf. Sci.* 387.1 (1997), pp. 69–77.

[56] A Schirmeisen et al. “Probing ion transport at the nanoscale: Time-domain electrostatic force spectroscopy on glassy electrolytes”. In: *Appl. Phys. Lett.* 85.11 (2004), pp. 2053–2055.

[57] David C Coffey and David S Ginger. “Time-resolved electrostatic force microscopy of polymer solar cells”. In: *Nature Materials* 5.9 (2006), pp. 735–740.

[58] Dmitry Klinov and Sergei Magonov. “True molecular resolution in tapping-mode atomic force microscopy with high-resolution probes”. In: *Applied physics letters* 84.14 (2004), pp. 2697–2699.

[59] TR Albrecht et al. “Frequency modulation detection using high-Q cantilevers for enhanced force microscope sensitivity”. In: *Journal of Applied Physics* 69.2 (1991), pp. 668–673.

[60] Aaron Mascaro et al. “Measuring spatially resolved collective ionic transport on lithium battery cathodes using atomic force microscopy”. In: *Nano Letters* (2017).

[61] Michel Gauthier et al. “Interplay between nonlinearity, scan speed, damping, and electronics in frequency modulation atomic-force microscopy”. In: *Physical review letters* 89.14 (2002), p. 146104.

[62] J Kokavecz et al. “Novel amplitude and frequency demodulation algorithm for a virtual dynamic atomic force microscope”. In: *Nanotechnology* 17.7 (2006), S173.

[63] Sascha Sadewasser and Thilo Glatzel. *Kelvin Probe Force Microscopy: From Single Charge Detection to Device Characterization*. Vol. 65. Springer, 2018.

[64] Yves Martin, David W Abraham, and H Kumar Wickramasinghe. “High-resolution capacitance measurement and potentiometry by force microscopy”. In: *Applied Physics Letters* 52.13 (1988), pp. 1103–1105.

[65] GM Sacha, E Sahagun, and JJ Saenz. "A method for calculating capacitances and electrostatic forces in atomic force microscopy". In: *Journal of Applied Physics* 101.2 (2007), p. 024310.

[66] L Fumagalli et al. "Nanoscale capacitance imaging with attofarad resolution using ac current sensing atomic force microscopy". In: *Nanotechnology* 17.18 (2006), p. 4581.

[67] Andrey V Krayev et al. "Quantitative analysis of dielectric constants from EFM images of multicomponent polymer blends". In: *Macromolecular Chemistry and Physics* 207.11 (2006), pp. 966–969.

[68] PS Crider et al. "Local dielectric spectroscopy of polymer films". In: *Applied physics letters* 91.1 (2007), p. 013102.

[69] Laura Fumagalli et al. "Dielectric-constant measurement of thin insulating films at low frequency by nanoscale capacitance microscopy". In: *Applied Physics Letters* 91.24 (2007), p. 243110.

[70] Wei Lu, Dan Wang, and Liwei Chen. "Near-static dielectric polarization of individual carbon nanotubes". In: *Nano letters* 7.9 (2007), pp. 2729–2733.

[71] C Riedel et al. "Determination of the nanoscale dielectric constant by means of a double pass method using electrostatic force microscopy". In: *Journal of Applied Physics* 106.2 (2009), p. 024315.

[72] Ryan P Dwyer, Sarah R Nathan, and John A Marohn. "Microsecond photocapacitance transients observed using a charged microcantilever as a gated mechanical integrator". In: *Science Advances* 3.6 (2017), e1602951.

[73] J Murawski et al. "Pump-probe Kelvin-probe force microscopy: Principle of operation and resolution limits". In: *Journal of Applied Physics* 118.15 (2015), p. 154302.

[74] Zeno Schumacher et al. “Measurement of surface photovoltage by atomic force microscopy under pulsed illumination”. In: *Physical Review Applied* 5.4 (2016), p. 044018.

[75] S Woutersen, U Emmerichs, and HJ Bakker. “Femtosecond mid-IR pump-probe spectroscopy of liquid water: Evidence for a two-component structure”. In: *Science* 278.5338 (1997), pp. 658–660.

[76] T Pfeifer, Ch Spielmann, and G Gerber. “Femtosecond x-ray science”. In: *Reports on Progress in Physics* 69.2 (2006), p. 443.

[77] Adrian L Cavalieri et al. “Attosecond spectroscopy in condensed matter”. In: *Nature* 449.7165 (2007), p. 1029.

[78] DG Cooke et al. “Electron mobility in dilute GaAs bismide and nitride alloys measured by time-resolved terahertz spectroscopy”. In: *Applied physics letters* 89.12 (2006), p. 122103.

[79] Zeno Schumacher et al. “The limit of time resolution in frequency modulation atomic force microscopy by a pump-probe approach”. In: *Applied Physics Letters* 110.5 (2017), p. 053111.

[80] Doron Aurbach and Yair Cohen. “The application of atomic force microscopy for the study of Li deposition processes”. In: *Journal of The Electrochemical Society* 143.11 (1996), pp. 3525–3532.

[81] Soshi Shiraishi, Kiyoshi Kanamura, and Zen-ichiro Takehara. “Imaging for uniformity of lithium metal surface using tapping mode-atomic force and surface potential microscopy”. In: *The Journal of Physical Chemistry B* 105.1 (2001), pp. 123–134.

[82] LY Beaulieu et al. “Reaction of Li with alloy thin films studied by in situ AFM”. In: *Journal of The Electrochemical Society* 150.11 (2003), A1457–A1464.

[83] A Clemencon et al. “Atomic force microscopy studies of surface and dimensional changes in LixCoO2 crystals during lithium de-intercalation”. In: *Electrochimica acta* 52.13 (2007), pp. 4572–4580.

[84] AE Semenov, IN Borodina, and SH Garofalini. “In Situ Deposition and Ultra-high Vacuum STM/AFM Study of V 2 O 5/Li3 PO 4 Interface in a Rechargeable Lithium-Ion Battery”. In: *Journal of The Electrochemical Society* 148.11 (2001), A1239–A1246.

[85] K Kuriyama et al. “Atomic force microscopy study of surface morphology change in spinel LiMn2O4: possibility of direct observation of Jahn–Teller instability”. In: *Surface science* 601.10 (2007), pp. 2256–2259.

[86] Rui Shao, Sergei V Kalinin, and Dawn A Bonnell. “Local impedance imaging and spectroscopy of polycrystalline ZnO using contact atomic force microscopy”. In: *Appl. Phys. Lett.* 82.12 (2003), pp. 1869–1871.

[87] Ryan O’Hayre, Minhwan Lee, and Fritz B Prinz. “Ionic and electronic impedance imaging using atomic force microscopy”. In: *Journal of applied physics* 95.12 (2004), pp. 8382–8392.

[88] Ryan O’Hayre et al. “Quantitative impedance measurement using atomic force microscopy”. In: *Journal of applied physics* 96.6 (2004), pp. 3540–3549.

[89] Steffen Hink et al. “Impedance spectroscopic investigation of proton conductivity in Nafion using transient electrochemical atomic force microscopy (AFM)”. In: *Membranes* 2.2 (2012), pp. 237–252.

[90] AN Morozovska et al. “Local probing of ionic diffusion by electrochemical strain microscopy: Spatial resolution and signal formation mechanisms”. In: *Journal of Applied Physics* 108.5 (2010), p. 053712.

[91] N Balke et al. “Nanoscale mapping of ion diffusion in a lithium-ion battery cathode”. In: *Nature Nanotechnology* 5.10 (2010), p. 749.

[92] Sergei V Kalinin and Anna N Morozovska. “Electrochemical strain microscopy of local electrochemical processes in solids: Mechanism of imaging and spectroscopy in the diffusion limit”. In: *Journal of Electroceramics* 32.1 (2014), pp. 51–59.

[93] Konstantin Romanyuk et al. “Giant Electric-Field-Induced Strain in PVDF-Based Battery Separator Membranes Probed by Electrochemical Strain Microscopy”. In: *Langmuir* 32.21 (2016), pp. 5267–5276.

[94] Stephan Bradler, André Schirmeisen, and Bernhard Roling. “Amplitude quantification in contact-resonance-based voltage-modulated force spectroscopy”. In: *Journal of Applied Physics* 122.6 (2017), p. 065106.

[95] André Schirmeisen et al. “Fast interfacial ionic conduction in nanostructured glass ceramics”. In: *Phys. Rev. Lett.* 98.22 (2007), p. 225901.

[96] Ahmet Taskiran et al. “Time-domain electrostatic force spectroscopy on nanostructured lithium-ion conducting glass ceramics: analysis and interpretation of relaxation times”. In: *Phys. Chem. Chem. Phys.* 11.26 (2009), pp. 5499–5505.

[97] Myounggu Park et al. “A review of conduction phenomena in Li-ion batteries”. In: *Journal of Power Sources* 195.24 (2010), pp. 7904–7929.

[98] John E Sader et al. “A virtual instrument to standardise the calibration of atomic force microscope cantilevers”. In: *Review of Scientific Instruments* 87.9 (2016), p. 093711.

[99] Joost Te Riet et al. “Interlaboratory round robin on cantilever calibration for AFM force spectroscopy”. In: *Ultramicroscopy* 111.12 (2011), pp. 1659–1669.

# A

Supporting Information for Chapter 2

## Supporting Information - Measuring Spatially Resolved Collective Ionic Transport on Lithium Ion Battery Cathodes using Atomic Force Microscopy

## A.1 Experimental Methods

### A.1.1 Atomic Force Microscopy Measurements.

The AFM measurements were performed using a highly customized JSPM-5200 microscope (including a custom fabricated sample heater stage) operating in high vacuum ($10^{-7}$ mBar) with a gold-coated tip ($r$ = 20 nm, $k$ = 231 N/m, $f_0$ = 1.227 MHz, $A_{pp} \approx 12$ nm for the platelet measurements; and $r = 20$ nm, $k = 27$ N/m, $f_0 = 296$ kHz, $A_{pp} \approx 5$ nm for the ingot measurements) controlled using GXSM [1]. A Nanosurf® EasyPLL Plus was used in the standard FM-AFM self-excitation configuration during scanning for the ingot sample measurements [2]. Topography images on the $LiFePO_4$ platelets were obtained in high vacuum using Q-control to decrease the effective quality factor [3]. KPFM was performed using the sideband detection scheme with an external PLL and PID controller (Zurich Instruments HF2) with a modulation amplitude of 2 V and modulation frequency of 800 Hz, as described elsewhere [4]. The $V_{dc}$ was applied to the tip while the sample was grounded, resulting in a $V_{cpd}$ value with the opposite sign as the difference in work function (sample-tip) so that the regions of high $V_{cpd}$ in the KPFM image actually correspond to a lower sample work function (see Figure S5).

A simple understanding of the ionic response starts with the general expression for the electrostatic force between a conducting AFM tip and a sample:

$$F = \frac{1}{2}\frac{\partial C}{\partial z}V^2 \tag{S 1}$$

If the tip is separated from the back electrode by a vacuum gap (between the tip and sample) and a dielectric sample, the series capacitance is:

$$C = \frac{1}{\frac{1}{C_v} + \frac{1}{C_\epsilon}} \tag{S 2}$$

where $C_v$ is the vacuum capacitance and $C_\epsilon$ is the capacitance of the dielectric. In the case where the ions fully screen the internal field after some saturation time ($t_s$), the capacitance of the dielectric goes to infinity, so the overall capacitance $C \to C_v$. Due to the small distance between the tip and surface of the sample, $C_v$ is much more sensitive to z-position than $C_s$, so $\frac{\partial C}{\partial z}$ increases. Thus, the electrostatic force will increase until the saturation time is reached. Since this process is due to ions hopping through a lattice on long timescales, the electrostatic force follows Eq. 2.

The time trace frequency shift data was fitted to Eq. SS 3, where $df_0$ is the initial frequency shift and $df_s$ is the final (saturation) frequency shift.

$$df(t) = df_0 + df_s \exp\left[-(t/\tau)^\beta\right] \tag{S 3}$$

The time constants were then fitted to Eq. 3 to determine activation energies and effective attempt frequencies for each probe-point. The bulk ionic hopping barriers were found using Eq. 4.

The optimal time resolution attainable (i.e. the fastest change in frequency that can be recorded) in FM-AFM is usually limited by the frequency detector (typically a phase-locked-loop, PLL), which has a finite response time to instantaneous frequency changes. In order to decrease this response time, the frequency detection bandwidth (and hence the overall input noise) must be increased. To achieve sub-millisecond time resolution, we developed a system that acquires a repeated signal and averages it in real-time until an acceptable noise level is achieved. To perform the relaxation-time measurements an external PLL (Zurich Instruments HF2) was used as a frequency detector with the bandwidth set to 4 kHz to realize a $\approx 150\mu$ s response time for measurements on the ingot sample and a 10 kHz bandwidth with response time $\approx 60\mu$ s for the platelet samples. This high (10kHz) bandwidth was achieved using ultra-high frequency cantilevers with $\sim$MHz resonance frequencies and allows for time resolution limited only by the real-time

averaging system. To achieve acceptable SNR, each measurement was averaged over $N = 100$ to $N = 700$ pulses by an on-line data processing system to acquire and average the data in real-time (developed using Mathworks® Simulink Real-Time® and running at a base sample rate of 20 kHz). The pulses were applied using a signal generator triggered by the SPM scan controller (Soft dB MK2-A810) for 40 ms. The measurements at each point/temperature were performed 10 times in order to calculate a statistical error value. Before each probe measurement, the initial $V_{dc}$ was set to the contact potential difference, $V_{cpd}$, by sweeping $V_{dc}$ to find the minimum in the parabolic $\Delta f$-$V_{dc}$ curve.

### A.1.2 Kelvin Probe Force Microscopy.

In general, the electrostatic force between an AFM tip and a sample is given by:

$$F_{es} = \frac{1}{2}\frac{\partial C}{\partial z}\Delta V^2 \tag{S 4}$$

where $C$ is the tip-sample capacitance, z is the tip-sample separation, and $\Delta V$ is the potential difference between the tip and sample. The contact potential difference is defined by:

$$V_{cpd} = \frac{\phi_{tip} - \phi_{sample}}{-e} \tag{S 5}$$

where $\phi$ refers to the work function of the materials and $e$ is the electron charge. Thus, if we apply both a $V_{dc}$ and a $V_{ac}$ (at some frequency $\omega$) between the tip and sample, the total voltage difference is given by:

$$\Delta V = V_{dc} - V_{cpd]} + V_{ac}\sin(\omega t) \tag{S 6}$$

Inserting this into Eq. SS 4, expanding, and simplifying, we see that there are three

frequency components of the overall electrostatic force:

$$F_{dc} = \frac{\partial C}{\partial z}\left[\frac{1}{2}\left(V_{dc} - V_{cpd}\right)^2 + \frac{1}{4}V_{ac}^2\right] \tag{S 7}$$

$$F_{\omega} = \frac{\partial C}{\partial z}\left[V_{dc} - V_{cpd}\right] V_{ac}\sin(\omega t) \tag{S 8}$$

$$F_{2\omega} = \frac{1}{4}\frac{\partial C}{\partial z}V_{ac}^2\cos(2\omega t) \tag{S 9}$$

The $\omega$ component of the force, $F_{\omega}$, is what is used in KPFM; we can clearly see that when $V_{dc} = V_{cpd}$, $F_{\omega}$ is zero. By controlling $V_{dc}$ with a feedback loop such that $F_{\omega} = 0$, we achieve $V_{dc} = V_{cpd}$ and thus $V_{cpd}$ can be measured.

While the $V_{cpd}$ is proportional to the difference in work functions between the tip and sample, the absolute value of these work functions cannot be easily determined due to a variety of factors, including difficulty in determining the exact tip work function (see [5] for a discussion of other challenges). In our case the $V_{cpd}$ has the opposite sign of the measured voltage so that the regions of lower work function on the sample have higher $V_{cpd}$ in Figure S4. This is due to the voltage ($V_{dc}$) measurement being taken from the tip potential while the sample is grounded. This can be better understood by drawing an energy level diagram as shown in Figure S5 [6]. Performing KPFM on a thick insulating sample with a high dielectric constant such as $LiFePO_4$ further complicates quantitative analysis as the voltage decay within the sample also has to be taken into account. The $\phi_{sample}$ has to be referred to the Fermi level of the back-electrode material, thus the $V_{cpd}$ variations along the surface will be a fraction of the true work function variations of the sample. The large capacitive force present between the macroscopic parts of the probe (namely the cantilever) also contribute to a complicated electrostatics problem with dependencies on not only the applied voltages and geometries, but also the tip oscillation

amplitude [7].

### A.1.3 Data analysis.

For each probe point 10 measurements were conducted at each temperature. After fitting the frequency shift vs. time data to Eq. SS 3 to extract the relaxation times, $\tau$, and stretching factor, $\beta$, the collective activation energies were obtained by a linear fit to the natural log of the relaxation times vs. energies as per Eq. 3 (i.e. the linear fit shown in Figure 2C). Parametric bootstrap was used to determine an estimate for the uncertainty on the activation energies, $\beta$, and $\tau_\infty$ using a Gaussian distribution with the mean and standard deviation of each data point and 1000 iterations [8]. A non-parametric bootstrap was performed for several points, but yielded the same uncertainty on the fit parameters to the indicated significance and thus a parametric boostrap was used to minimize computation time.

### A.1.4 TOF-SIMS.

The Time of Flight Secondary Ion Mass (TOF-SIMS) analyses were performed using the Tescan Lyra3 FIB/SEM microscope fitted with a TOF-SIMS from TOFWERK. A focus ion beam (Ga) with an ion current of 1.7 nA was used to sputter the secondary ions in an area with a field of view of 18 $\mu m$ (768 $\times$ 768 pixels). Electron beam flooding was used to minimize charging effects and obtain a reasonable SNR (spot mode, 2nA current at 5kV). The sample surface was normal to the ion beam. Each of the 7 frames recorded is composed of 768 $\times$ 768 extractions with a FIB dwell time of 10 $\mu s$ per pixel. The final image was binned 4 times (192 $\times$ 192 pixels). See Figure S7 for depth profiles and mass/charge spectra. The ion current and analyzed area were chosen so the features of interest were still visible after the analysis (quasi static mode). The voltage on the TOF-SIMS plates was selected so only the positive ions were measured.

### A.1.5 EBSD.

The ingot sample was ion milled (Hitachi IR4000+) using 3 kV $Ar^+$ for 3 minutes to minimize any residual stress at the sample surface. The sample was then glued onto a pre-tilted (70°) sample holder and analyzed in a Lyra3 microscope using a 20 kV electron beam. The EBSD detector utilized the Aztec software and NordlysNano camera (Oxford Instruments) to record the pattern. Both mapping (1 frame per second) and point analysis were used to determine the crystallographic orientation of the same region of interest that was measured using TOF-SIMS and on several $LiFePO_4$ platelet samples. The EBSD measurement on the ingot sample was performed after the TOF-SIMS measurement on the region of interest, which left the surface especially rough in the center grain (region B), while the outer regions remained relatively smooth. This roughness prevented a reasonable signal from being obtained on the center region, thus the indexation was not reliable and is therefore not reported here.

## A.2 *Ab initio* calculations.

The *ab initio* calculations were performed using the GGA functional by Perdew, Burke, and Ernzerhof (PBE) [9] within the projector augmented wave (PAW) formalism [10] as implemented in the Vienna *ab initio* simulation package (VASP) [11–14]. To account for the strong electron correlation present in the Fe $3d$ orbitals, an on-site Hubbard term $U$ was added to the functional (GGA + $U$). The value of $U$ depends on the material and the oxidation state of the Fe atoms, which we selected to be $U_{\text{eff}} = 3.7$ eV for pure $LiFePO_4$, $U_{\text{eff}} = 4.9$ eV for pure $FePO_4$, and $U_{\text{eff}} = 4.3$ eV for systems with mixed oxidation states [15, 16].

Ionic diffusion calculations were done on $1 \times 4 \times 2$ supercells with a plane wave energy cutoff of 500 eV and a single k-point at the Γ-point in reciprocal space. The dimensions

of the supercells were set to simulate a concentration of $x = 0.75$, with the lattice vectors assumed to be a linear combination of 25% $FePO_4$ and 75% $LiFePO_4$ lattice vectors. To simulate a phase boundary between $LiFePO_4$ and $FePO_4$, one half of the supercells were fully lithiated (with Fe sites reduced to 2+), and the other half empty (with the oxidation state of the Fe sites at 3+). To simulate interactions in a dilute phase, a system was studied where only two Li ions (and two polarons) are introduced in an otherwise fully delithiated supercell. The lowest energy configuration of this system was found through enumeration of all possible symmetrically distinct configurations. Internal coordinates were fully relaxed. To calculate diffusion barriers, we utilized the climbing image nudged elastic band method (CI-NEB) [17, 18] to optimize the images between endpoints.

To the best of our knowledge, the experimental reference values of the work functions of $LiFePO_4$ and $FePO_4$ are not available. Therefore, we investigated the work functions of $LiFePO_4$ and $FePO_4$ from an *ab initio* approach. Since the work functions of different surface orientations of the same material will not vary significantly (usually within a few tenth of eV, as confirmed by our calculations of two other surface orientations of $FePO_4$), we chose the (010) orientation, which has the lowest surface energy [19], as the characteristic surface for our calculation. A 20 Å thick slab of $LiFePO_4/FePO_4$ separated by a vacuum layer with a thickness of 40 Å was used in the study. By comparing the reported results with the those corresponding to slightly smaller thicknesses, our results appear to be converged.

## A.3 Materials Preparation

$LiFePO_4$ platelets were synthesized following a hydrothermal route (reported in Ref. [20]): 33.6 g (0.12 mol) $FeSO_4{\cdot}7H_2$, 15.41 g (0.36 mol) LiOH $H_2O$, 13.83 g (0.12 mol) $H_3PO_4$, and 0.5 g (0.003 mol) ascorbic acid ($C_6H_8O_6$) were mixed with 300 ml of deionised water in a glass liner. The final molar ratio for Li:Fe:$PO_4$:$C_6H_8O_6$ was 3:1:1:0.008. The pH

was controlled at 7.8 by drop-wise addition of $NH_4OH$. The synthesis was performed in a stirred autoclave (OM-JAPAN) for 5 hours at 180 °C. The resulting platelets at this stage were dispersed in Milli-Q water and drop cast onto a template stripped gold substrate. These platelets were used for the measurements shown in Figure 1.

To prepare the ingot sample, the platelets were then ground for 30 minutes with a SPEX® grinder prior to delithiation. The $LiFePO_4$ crystals were dispersed in potassium persulfate ($K_2S_2O_8$) water solution (molar ratio 2:1) and heated at 60 °C for 24 hours to promote the final $Li_xFePO_4$ conversion [21, 22]. Finally, the powder was held at 1050 °C under $N_2$ for 1 hour to obtain a bulk sample, which was polished using successive diamond abrasive papers from 30 $\mu$m down to 0.3 $\mu$m particle size.

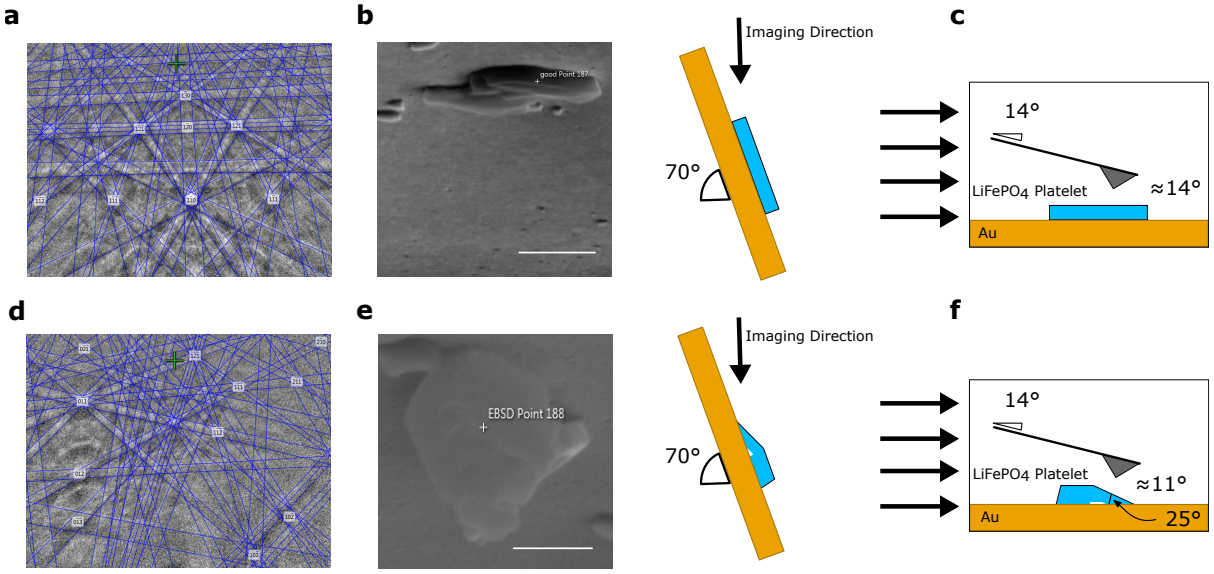


Figure S A.1: (**a**) Indexed Kikuchi pattern from EBSD conducted on platelet shown in (**b**). This pattern confirms that the (010) axis is directly perpendicular to the surface as shown in Figure 1A. (**b**) SEM image taken of a $LiFePO_4$ platelet on a gold substrate while oriented for EBSD measurement at a 70° angle as shown in illustration, scale bar 2$\mu$m. (**c**). Illustration of the orientation of the AFM cantilever with respect to the platelet and gold substrate. The nominal angle between the normal direction from the surface to the tip-axis of the cantilever is ≈14°. (**d**) Indexed Kikuchi pattern from EBSD conducted on platelet shown in (**e**), where it is clear that the platelet is not perfectly oriented along the gold surface. (**e**) shows an SEM image of the platelet taken in the EBSD orientation, as illustrated. From this image and the Kikuchi pattern we determined that the (010) axis is perfectly perpendicular to the surface of the platelet and the platelet is oriented at ≈25° from the gold surface, as illustrated in (**f**). The nominal angle between the normal direction from the platelet surface to the tip-axis of the cantilever is ≈11°, shown in (**f**)

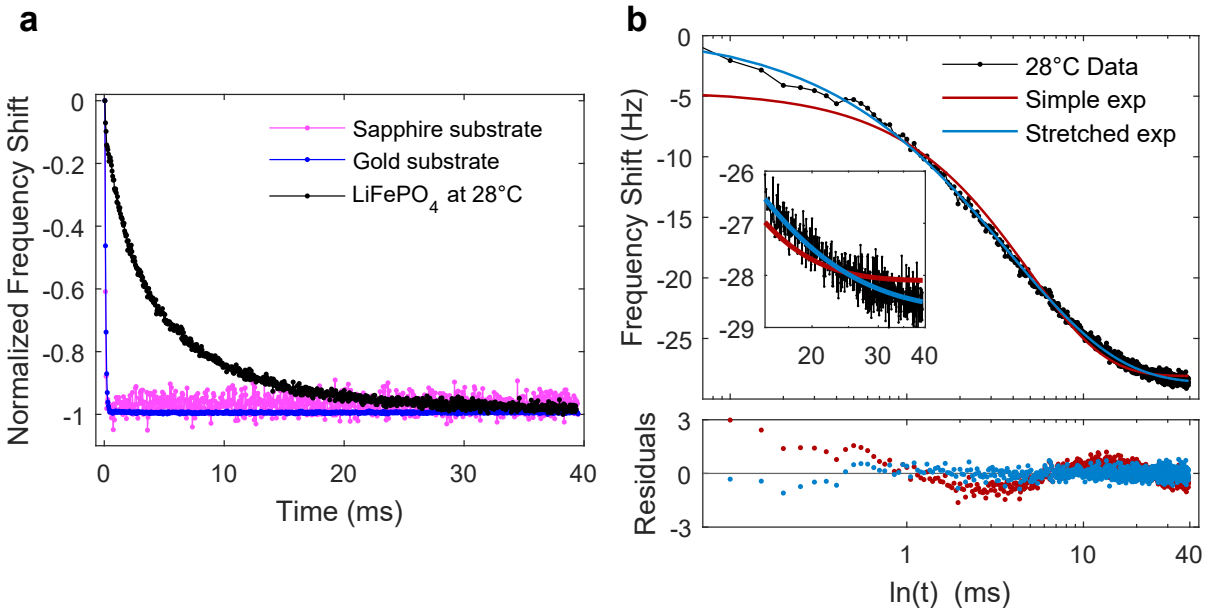


Figure S A.2: Ionic response validation measurements. (**a**) Normalized frequency shift vs. time for probe measurements performed on 430$\mu$m thick single crystal sapphire, gold, and the $LiFePO_4$ platelet shown in Figure 1E all conducted under the same conditions using the same cantilever. (**b**) Result of fitting the data shown in (**a**) taken on the $LiFePO_4$ sample to a pure exponential (red line) and a stretched exponential (blue line) with residuals from both fits shown below. Both plots are linear-log to better display the poor fit of the pure exponential function. A $\chi^2$ test on the residuals reveals that the pure exponential residuals are not normally distributed (p = 0.03), while the residuals for the stretched exponential fit are normally distributed (p = 0.17). Inset shows a close-up from 10-40ms, also as a linear-log plot.

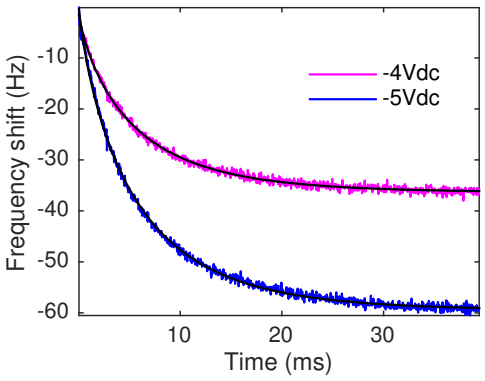


Figure S A.3: Probe measurements taken on the same point with two different $V_{dc}$ values (-4V and -5V as indicated). Black lines are fits to each curve. The parameters obtained from the fitting are: 5.46 ± 0.07 ms and 5.38 ± 0.11 ms; and 0.80 ± 0.03 and 0.80 ± 0.04 for -5V applied and -4V applied, respectively.

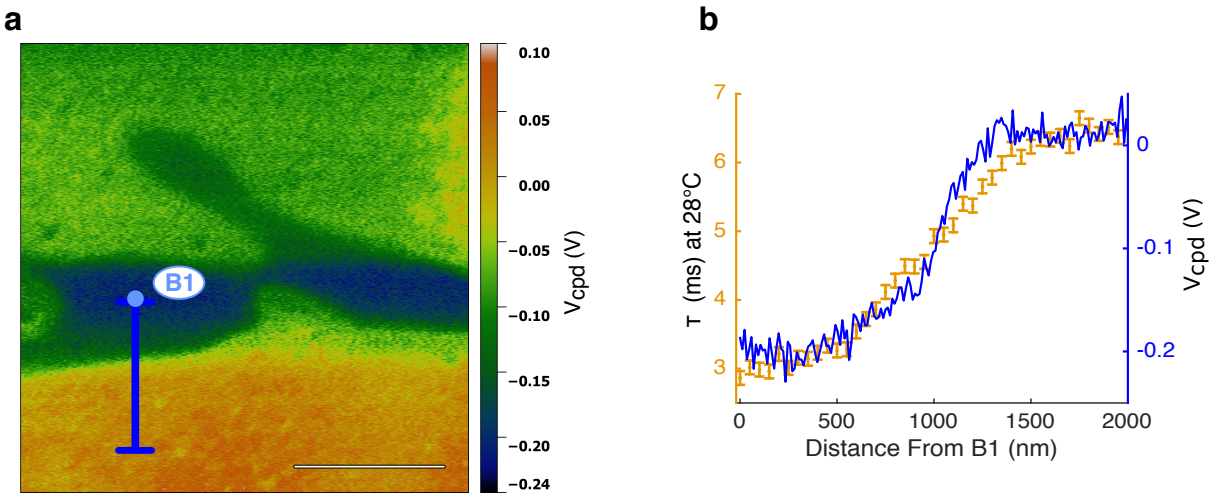


Figure S A.4: (**a**) Kelvin Probe Force Microscopy (KFPM) taken simultaneously with FM-AFM topography, scale bar is 2$\mu$m. (**b**) Surface contact potential difference data along the line indicated in (**a**) plotted on top of the relaxation time constants at each point spaced 50nm apart.

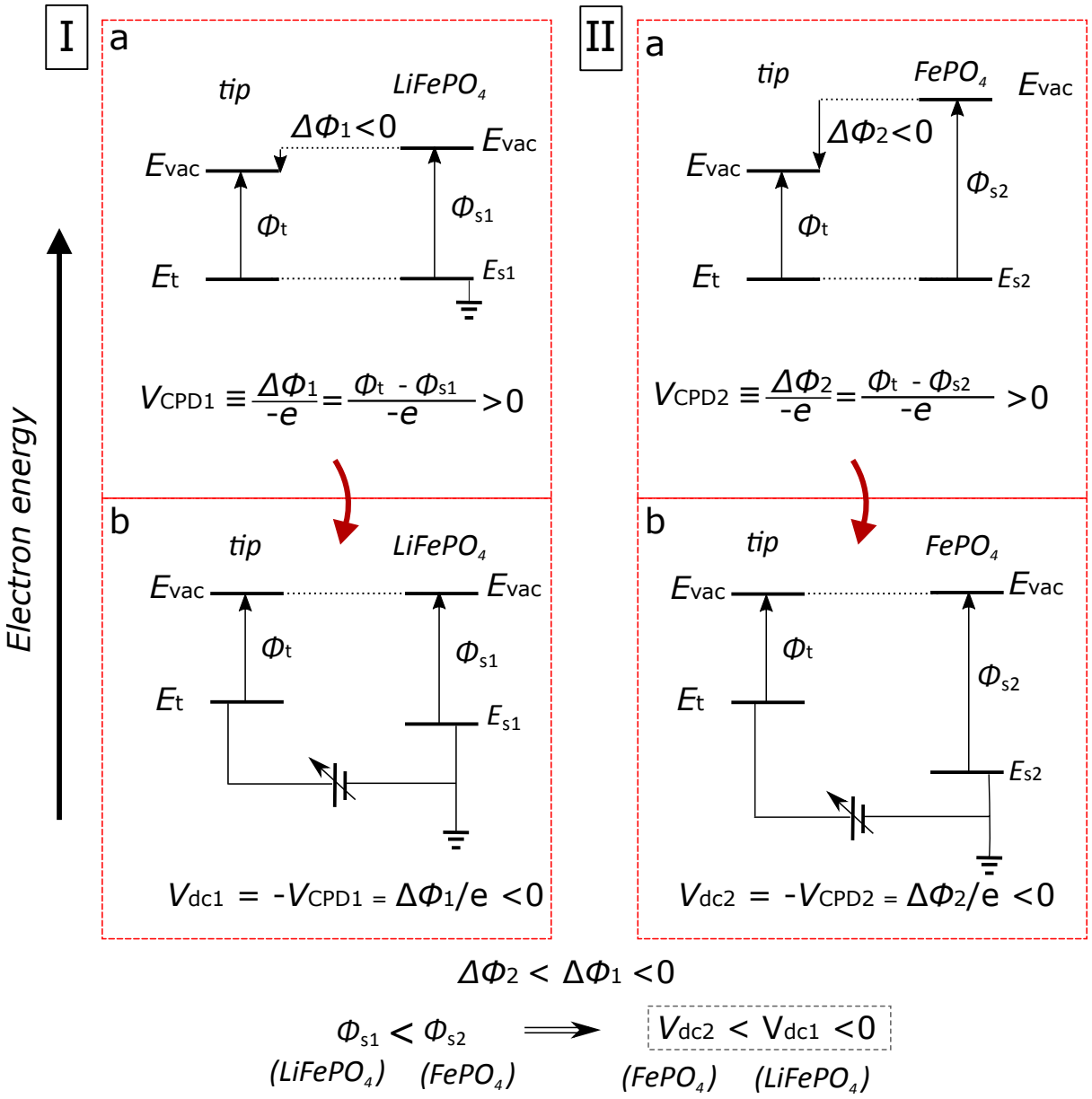


Figure S A.5: Tip-sample energy level diagrams for the $LiFePO_4$ and $FePO_4$ sample phases. The work functions of $LiFePO_4$ and $FePO_4$ are 5.2eV ($\phi_{s1}$) and 8.3eV ($\phi_{s2}$), respectively (see main text). Thus, for $LiFePO_4$ (case I) the sample has a lower work function ($\phi_{s1}$), which results in a more positive $V_{dc}$. $FePO_4$ has a higher work function ($\phi_{s2}$, case II), giving a more negative $V_{dc}$. For each case the (a) panel corresponds to the initial energy levels with no bias applied, while (b) gives the energy levels during the KPFM measurement.

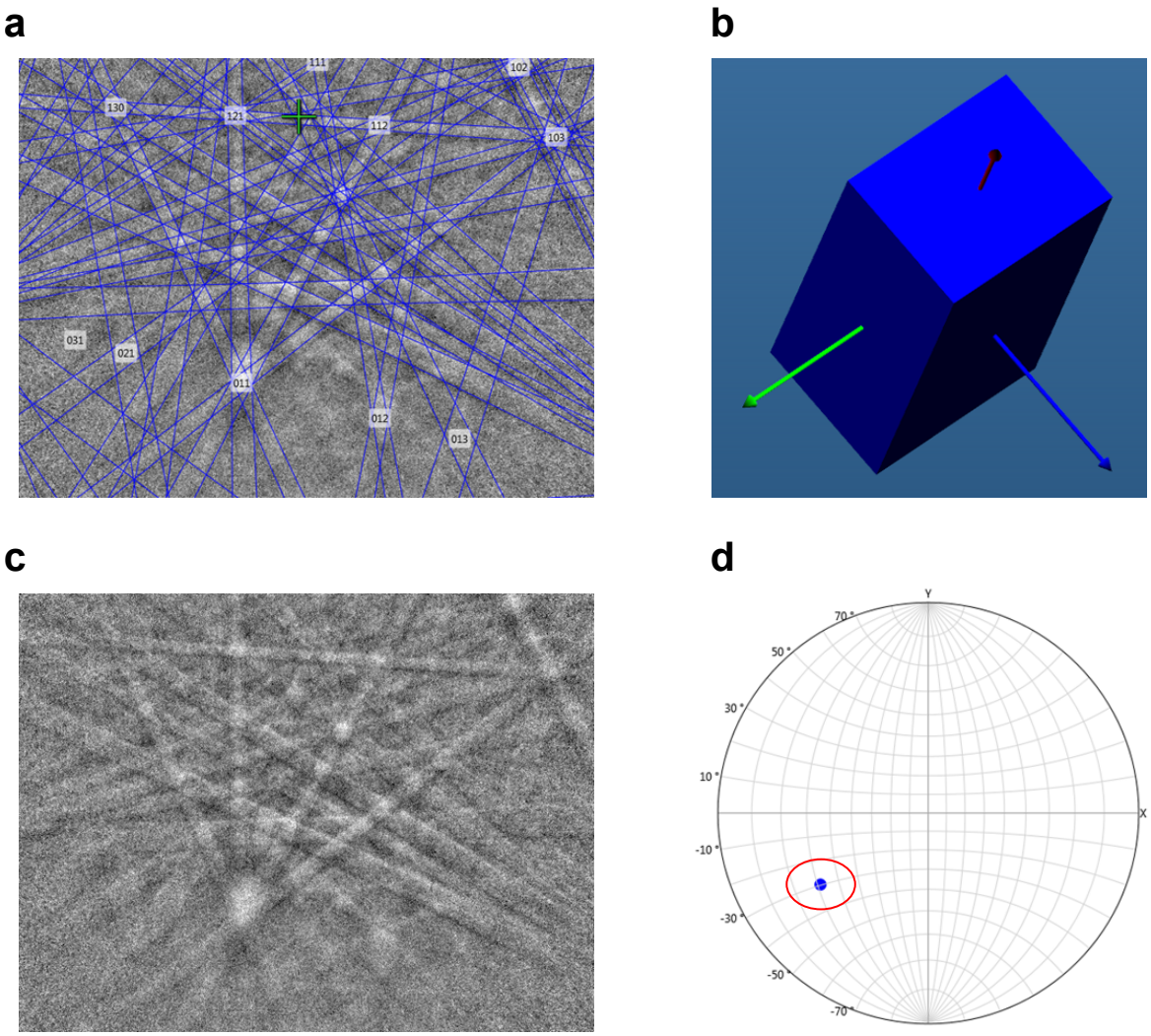


Figure S A.6: (**a**) Indexed Kikuchi pattern of $LiFePO_4$ phase on partially delithiated ingot sample. (**b**) Crystallographic orientation determined from Kikuchi pattern. (**c**) Raw Kikuchi pattern. (**d**) Pole plot of (010) axis showing orientations obtained from EBSD mapping over the $LiFePO_4$ region, circled in red.

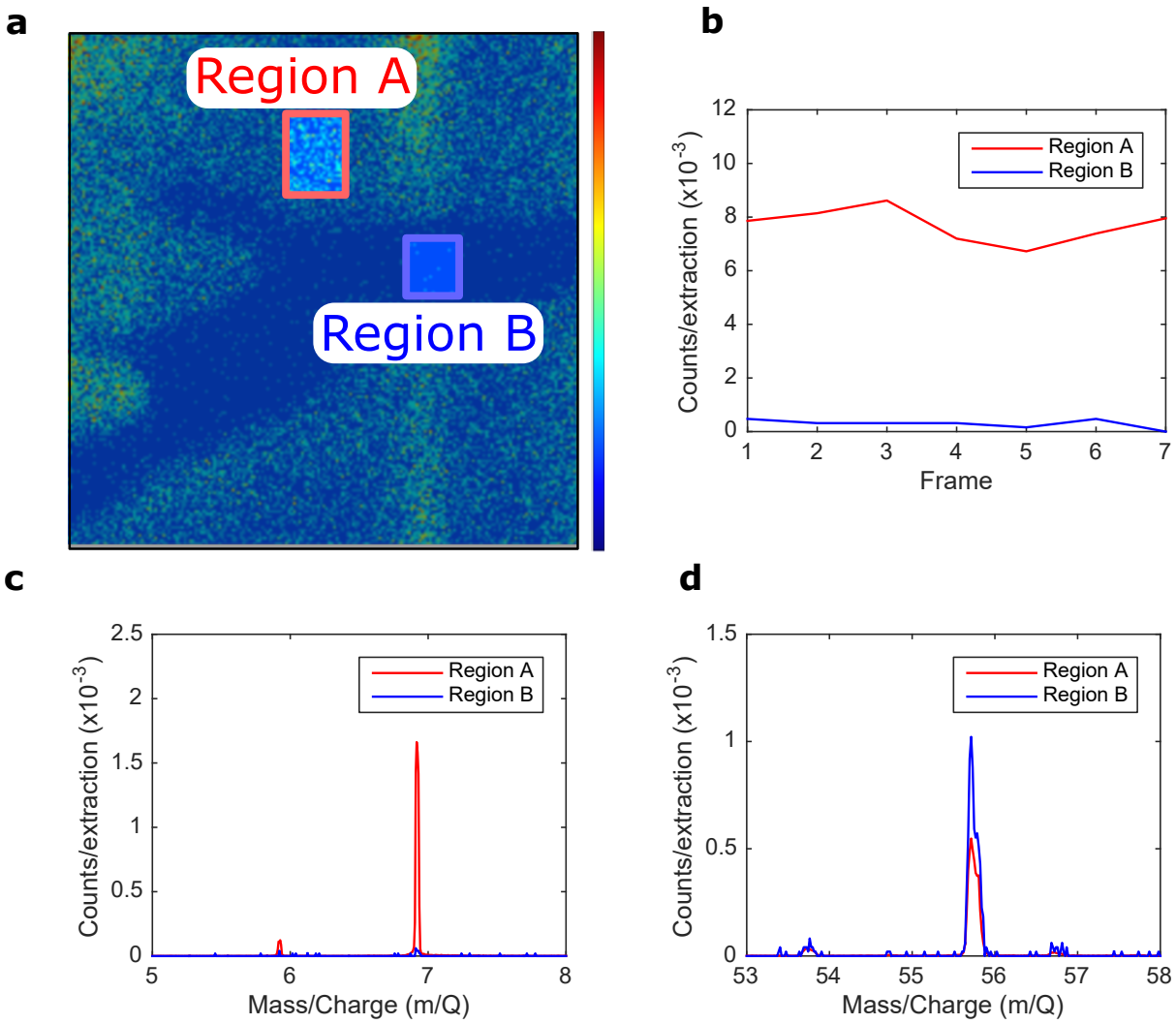


Figure S A.7: (**a**) TOF-SIMS mapping on the partially delithiated $LiFePO_4$ ingot sample with a high $Li^+$ concentration region (A) and a low $Li^+$ concentration region (B) outlined for analysis. Colour scale extends from 0 to 0.08 counts/TOF-SIMS extraction. (**b**) Counts/TOF-SIMS extraction of the indicated regions as a function of depth over all frames acquired. (**c**) Mass spectra of both regions A and B showing the $^6Li^+$ and $^7Li^+$ peaks. (**d**) Mass spectra of both regions A and B showing the $^{56}Fe^+$ peaks.

| **Point** | 1 | 2 |
|---|---|---|
| $\mathbf{E}_a^*$ **(eV)** | 0.44(7) | 0.49(3) |
| $\mathbf{E}_a$ **(eV)** | 0.26(4) | 0.34(2) |
| $\beta$ | 0.59(1) | 0.69(1) |
| $\tau_\infty$ **(s)** | 2(2) x$10^{-9}$ | 5(7) x$10^{-11}$ |
| **Collective Diffusivity ($cm^2/s$)** | 3.7(4) x$10^{-13}$ | 1.90(7) x$10^{-13}$ |
| **Bulk Diffusivity ($cm^2/s$)** | (0.2 ± 2.0) x$10^{-10}$ | 3(5) x$10^{-11}$ |

Table S A.1: Results obtained from both points indicated on the $LiFePO_4$ platelet shown in Figure 1E in the main text. Uncertainty of values obtained from fitting are the standard deviation values obtained from bootstrapping (see methods).

| **Point** | A1 | A2 | B1 | B2 | C1 | C2 |
|---|---|---|---|---|---|---|
| $\mathbf{E}_a^*$ **(eV)** | 0.54(2) | 0.54(2) | 0.62(3) | 0.62(3) | 0.49(1) | 0.52(1) |
| $\mathbf{E}_a$ **(eV)** | 0.30(1) | 0.30(1) | 0.36(1) | 0.38(1) | 0.31(1) | 0.33(1) |
| $\beta$ | 0.565(5) | 0.548(5) | 0.572(4) | 0.614(5) | 0.628(4) | 0.649(6) |
| $\tau_\infty$ **(s)** | 5(3) x$10^{-12}$ | 5(5) x$10^{-12}$ | 2(3) x$10^{-13}$ | 2(3) x$10^{-13}$ | 6(3) x$10^{-11}$ | 2(1) x$10^{-11}$ |
| **Collective Diffusivity ($cm^2/s$)** | 2.31(7) x$10^{-13}$ | 2.31(7) x$10^{-13}$ | 2.27(7) x$10^{-13}$ | 2.27(8) x$10^{-13}$ | 1.05(2) x$10^{-13}$ | 1.10(2) x$10^{-13}$ |
| **Bulk Diffusivity ($cm^2/s$)** | 1(1) x$10^{-9}$ | 2(2) x$10^{-9}$ | 4(6) x$10^{-9}$ | 2(2) x$10^{-9}$ | 1.1(6) x$10^{-10}$ | 1.1(6) x$10^{-10}$ |

Table S A.2: Results obtained at each of the 6 probe-points in order by region, top to bottom. Uncertainty of values obtained from fitting are the standard deviation values obtained from the Monte Carlo simulations (see Methods).

# References


[1] Percy Zahl et al. "The flexible and modern open source scanning probe microscopy software package GXSM". In: *Rev. Sci. Instrum.* 74.3 (2003), pp. 1222–1227.

[2] TR Albrecht et al. "Frequency modulation detection using high-Q cantilevers for enhanced force microscope sensitivity". In: *J. Appl. Phys.* 69.2 (1991), pp. 668–673.

[3] B Anczykowski et al. "Analysis of the interaction mechanisms in dynamic mode SFM by means of experimental data and computer simulation". In: *Appl. Phys. A: Mater. Sci. Process.* 66 (1998), S885–S889.

[4] Ulrich Zerweck et al. "Accuracy and resolution limits of Kelvin probe force microscopy". In: *Phys. Rev. B* 71.12 (2005), p. 125424.

[5] Dimitri SH Charrier et al. "Real versus measured surface potentials in scanning Kelvin probe microscopy". In: *ACS Nano* 2.4 (2008), pp. 622–626.

[6] Wilhelm Melitz et al. "Kelvin probe force microscopy and its application". In: *Surf. Sci. Rep.* 66.1 (2011), pp. 1–27.

[7] Ali Sadeghi et al. "Multiscale approach for simulations of Kelvin probe force microscopy with atomic resolution". In: *Phys. Rev. B* 86.7 (2012), p. 075407.

[8] Bradley Efron and Robert J Tibshirani. *An introduction to the bootstrap*. CRC press, 1994.

[9] John P. Perdew, Kieron Burke, and Matthias Ernzerhof. "Generalized Gradient Approximation Made Simple". In: *Phys. Rev. Lett.* 77 (18 1996), pp. 3865–3868. DOI: 10.1103/PhysRevLett.77.3865.

[10] G. Kresse and D. Joubert. "From ultrasoft pseudopotentials to the projector augmented-wave method". In: *Phys. Rev. B* 59 (3 1999), pp. 1758–1775. DOI: 10.1103/PhysRevB.59.1758.

[11] G. Kresse and J. Hafner. “Ab initio molecular dynamics for liquid metals”. In: *Phys. Rev. B* 47 (1 1993), pp. 558–561. DOI: 10.1103/PhysRevB.47.558.

[12] G. Kresse and J. Hafner. “Ab initio molecular-dynamics simulation of the liquid-metal–amorphous-semiconductor transition in germanium”. In: *Phys. Rev. B* 49 (20 1994), pp. 14251–14269. DOI: 10.1103/PhysRevB.49.14251.

[13] G. Kresse and J. Furthmuller. “Efficiency of ab-initio total energy calculations for metals and semiconductors using a plane-wave basis set”. In: *Comput. Mater. Sci.* 6.1 (1996), pp. 15–50. ISSN: 0927-0256. DOI: http://dx.doi.org/10.1016/0927-0256(96)00008-0.

[14] G. Kresse and J. Furthmüller. “Efficient iterative schemes for ab initio total-energy calculations using a plane-wave basis set”. In: *Phys. Rev. B* 54 (16 1996), pp. 11169–11186. DOI: 10.1103/PhysRevB.54.11169.

[15] Fei Zhou et al. “The electronic structure and band gap of LiFePO4 and LiMnPO4”. In: *Solid State Commun.* 132.3–4 (2004), pp. 181 –186. ISSN: 0038-1098. DOI: http://dx.doi.org/10.1016/j.ssc.2004.07.055.

[16] Thomas Maxisch, Fei Zhou, and Gerbrand Ceder. “Ab initio study of the migration of small polarons in olivine LixFePO4 and their association with lithium ions and vacancies”. In: *Phys. Rev. B* 73.10 (Mar. 2006), p. 104301.

[17] Graeme Henkelman, Blas P Uberuaga, and Hannes Jónsson. “A climbing image nudged elastic band method for finding saddle points and minimum energy paths”. In: *J. Chem. Phys* 113.22 (2000), pp. 9901–5.

[18] Gopi Krishna Phani Dathar et al. “Calculations of Li-ion diffusion in olivine phosphates”. In: *Chem. Mater.* 23.17 (2011), pp. 4032–4037.

[19] L. Wang et al. “First-principles study of surface properties of $LiFePO_4$: Surface energy, structure, Wulff shape, and surface redox potential”. In: *Phys. Rev. B* 76 (16 2007), p. 165435. DOI: 10.1103/PhysRevB.76.165435.

[20] Andrea Paolella et al. “Cation exchange mediated elimination of the Fe-antisites in the hydrothermal synthesis of LiFePO 4”. In: *Nano Energy* 16 (2015), pp. 256–267.

[21] K Zaghib et al. “Electronic, optical, and magnetic properties of LiFePO4: small magnetic polaron effects”. In: *Chem. Mater.* 19.15 (2007), pp. 3740–3747.

[22] R Stevens et al. “Phonons and thermodynamics of unmixed and disordered Li0. 6FePO4”. In: *J. Phys. Chem. B* 110.45 (2006), pp. 22732–22735.

# B

Supporting Information for Chapter 3

# Supporting Information - Review of time-resolved non-contact electrostatic force microscopy techniques with applications to ionic transport measurements

## B.1 sub_cycle_sim_beta.m

```
function output = sub_cycle_sim_beta(f0,Q,k,F0,Fe,df,tau,beta,Fs,ntaps,fc,n_pts,PLOT)
%
% This script solves the equation for a damped-driven harmonic oscillator
% with the parameters given below. This script applies a STRETCHED
% EXPONENTIAL electrostatic force at t = 3*Q*T at 0-phase.
%
%
% Based on the following works:
%
% [1] Giridharagopal, R. et al. Nano letters 12.2 (2012): 893-898.
% [2] Karatay, D. U., et al. Review of Scientific Instruments 87.5 (2016): 053702.
%
% Analysis is done as follows:
%
% Window the data and apply a blackman window-function, then apply a FIR
% filter, then Hilbert transform to get the phase and instantaneous
% frequency, which is plotted in the last line.
%
%%%%%%%%%%%%%%%%%%%%%%%%%%%%%%%%%%%%%%%%%%%%%%%%%%%%%%%%%%%%%%%%%%%%%%%%%%%%%%%
%          INPUTS
%
%
% Cantilever parameters:
%
% f0    = resonance frequency (Hz)
% Q     = Q-factor
% k     = spring constant (N/m)

% Force parameters:
%
% F0    = drive force (N)
% Fe    = electrostatic force (N)
% df    = maximum frequency shift (Hz)
% tau   = relaxation time-constant (s)
% beta  = stretching factor (0 < beta < 1)
```

```
% Filter/simulation parameters:
%
% Fs    = sample rate (samples/s)
% ntaps = # coefficients for FIR filter (MUST BE ODD)
% fc    = FIR filter cutoff frequency (Hz)
% n_pts = # of points around the pulse to analyze/plot
% PLOT = plot result (BOOLEAN)
%
%%%%%%%%%%%%%%%%%%%%%%%%%%%%%%%%%%%%%%%%%%%%%%%%%%%%%%%%%%%%%%%%%%%%%%%%%%%%%%%

syms y(t) t

W0 = f0*2*pi;      % Ang. freq.
T = 1/f0;          % Period
m = k/W0^2;
dW = df*2*pi;

ts = 1/Fs;
tTrig = Q*T*3;               % Trigger time at 3*Q periods into the sim.
tTotal = tTrig*2;            % Total sim time

t0 = 0:ts:tTrig;             % Ring-up time array
t1 = t0(end):ts:tTotal;      % Pulse-applied time array

FdFunc = @(t) F0*sin(W0*t);              % Drive force

% This function makes the 2nd order diff eq. into a system of 1st orders:
[V0] = odeToVectorField(diff(diff(y)) + W0/Q*diff(y) + W0^2*y == FdFunc(t)/m);
M0 = matlabFunction(V0,'vars', {'t','Y'}); % Make it a Matlab function
sol0 = ode45(M0,[t0(1),t0(end)],[0 1.9e-9]); % Solve it, y(0) = 0, y'(0) = 1

% Exponential function:
expParams = [tau];
C = @(params,t) (1-exp(-((t-t1(1))/params(1)).^beta));

% Frequency change(t) after exponential pulse is applied:
dWFunc = @(t) W0 - dW * C(expParams,t);

% This is the actual system response with an exponential pulse applied at t1(1):
```

```
[V1] = odeToVectorField(diff(diff(y)) + dWFunc(t)/Q*diff(y) + dWFunc(t)^2*y == Fe*C(expParams,t)/m +
    FdFunc(t)/m);
M1 = matlabFunction(V1,'vars', {'t','Y'});              %Make it a Matlab function
sol1 = ode45(M1,[t1(1),t1(end)],[deval(sol0,t0(end))]); %Solve it


y0 = deval(sol0,t0,1);
y1 = deval(sol1,t1,1);
tf = horzcat(t0,t1(2:end));
yf = horzcat(y0,y1(2:end));


Nf = 1/ts/2; % Nyquist frequency

% Number of samples to use around the trigger pulse (same number before+after):
% Sample number when trigger occured:
st = length(y0);

bwindow = blackman(length(yf(length(t0)-n_pts/2:length(t0)+n_pts/2-1)));

windowedSig = yf(length(t0)-n_pts/2:length(t0)+n_pts/2-1).*bwindow'; % Windowed and filtered signal
twindowed = tf(length(t0)-n_pts/2:length(t0)+n_pts/2-1);         % Time for windowed signal

FILT = fir1(ntaps,[(f0-fc/2)/Nf,(f0+fc/2)/Nf],'bandpass',blackman(ntaps+1));
filteredData = conv(windowedSig,FILT,'same');

% Take the hilbert transform of the signal:
z = hilbert(filteredData);
% Get the phase:
phi = unwrap(angle(z));

% Linear fit to the phase, can be used to subtract the resonance before
% filtering/differentiating:
phaseFit = polyfit(twindowed(end/4:end/3)-twindowed(1),phi(end/4:end/3),1);
yData = (twindowed-twindowed(1))*phaseFit(1) + phaseFit(2);

filtPhi = sgolayfilt(phi-yData,1,5);

Fs = 1/(t0(2)-t0(1));
instFreq = Fs./(2*pi)*diff(filtPhi);
```

```
% Correct the time, which is shifted by (ntaps - 1)/2:
tShift = twindowed((ntaps-1)/2:end-(ntaps-1)/2-1)-t0(end);
instFreq = instFreq(1:end-(ntaps-2));

if(PLOT)
plot(tShift,instFreq);
set(gca,'xlim',[0,0.3e-3])
end

output = vertcat(tShift,instFreq);
```

# C

Supporting Information for Chapter 4

# Supplementary Materials - Eliminating the effect of acoustic noise on cantilever spring constant calibration

## C.1 Effect of Transfer Function on Frequency Sweep Measurements

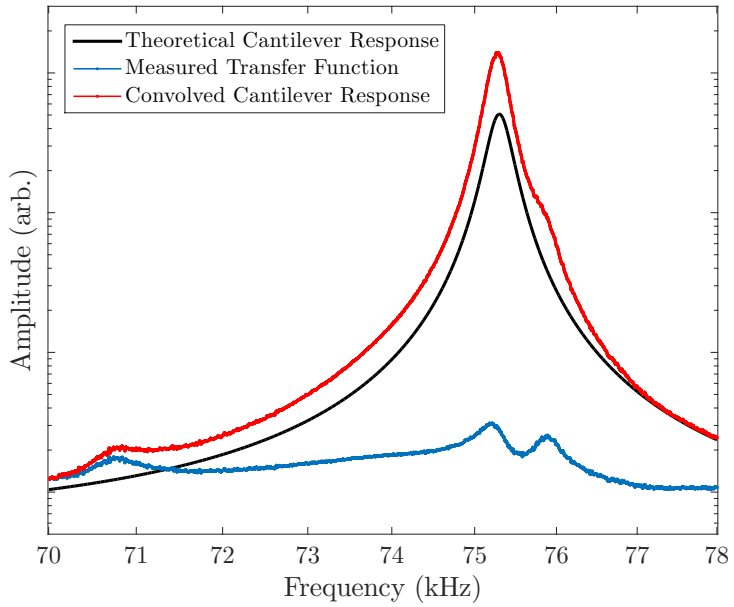


Figure S C.1: The blue data shows the measured transfer function of a cantilever, extracted using the procedure outlined in Ref. [1]. The black line shows synthetic data of the theoretical response of a cantilever with $Q = 225$ and $f_0 = 75.30$kHz, while the red line shows the convolution of the measured transfer function and the theoretical response.

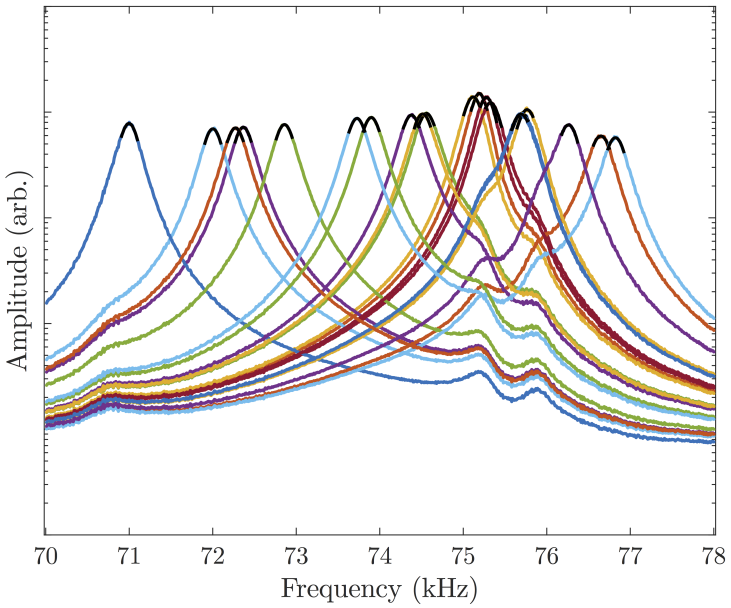


Figure S C.2: Synthetic datasets of theoretical cantilever response convolved with a measured transfer function (as shown in Figure C.1). Black lines are fits as described in the main text (see Figure 3). The resonance frequencies obtained from fitting were compared to the known values used to produce the synthetic data. The largest deviation in the most extreme case was 35Hz, corresponding to a difference of 0.03%.

## C.2 Effect of Drive Frequency on Ringdown Measurements

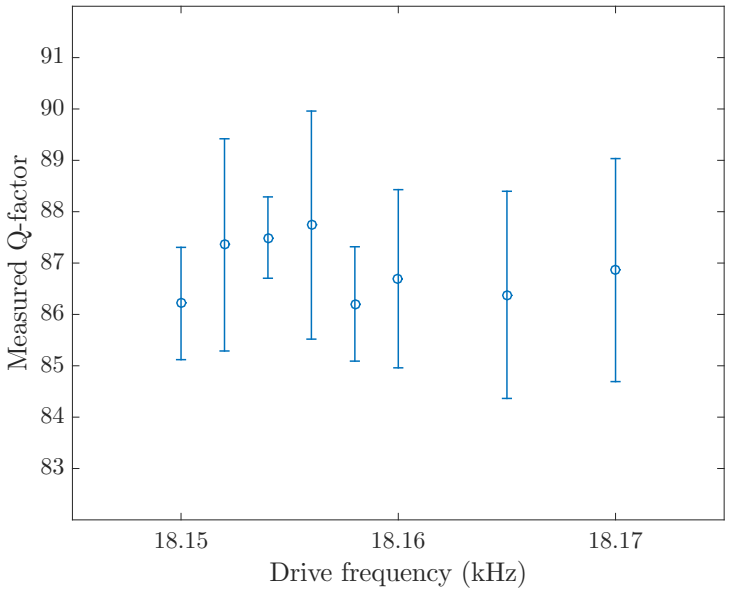


Figure S C.3: Measured quality factor for cantilever Type A - 1 at various drive frequencies. Data demonstrates that the correct quality factor can be obtained (within experimental uncertainty) even if the drive is not perfectly on resonance.

## C.3 Effect of Fitting to PSD Data Directly

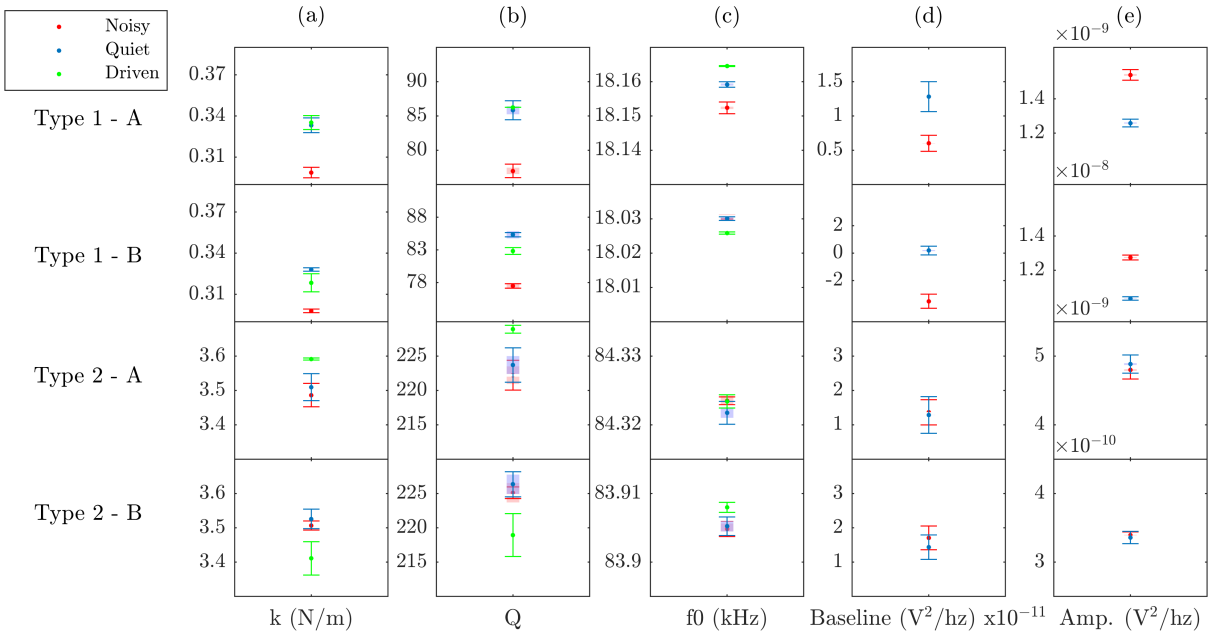


Figure S C.4: **(a)** Spring constants obtained from Equation 2. **(b)** quality factors, **(c)** resonance frequencies ($\omega_0/2\pi$), **(d)** baseline noise levels ($\alpha_2$) and **(e)** peak amplitudes ($\alpha_1$) obtained from fitting the 'thermal' oscillation PSD measurements of 4 different cantilevers with (red) and without (blue) ambient acoustic noise to Equation 1 directly. Results for the driven-calibration method described in the text are shown in green. Error bars are the uncertainty on the mean from 5 measurements on each cantilever. Shaded regions are theoretical uncertainties on the fit parameters obtained from the formulas given in Refs. [2] and [3].

### C.3.1 Discussion

As can be seen in Figure C.4(b), the quality factors and spring constants obtained from fitting the PSD data directly can also be affected by acoustic noise. Interestingly, the quality factors obtained for the Type 1 cantilevers were significantly lower with the acoustic noise than without – the opposite trend than was seen with the logarithm fitted data. This is likely due to the larger weighting of noise on the data on the resonance peak than the baseline noise due to its multiplicative nature. Regardless of the exact mechanism, the acoustic noise clearly has a non-negligible effect on the quality factors and thus the

spring constants obtained through measurements of the thermal PSD.

An interesting side effect of the direct-fitting is the sensitivity of the measured baseline noise levels on the acoustic noise, as shown in Figure C.4(d). In the case of cantilever Type 1 - B a negative value for the baseline noise was obtained, again likely due to the larger weighting of noise on the resonance peak vs. away from resonance.

The shaded regions in both Figure C.4(b)-(e) and Figure 2 (main text) are the theoretical uncertainties calculated using the formulas given in Refs. [2] and [3]. The measured uncertainties were $\sim$50% and $\sim$250% smaller than the theoretical uncertainties for the resonance frequencies and quality factors (respectively) when the logarithm of the data was fitted. When the PSD data was fitted directly, the measured uncertainties were $\sim$20% and $\sim$30% larger than the predicted theoretical uncertainties for the resonance frequencies and quality factors respectively. Despite the rough agreement for the other two parameters, the measured uncertainties for both the baseline and amplitudes were significantly higher than the theoretical predictions regardless of the fitting procedure.

## C.4 Systematic Effect of Acoustic Noise on Fit Parameters

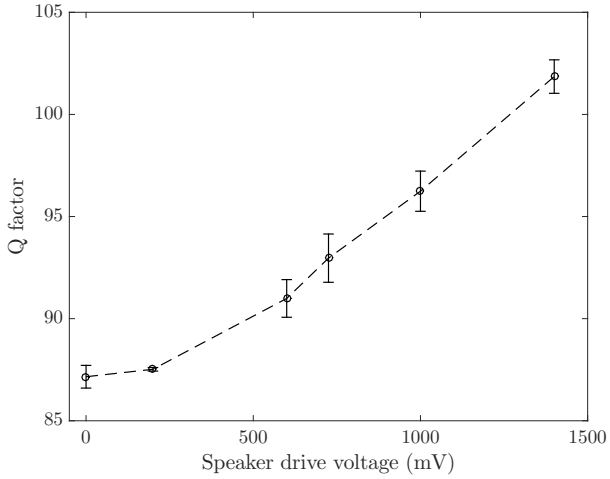


Figure S C.5: Quality factor $Q$ obtained from thermal PSDs for cantilever 1 - A as a function of white noise drive voltage sent to the speaker.

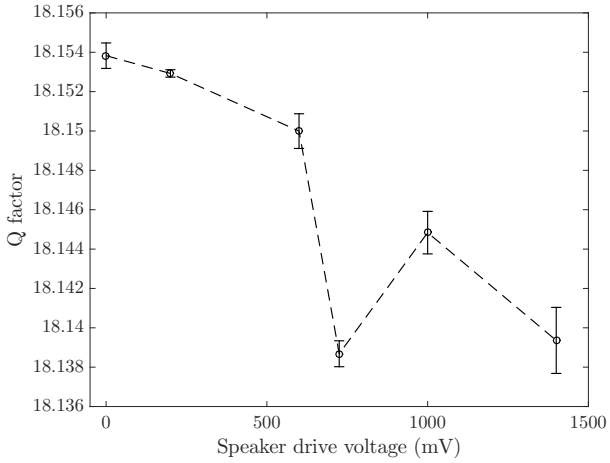


Figure S C.6: Resonance frequency $f_0$ obtained from thermal PSDs for cantilever 1 - A as a function of white noise drive voltage sent to the speaker.

### C.4.1 Discussion

Figure 3 (main text) shows the spring constant obtained for cantilever 1 - A as a function of the white noise voltage supplied to the speaker, while the inset shows the raw spectra for each of the 6 points. Figures C.5 and C.6 show the raw values of $Q$ and $f_0$ used to calculate the spring constants in Figure 3. Above the highest speaker noise voltage shown here (1400mV) the least-squares fitting failed (i.e. returned NaN for at least 1 of the parameters). The spectrum for 725mV speaker noise voltage is the same as the spectrum in Figure 1(b) and was used for the noisy data for cantilever 1 - A in Figure 2. A rough estimate of the ambient noise level at this speaker noise voltage was measured using an iPhone application (Decibel X) and is approximately 61dB (within the range of a normal conversation). At the highest speaker noise drive voltage shown here the ambient level was approximately 67dB, while the quiet noise level was approximately 56dB.

# References

[1] Aleksander Labuda et al. “Decoupling conservative and dissipative forces in frequency modulation atomic force microscopy”. In: *Physical Review B* 84.12 (2011), p. 125433.

[2] John E Sader, Morteza Yousefi, and James R Friend. “Uncertainty in least-squares fits to the thermal noise spectra of nanomechanical resonators with applications to the atomic force microscope”. In: *Review of Scientific Instruments* 85.2 (2014), p. 025104.

[3] John E Sader et al. “Effect of multiplicative noise on least-squares parameter estimation with applications to the atomic force microscope”. In: *Review of Scientific Instruments* 83.5 (2012), p. 055106.